THE ROLE OF INTERFACES AND DEFECTS ON THE THERMAL TRANSPORT IN NANO-ELECTRONIC SEMICONDUCTING MATERIALS

A Dissertation
Presented to
The Academic Faculty

by

Zhequan Yan

In Partial Fulfillment
of the Requirements for the Degree
Doctor of Philosophy in the
School of Mechanical Engineering

Georgia Institute of Technology
December 2018

THE ROLE OF INTERFACES AND DEFECTS ON THE THERMAL TRANSPORT IN NANO-ELECTRONIC SEMICONDUCTING MATERIALS

Approved by:

Dr. Satish Kumar, Advisor
School of Mechanical Engineering
Georgia Institute of Technology

Dr. Zhuomin Zhang
School of Mechanical Engineering
Georgia Institute of Technology

Dr. Eric Vogel
School of Material Science and Engineering
Georgia Institute of Technology

Dr. Seung Soon Jang
School of Material Science and Engineering
Georgia Institute of Technology

Dr. Matthew McDowell
School of Mechanical Engineering & Material Science and Engineering
Georgia Institute of Technology

Date Approved: August 21, 2018

ACKNOWLEDGEMENTS

Firstly, I would like to express my special appreciation and sincere gratitude to my advisor Dr. Satish Kumar for his continuous support of my research, for his invaluable advice of my career, for his patience, motivation, and immense knowledge. I'm so lucky to work with such a brilliant, passionate, nurturing, and kind person.

I would like to extend my appreciation to committee members: Dr. Zhuomin Zhang, Dr. Seung Soon Jang, Dr. Eric Vogel, and Dr. Matthew McDowell for providing valuable research advice and insightful comments for the improvement of this work. I would like to thank Dr. Mina Yoon for her valuable collaboration in several parts of this work. I am also very thankful to my colleagues and friends: Dr. Liang Chen, Dr. Man Prakash Gupta, David Brown, Jialuo Chen, Wenqing Shen, Matthew Barry and Nitish Kumar for providing a great company. I am also thankful to my roommate Tianyuan Liu for making me feel home away from home.

I am deeply indebted to my parents for their unconditional love and support throughout my life. I can never thank you enough for all of your love and encouragement during these years.

Above all, I would like to thank my wife Xiao for her love and constant support. Thank you for being my soul mate. I owe you everything.

Table of Contents

LIST OF TABLES

LIST OF FIGURES

LIST OF SYMBOLS AND ABBREVIATIONS

Abbreviations

AGF	Atomistic Green's function
BTE	Boltzmann transport equation
CVD	Chemical vapor deposition
DFT	Density functional theory
DOSs	Density of states
ELF	Electron localization function
FET	Field effect transistor
GFET	Graphene field effect transistor
GNR	Graphene nano-Ribbon
IFC	Interatomic force constant
LA	Longitudinal acoustic
LD	Lattice dynamics
LO	Longitudinal optical
MD	Molecular dynamics
MFP	Mean free path
MLG	Multilayer graphene
NEMD	Non-equilibrium molecular dynamics
RTA	Relaxation time approximation
SLG	Single-layer graphene
TA	Transverse acoustic

TBC	Thermal boundary conductance
TO	Transverse optical
VASP	Vienna *ab initio* package
ZA	Out-of-plane acoustic
ZO	Out-of-plane optical
vdW	van der Waals

Symbols

C	Specific heat
D	Dynamical matrix
E	Energy functional
E_f	Fermi energy
$\vec{F}$	Force vector
G	Green's function
H	Harmonic matrix
J	Heat flux
L	Length
N	Number of atoms, Bose-Einstein distribution
V	Interatomic potential, volume
a	Lattice constant
d	Diameter, distance between graphene and substrate
e	Energy density
e''	Energy flux

f	Scaling factor of interatomic force constants, Fermi-Dirac distribution
g	Velocity spectrum
$\hbar$	Planck constant
k	Electron wave vector, thermal conductivity
k_B	Boltzmann constant
m	Atom mass
k	Phonon wave vector
$\vec{r}$	Atom position vector
t	Time
u	Atom displacement
$\ddot{u}$	Atom acceleration
v	Phonon group velocity

Greek Letters

Φ	Second-order force constant matrix
Γ	Phonon escape rate in Green's function
Ψ	Wave function
Θ_D	Debye temperature
Ξ	Transmission function
χ	Scaling factor in Lennard Jones potential model
δ	Dirac delta function
σ	Thermal conductance, distance parameter in Lennard-Jones potential

ρ	Electron density
θ	Spectral energy density
τ	Phonon lifetime, correlation time, relaxation time
ω	Angular frequency

Superscript and Subscript

L, D, R, C	Left, device, right, and contact
xc	Exchange-correlation functional
α, β, γ	Indices of directions in Cartesian coordinate
i, j	Indices of atoms in a unit cell
l	Indices of unit cells

SUMMARY

As the device dimension scales down and power dissipation increases in the electronic devices, the inefficient thermal management becomes challenging for the performance and reliability. Phonons are expected to be the dominant energy carriers for the thermal transport in the nano-electronic semiconducting materials such as Graphene, 2D transition metal dichalcogenides (TMDs), and ultra-wide bandgap semiconductors (UWBGS), such as GaN and β-Ga_2O_3. Due to the low thermal boundary conductance at the interfaces, and the defect-induced phonon scatterings in these materials, the heat dissipation becomes even worse in their micro- and nano-electronic devices. A fundamental understanding of phonon transport properties of these electronic materials considering the influence of interfaces, boundaries, and defects is of high importance for improving reliability and energy efficiency of their electronic devices.

In this work, the phonon transport at the interface of vertically stacked graphene and h-BN heterostructures is investigated using first-principles density functional theory (DFT) and atomistic Green's function (AGF) simulations. The frequency and wave-vector dependent phonon transmission function is computed. Results indicate distinct stacking-dependent thermal boundary conductance (TBC) features for the graphene/h-BN interfaces. In addition, the role of interfacial electronic properties on the phonon transport in monolayer MoS_2 adsorbed on metal substrates (Au and Sc) is studied using the DFT and AGF methods. The study reveals that the different degree of orbital hybridization and electronic charge distribution between MoS_2 and metal substrates play a significant role in determining the overall phonon-phonon coupling and phonon transmission. The findings

demonstrate the inherent connection among the interfacial electronic structure, the phonon distribution, and TBC, which will help in understanding the mechanism of phonon transport at the MoS_2/metal interfaces.

Another part of this study is investigating the phonon transport properties of electronic materials, such as $MoSe_2$ and β-Ga_2O_3, under the influence of doping and defects using DFT along with the phonon Boltzmann transport equation (BTE) simulation. The model for estimating the influence of vacancy defects on the thermal conductivity is developed by considering contributions of different types of the defect-induced phonon scatterings. The influence of different types of the defects on the thermal conductivity is studied using the first-principles DFT, considering supercell with defects, which is a parameter-free model. The findings help us understand how the vacancy-induced phonon states impact the mechanism of phonon transport of $MoSe_2$. Furthermore, a modified empirical model of defects is developed in this study which is in better agreement of the parameter-free DFT simulation results. The results from this work will help in understanding the defect-induced phonon transport mechanism in electronic semiconducting materials and provide reliable empirical models to estimate the material properties considering the influence of defects, which could be used for the future design of electronics.

CHAPTER 1 : INTRODUCTION

As the device dimension scales down and power dissipation increases in the electronic devices, the inefficient thermal management becomes challenging for the performance and reliability. Phonons are expected to be the dominant energy carriers for the thermal transport in the nano-electronic semiconducting materials such as Graphene, 2D transition metal dichalcogenides (TMDs) ,and ultra-wide bandgap semiconductors (UWBGS), such as GaN and β-Ga_2O_3. It's necessary to understand the thermal transport in these nano-electronic semiconducting materials to control the hot spot temperature in its active devices and also for the design of packaging and thermal solutions. In this chapter, a brief description of their unique electronic, optical and thermal properties and their applications in electronic devices is introduced. The motivations, objectives and outlines of the current work are discussed as follows.

1.1 Electronic Applications of Graphene

Graphene as one of the remarkable two-dimensional (2D) materials exhibits exceptional thermal and electrical properties, such as high intrinsic carrier mobility, high mechanical strength and high thermal conductivity,[1, 2] which make it promising for many electronic applications such as high-frequency analog and RF devices [3-6]. It has a single atomic planar sheet which consists of sp^2 bonded carbon atoms in hexagonal lattices. The long-range π-conjugation in graphene yields extraordinary thermal, mechanical, and electrical properties but zero bandgap. A sizable bandgap can be opened by various methods such as doping, oxidation, introducing the substrates and making graphene nanoribbons (GNR).[7-9] Figure 1.1 shows the schematic diagram of a top-gated graphene

field effect transistor (GFET) which consists of a gate/dielectric-barrier/channel/substrate layers, and source and drain electrodes. Lin et, al. has fabricated a top-gated graphene transistors which can operate as high as 26 GHz frequencies.[10] Mattevi et al. reported the fabrication of solution processed flexible graphene transistors at low temperature shown in Figure 1.2. A wideband, frequency-tunable, terahertz and infrared detector based on graphene transistors was also demonstrated in 2013[11].

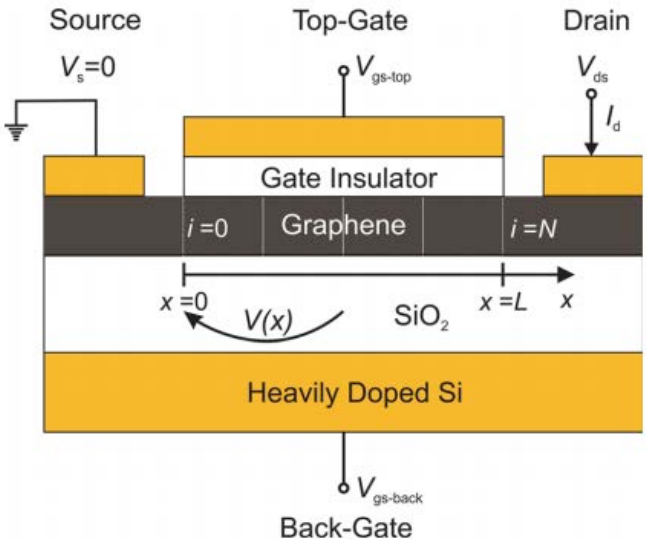

Figure 1.1 A schematic diagram of a top-gated graphene FET. The voltages $V_{gs\text{-}top}$, V_{ds}, and $V_{gs\text{-}back}$ are the external, i.e., terminal, top-gate-source, drainsource, and back-gate-source voltages. Copyright 2011 American Institute of Physics.[12]

Due to its high transparency from ultraviolet to near-infrared region and the high electrical conductivity, graphene has the potential to become the transparent electrode materials for applications in photovoltaic devices such as LEDs and solar cells [8, 13, 14]. Figure 1.3(a) shows the photograph of transparent and flexible graphene electrode. In addition, transparent, conductive, and ultrathin graphene films, as an alternative to the ubiquitously employed metal oxides window electrodes for solid-state dye-sensitized solar

cells, are demonstrated by Wang et al.[14] shown in Figure 1.3(b). These graphene films, fabricated from exfoliated graphite oxide, followed by thermal reduction, showed high conductivity of 550 S/cm and >70% transmission in the 1000–3000 nm spectral region, together with high chemical and thermal stability.

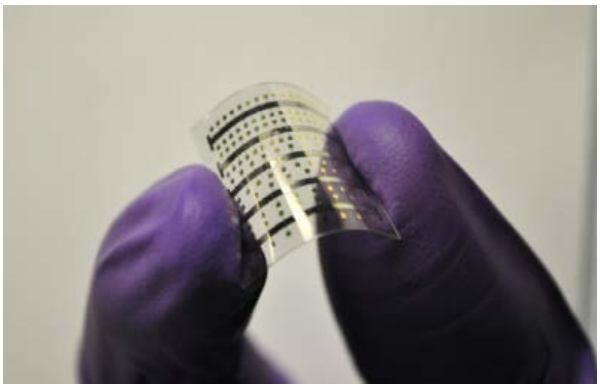

Figure 1.2 Photograph of a set (35 devices) of octadecylphosphonic acid (ODPA) self assembled monolayer (SAM) based chemical vapor deposition (CVD) graphene transistors fabricated on PET substrates. Copyright 2012 IOPscience[15].

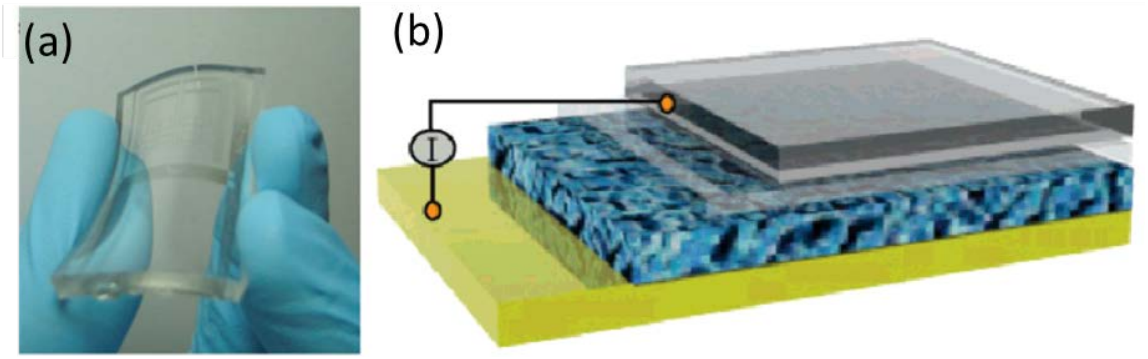

Figure 1.3 (a) Photograph of transparent and flexible graphene electrode. Copyright 2009 Nature.[16] (b) Illustration of dye-sensitized solar cell using graphene film as electrode, the four layers from bottom to top are Au, dye-sensitized heterojunction, compact TiO_2, and graphene film. Copyright 2008 American Chemical Society.[14]

Another area of potential applications of graphene are batteries and energy devices, especially Li batteries,[17-20] supercapacitors,[21, 22] due to its high surface area to mass

ratio (2630 m^2/g for monolayer graphene).[23] The graphene-based electrode materials can reach a high reversible capacity (1013–1054 mAh/g) but it's rate still limited at a high charge/ discharge rate (>500 mA/g).[24, 25] Compared to the pristine graphene, the nitrogen-doped graphene (N-graphene) has been reported to increase battery capacities nearly twofold due to the enhanced intercalation of Li ions from introduction of N-atoms.[26] N-graphene has also been suggested for use in fuel cells and other energy devices.[27]

1.2 Ultra-Wide Bandgap Semiconductor (UWBGS): β-Ga_2O_3

β-Ga_2O_3 is a monoclinic crystal with space group C2/m containing 20 atoms per conventional unit cell shown in Figure 1.4. The unit cell of the stable phase β-Ga_2O_3, contains two crystallographically different Ga atoms in the asymmetric unit, one with tetrahedral and the other with octahedral coordination geometry.[28-30] The unit cell is composed of two types of gallium ions (Ga1 and Ga2) and three types of oxygen ions (O1, O2, and O3). This leads to an anisotropy of physical, optical, and electrical. [30-33]

Because of the large bandgap and the resultant large electrical breakdown strength, β-Ga_2O_3 emerged as a promising semiconductor which can sustain large voltages, making it attractive for high-power devices.[29] In contrast to the band gap ~3.4eV of GaN [34, 35], the β-Ga_2O_3 exhibits larger bandgap of ~4.8eV.[36] The larger breakdown voltage and the larger breakdown field (~8 MV/cm)[37] than GaN make the Baliga's figure of merit (FOM, which defines the material parameters to minimize conduction losses) of β-Ga_2O_3 (3200), four times larger than that of GaN (860) shown in Table 1.1.[35] The unique electronic/optical properties and the lower cost of manufacturing of bulk crystals of β-

Ga_2O_3 than that of GaN and SiC make it a promising candidate for high-power high-frequency devices, such as solar blind UV photodetectors,[38] power rectifiers,[39] gas sensors,[29, 40] as well as power MOSFETs and MESFETs (Figure 1.5).[41-43]

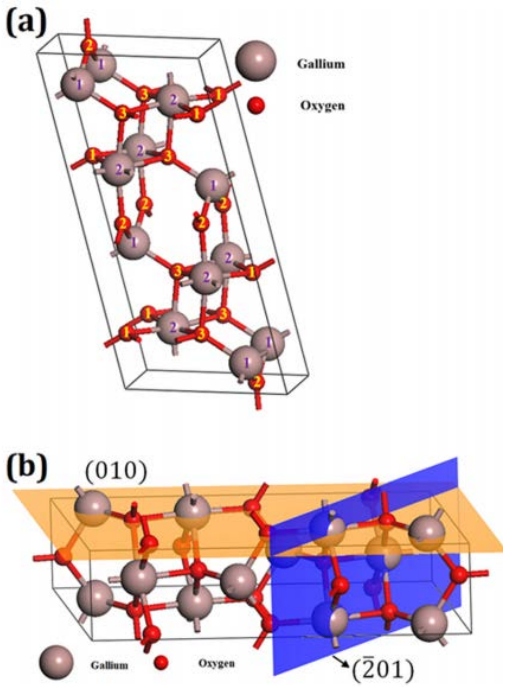

Figure 1.4 (a) β-Ga_2O_3 crystal structure and (b) (010) and $(\bar{2}01)$ surfaces. Copyright 2018 American Institute of Physics. [29]

Table 1.1 Material properties of major semiconductors and β-Ga_2O_3 [35]

	Si	4H-SiC	GaN	Diamond	β-Ga_2O_3
Band gap (eV)	1.1	3.3	3.4	5.5	4.8
Electron mobility ($cm^{-2}V^{-1}s^{-1}$)	1500	1000	1200	1800	300[a)]
Breakdown field (MV/cm)	0.3	3.0	3.3	10	8[a)]
Dielectric constant	11.8	10	9.5	5.5	10
Baliga's FOM (low freq.)	1	570	860	21000	3200

a) Estimated

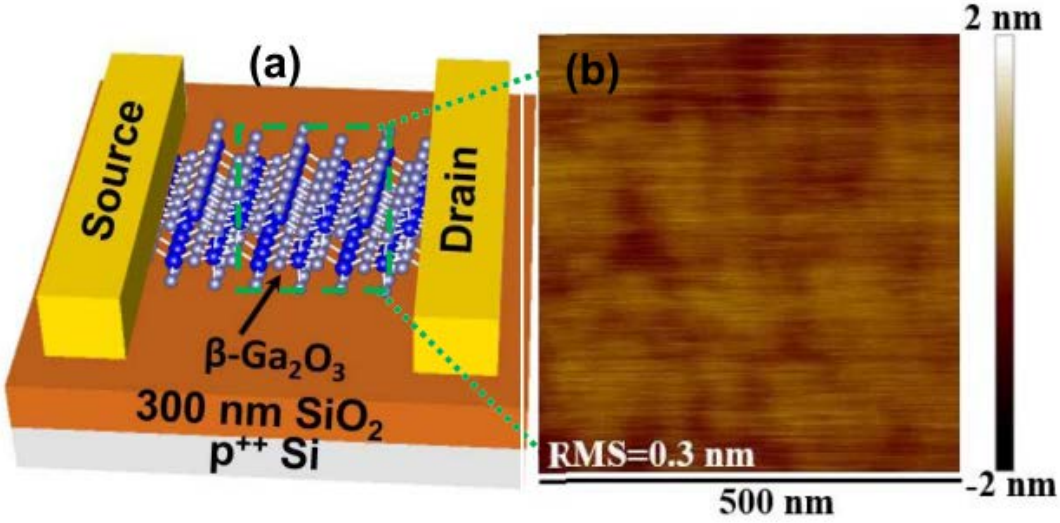

Figure 1.5 (a) Schematic view of a β-Ga_2O_3 on Insulator (GOOI) FET with a 300 nm SiO_2 layer on Si substrate and (b) AFM image of the atomic flat β-Ga_2O_3 surface after cleavage. Copyright 2017 IEEE.[44]

1.3 2-D Transition Metal Dichalcogenides (TMDs)

Molybdenum disulfide (MoS_2), as one of the promising two-dimensional (2D) materials, offers an alternative to graphene due to its unique electronic[45-48] and optical properties,[49-52] such as direct bandgap (~1.8 eV),[45, 48, 52] good mobility (~700 $cm^2\ V^{-1}\ s^{-1}$),[53] high current on/off ratio of 10^7–10^8,[54] large optical absorption (~$10^7\ m^{-1}$ in the visible range).[52, 55] Monolayer MoS_2 can be exfoliated from the bulk MoS_2 crystal as a result of the weak van der Waals interlayer interactions or can be grown on substrates using chemical vapor deposition.[56, 57] The large intrinsic bandgap and hexagonal planar lattice make it promising for flexible nano-electronic applications such as FETs with a high on-off ratio and low power consumption.[54, 58] Figure 1.6 shows the schematic and the cross-sectional view of the single layer MoS_2 transistor. The MoS_2 FETs have on/off-current ratios as high as 10^8.[54] MoS_2 transistors

exhibit a high field effect mobility (184 $cm^2 V^{-1} s^{-1}$) using scandium (Sc) as a metal contact, which can be increase to 700 $cm^2/(V \cdot s)$ by covering with a thin layer Al_2O_3.[53]

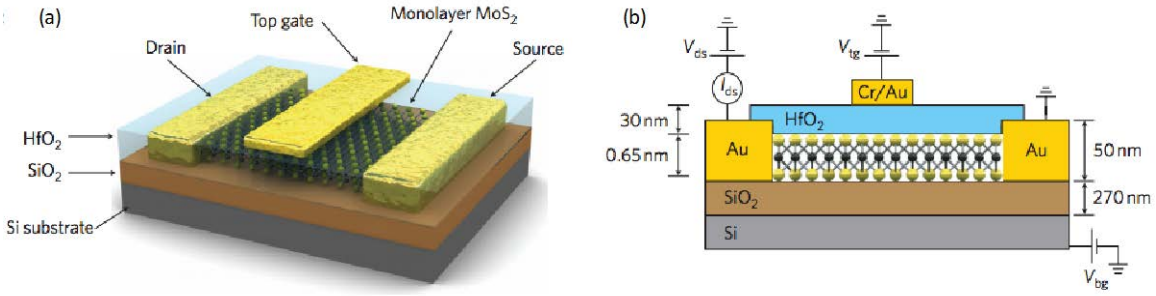

Figure 1.6 (a) Three-dimensional schematic view of single layer of MoS_2 transistors. (b) Cross-sectional view of the structure of a monolayer MoS_2 FET together with electrical connections used to characterize the device. A single layer of MoS_2 (thickness, 6.5 Å) is deposited on a degenerately doped silicon substrate with 270-nm-thick SiO_2. The substrate acts a back gate. One of the gold electrodes acts as drain and the other source electrode is grounded. The monolayer is separated from the top gate by 30 nm of ALD-grown HfO_2. The top gate width for the device is 4 mm and the top gate length, source–gate and gate–drain spacing are each 500 nm. Copyright 2011 Nature.[59]

$MoSe_2$ is another promising 2D TMDs. It exhibits unique electronic and optical properties such as an intrinsic band gap[60-63], strong photoluminescence (PL)[64] and efficient photovoltaic response[65, 66]. In contrast to an indirect gap ~1.1eV in bulk $MoSe_2$, the monolayer $MoSe_2$ exhibits direct bandgap of ~1.55eV.[60] The unique electronic/optical properties and atomic-thickness make it promising for flexible nano-electronic applications such as switchable transistors[64, 67], photodetectors[65], ultrathin photovoltaic (PV) devices[63, 66], as well as thermoelectric applications[68, 69]. Figure 1.7 shows the fabricated phototransistor based on exfoliated $MoSe_2$.[70] In addition, ultra-thin nanosheets of $MoSe_2$ show a room-temperature mobility of ~50 cm^2Vs^{-1},[67] which increases almost four-fold when the temperature decreases to 78 K. Therefore, the

monolayer $MoSe_2$ becomes the promising material in next-generation ultrathin nano-electronic devices.[71-76]

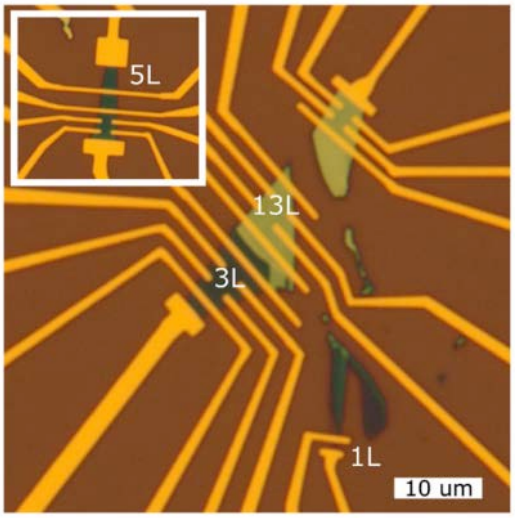

Figure 1.7 Optical micrograph of the fabricated phototransistors based on exfoliated $MoSe_2$. The crystal thicknesses range from monolayer (1L) to 13 layers. All the devices are fabricated on a single SiO_2/Si substrate. The Ti/Au contacts are fabricated on top of the $MoSe_2$ crystals, patterned by e-beam lithography. Copyright 2018 IOPscience.[70]

1.4 Motivation

As the device dimension scales down and power dissipation increases in the electronic devices, the inefficient thermal management becomes challenging for the performance and reliability in the application of nano-electronic devices using graphene, 2D-TMDs and UWBGS such as GaN and β-Ga_2O_3. In this section, the important factors that motivate the current research work is discussed.

1.4.1 Heat Removal through Graphene/h-BN Interfaces

Hexagonal boron nitride (h-BN) is an excellent dielectric substrate for graphene devices owing to its planar hexagonal lattice structure and atomically smooth surface. H-

BN has a small lattice mismatch (less than 2%) with the graphene [77]. Graphene sandwiched between h-BN layers could remove the equivalence of two carbon atoms in a unit cell to open a band gap and change its electronic properties[78, 79]. For example, an order of magnitude higher electron mobility has been observed in the graphene/h-BN devices than in graphene/SiO_2 devices [77]. Therefore, h-BN has a potential to lead to breakthrough in the applications of graphene-based devices.

Inefficient thermal management can become challenging for performance and reliability of graphene-based electronics. Graphene/h-BN contact may play an important role in heat dissipation in its electronic devices [80]. A fundamental understanding of phonon transport mechanism across graphene/h-BN interfaces is very important for improving heat dissipation. But very low thermal boundary conductance (TBC) has been reported using Raman spectroscopy technique, e.g., 7.4 $MW/m^2 \cdot K$ for the single layer graphene/h-BN interface, which may become a critical challenge for high frequency applications of graphene such as FETs and interconnects [81]. Moreover, only few studies have been focused on the prediction and analysis of TBC at graphene/h-BN interface. The TBC at multi-layer graphene (MLG)/h-BN interface has been calculated by Mao et al. [82] using the first principle method. The numerical simulations predict TBC as 186 $MW/m^2 \cdot K$, which is 24 times higher than the experimental value. Furthermore, previous studies found that the lattice stacking patterns of graphene on bulk h-BN are different in different parts within the same flake of the samples [77, 83-85]. Therefore, the actual value of TBC across the graphene/h-BN interfaces is the comprehensive result of different lattice stacking configurations. Theoretically, there are twelve different possible lattice stacking configurations for graphene sandwiched by h-BN which could influence the electronic

structures of SLG and lead to significant differences in electronic and thermal properties [86-90]. Electron-phonon coupling in three typical stacking configurations is analyzed by Slotman et al. [91]. They found that the phonon modes dominated by the nitrogen atoms have the highest electron-phonon coupling constant which might be explained by the stronger force interactions between nitrogen and carbon than those between boron and carbon. However, the effects of lattice stacking on the phonon transmission, and the contributions of different phonon modes to TBC are not well understood yet.

1.4.2 Effect of Interfacial Electronic Properties on Phonon Transport of MoS_2/Metal Interfaces

Due to the low TBC at the interface of the multilayer MoS_2 and its metal contacts[92], an inefficient heat removal through the interface can become a challenge for the performance and reliability of MoS_2-based nano-electronic devices. Only few studies [92], nevertheless, have focused on analyzing thermal transport and predicting TBC at the interface of monolayer MoS_2 and metal substrates.

MoS_2 transistors exhibit very high field effect mobility (184 ~ 700 $cm^2 V^{-1} s^{-1}$) using scandium (Sc) as a metal contact.[53] However, in contrast to the electron mobility of bulk MoS_2 crystal, that of monolayer MoS_2 ranges from 0.5 $cm^2/(V \cdot s)$ [56, 93] to 200 $cm^2/(V \cdot s)$[58] using myriad types of metal contacts. In addition, the research showed that the band structure of monolayer MoS_2 is also influenced by metal contacts.[94] The carrier mobility of a field-effect transistor is limited by scattering from phonons,[95] which are considered the dominant energy carriers for interfacial thermal transport.[96, 97] Therefore, it is necessary to establish a fundamental understanding of the inherent

connection between electronic properties and phonon transport at the interface of monolayer MoS_2 and its metal substrates in order to improve heat dissipation and device performance. Furthermore, the interfacial lattice-stacking configurations significantly influence electronic properties [79, 86, 90] and phonon transmission [98] for graphene-based devices. Our understanding of the effects of lattice-stacking on the interface of monolayer MoS_2/metals is far from being completed.

1.4.3 Effect of Point Defects on Thermal Conductivity of Bulk β-Ga_2O_3

High power dissipation in β-Ga_2O_3-based high-power high-frequency devices can cause critical challenges.[99] The relatively low thermal conductivity of β-Ga_2O_3 (one tenth of GaN[100, 101]) can lead to excess self-heating that must be mitigated in order to utilize β-Ga_2O_3 in high-frequency devices.[102] Various thermal management approaches need to be investigated for the β-Ga_2O_3 devices, similar to but probably more innovatively compared to what has been done with the GaN power devices to enable effective heat removal during high power operation.[103-105] Therefore, it's necessary to understand the thermal transport in β-Ga_2O_3 to better control the hot spot temperature in its active devices and for the design of packaging and thermal solutions. A few studies have focused on the prediction and the measurement of the thermal conductivity of β-Ga_2O_3. A recent computational DFT simulation reported a thermal conductivity of bulk β-Ga_2O_3 by solving the linearized Boltzmann transport equation.[106] However, the results didn't have a great agreement with the experimental results.[107-109] And the mechanism of the phonon transport in β-Ga_2O_3 is not well understood yet.

Due to the imperfection of growth processes, point vacancies[110, 111] may exist in the β-Ga_2O_3 which can provide promising opportunities for tailoring its electrical properties such as band structure [112], conductivity [111, 113-115], and optical properties [116] such as luminescence spectrum [117] for various device applications. However, the point defects like oxygen and gallium vacancies could suppress the thermal transport, reduce thermal conductivity and make the thermal management even more challenging.[118, 119] No study has focused on exploring the effect of point vacancies on the thermal transport in bulk β-Ga_2O_3. The understanding of how oxygen and gallium vacancies suppress the thermal transport in bulk β-Ga_2O_3 is far from being completed.

1.4.4 Influence of Defects and Doping on Phonon Transport Properties of Monolayer $MoSe_2$

Phonons are expected to be the dominant energy carriers for the thermal transport in 2D TMDs.[76, 120-122] A fundamental understanding of phonon transport properties of the monolayer $MoSe_2$ is of great importance for improving reliability and energy efficiency of the $MoSe_2$-based devices. A recent theoretical study reported a relatively low thermal conductivity of monolayer $MoSe_2$ (54 W/mK at room temperature) compared to other 2D TMDs by solving Peierls-Boltzmann transport equation (PBTE) calculations.[120] A much lower thermal conductivity of 17.6 W/mK[121] is obtained using Slack model.[123, 124]

In addition, due to the imperfection of growth processes, the crystal lattice of monolayer TMDs contains unintentional localized defects such as vacancies[125-129], dislocation cores and grain boundaries[130] which could further suppress the thermal transport.[131, 132] Peng, et.al. found that the defect-induced quasi-localized phonon

states have a significant influence on reducing the thermal conductivity of MoS_2 from the first-principles calculations. [131] Ding, et.al. used non-equilibrium molecular dynamics simulations to demonstrate that thermal conductivity of monolayer MoS_2 can be effectively tuned by introducing phonon–defect scattering.[132] However, very few studies has focused on exploring the effect of defects on the thermal transport in monolayer $MoSe_2$. In addition, a fully parameter-free defect model is needed to examine and improve the empirical defect model to estimate the thermal properties considering the influence of defects.

The defect engineering for Selenium vacancies in the monolayer $MoSe_2$ can provide promising opportunities for tailoring its properties for various device applications.[133-135] Isoelectronic doping is one of the most effective strategies to suppress or to manage the vacancy concentration [136] and precisely tailor its properties for desired applications, such as enhancing the photoluminescence (PL), modulating the carrier type and raising the carrier lifetime.[126-128, 137] However, the understanding of the effects of isoelectronic doping process on the thermal transport properties of monolayer $MoSe_2$ is far from being completed.

1.5 Objectives and Scope of Thesis

The thesis is aimed to investigate the role of interfaces and defects on the thermal transport in nano-electronic semiconducting materials such as graphene, 2-D TMDs and β-Ga_2O_3. First-principles density functional theory (DFT), atomistic Green's function (AGF) and phonon Boltzmann transport equation (BTE) simulations are used to fulfill the objectives.

The thesis is organized in following sequence. Chapter 2 reviews the literature regarding the experimental measurements and theoretical simulations of the thermal transport at graphene/h-BN interfaces, MoS_2/metal interfaces and the monolayer MoS_2 and bulk β-Ga_2O_3. It also summarizes the important contributions of the present work. Chapter 3 presents the atomistic models to study the thermal transport in nano-electronic materials and interfaces. Chapter 4 includes results and discussion of phonon transport at the interfaces of vertically stacked graphene/h-BN heterostructures. Chapter 5 includes results and discussion on how the interfacial electronic properties influence the phonon transport at monolayer MoS_2 with metal substrates. Chapter 6 presents results and analysis on phonon mode contributions to thermal conductivity of pristine and defective β-Ga_2O_3. Chapter 7 contains the results and analysis on the effects of point defects and tungsten doping on phonon transport properties of monolayer $MoSe_2$. Chapter 8 presents the fully parameter-free first-principles study of phonon transport of monolayer $MoSe_2$ with different types of defects and the improvement of empirical defect model. Chapter 9 summarizes the current work and includes discussion on the scope of future work.

CHAPTER 2 : BACKGROUND

The recent experimental measurements and theoretical simulations on nano-electronic semiconducting materials such as Graphene, 2D TMDs (MoS_2 and $MoSe_2$), and UWBGS (β-Ga_2O_3) are focused on elucidating phonon transport mechanism in order to better understand the heat dissipation in their devices. Another important focus of many studies are the effects of interfaces, defects and doping, which may further suppress the thermal transport in these devices.

In this Chapter, a literature survey is presented to summarize the recent experimental and theoretical studies on the phonon-mediated thermal transport at graphene/h-BN interfaces, MoS_2/metal interfaces and the monolayer MoS_2 and bulk β-Ga_2O_3. It followed by a summary of the contribution of current thesis work.

2.1 Experimental Study and Atomistic Modeling of Thermal Transport at Graphene/h-BN Interfaces

Due to the atomically smooth surface and the small lattice mismatch (less than 2%) with the graphene, h-BN can be used an excellent dielectric substrate for graphene-based FETs to improve the mobility [77, 138, 139]. For example, an order of magnitude higher electron mobility has been observed in the graphene/h-BN devices than in graphene/SiO_2 devices [77]. A prototype bipolar FET of graphene heterostructures with atomically thin BN is reported to improve the switching ratios at room temperature for high-frequency operation.[140] In addition, a theoretical modeling [141] and an experimental measurement [142] are conducted to report the Seebeck coefficient of graphene/*h*-BN/graphene heterostructures.

Graphene/h-BN contact may play an important role in heat dissipation in its electronic devices [80]. Zhang et al. [143] reported the direct growth of large-area graphene/h-BN vertical heterostructures by a co-segregation method. The first experimental measurement of TBC at graphene/h-BN interface was performed by Chen et al. using Raman spectroscopy.[81] They reported a TBC value of 7.4 MW/(m^2·K) for the graphene/h-BN interface. The low TBC which is away from most simulation results is attributed to the impurities resulting from the transfer process by the authors. Recently, a TBC value of 52.2 MW/(m^2·K) at the interface of graphene/h-BN is measured by Liu et al. using the same Raman technique.[144] In addition, Kim et al. [145] preformed the *in situ* spatially resolved Raman thermometry on an electrically biased graphene channel and its h-BN substrate to study the energy dissipation mechanism in graphene/h-BN heterostructures. They observed a TBC of 5-10 MW/(m^2·K) from 100 °C to 600 °C in air. They found that a doping effect occurred under a strong electric field played a crucial role in the energy dissipation in the graphene/hBN device up to 600 °C. Furthermore, David et al. reported a room temperature TBC of 35.1 MW/(m^2·K) which lies in between the previously reported experimental values by using time-domain thermoreflectance (TDTR) method.[146]

On the other hand, only a few theoretical studies have been focused on the prediction and analysis of TBC at graphene/h-BN interface. The TBC at multi-layer graphene (MLG)/h-BN interface has been calculated by Mao et al. [82] using the first-principles DFT and AGF method. The numerical simulations predict TBC as 186 MW/m^2·K, which is much higher than the experimental value. One reason for this difference could be the roughness and contaminants at the interface or the defects of the

samples which may influence the experimental results [147, 148]. Another reason could be that multi-layer graphene in numerical studies has different thermal properties compared with the single layer graphene (SLG) used in the experiments [149, 150]. Furthermore, previous studies found that the lattice stacking patterns of graphene on bulk h-BN are different in different areas within the same flake of the sample, as shown in Figure 2.1, which is not the same as the assumption of "perfect" matching in the theoretical calculations [77, 83-85]. Therefore, the actual value of TBC across the graphene/h-BN interface is the comprehensive result of different lattice stacking configurations.

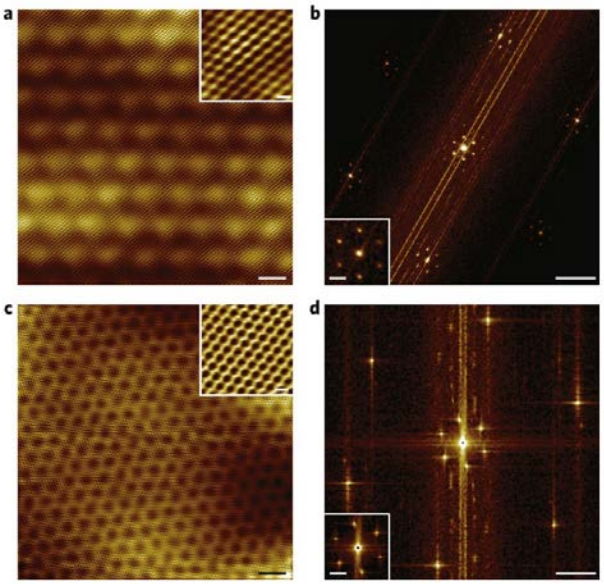

Figure 2.1 (a) STM topographic images of a Moiré pattern produced by graphene on hBN. The scale bar is 2 nm. The inset is a zoom in of a 2 nm region with a scale bar of 0.3 nm. The imaging parameters are V_t=−0.3 V and I_t=100 pA. (b) Fourier transform of a showing the six graphene lattice points near the edge of the image and the long wavelength Moiré pattern near the centre of the image and around each lattice point. The scale bar is 10 nm^{-1}. The inset is a zoom in around one of the lattice points with a scale bar of 2 nm^{-1}. (c) STM topographic image from another region of the same graphene flake showing a different Moiré pattern. The scale bar is 2 nm. The inset is a zoom in of a 2 nm region with a scale bar of 0.3 nm. The imaging parameters are V_t=−0.3 V and I_t=100 pA. (d) Fourier transform of c showing the atomic lattice as

well as the Moiré pattern. The scale bar is 10 nm^{-1}. The inset is a zoom of the Moiré pattern with a scale bar of 4 nm^{-1}. Copyright 2010 Nature.[151]

Theoretically, there are twelve different possible lattice stacking configurations for graphene sandwiched by h-BN which could influence the electronic structures of SLG and lead to significant differences in electrical and thermal properties [86-90]. Electron-phonon coupling in three typical stacking configurations is analyzed by Slotman et al. [91]. They found that the phonon modes dominated by the nitrogen atoms have the highest electron-phonon coupling constant which might be explained by the stronger force interactions between nitrogen and carbon than those between boron and carbon. Another theoretical simulation is conducted by Zhang et al. [152] to predict the TBC across stacked graphene nanoribbon (GNR) and h-BN interfaces. They reported a TBC of 5 $MW/m^2 \cdot K$ for the bilayer system at room temperature using classical molecular dynamics simulations.

2.2 Experimental Study and Atomistic Modeling of Thermal Transport in 2-D TMDs

As a family of novel 2D materials beyond graphene, the 2-D TMDs become promising due to their unique physical properties and potential applications. [153, 154] The electrical properties of 2D-TMDs have been studied extensively,[54, 58, 59, 65, 66, 94, 155-157] but much less attention has been given to the thermal properties until recently. Sahoo et al. [158] reported the in-plane thermal conductivity of high-quality few-layer MoS_2 is about 52 W/mK at room temperature using Raman spectroscopy. The first-order temperature coefficients for E_{2g} and A_{1g} modes were found to be (1.32 and 1.23) × 10^{-2} cm^{-1}/K, respectively. The room temperature thermal conductivity of suspended monolayer

MoS_2 is measured as 34.5±4 W/mK using Raman spectroscopy.[159] Another research reported the 84±17W/mK by using refined optothermal Raman technique.[160]

Gu et al.[120] systematically study the phonon transport of eight semiconducting single-layer TMDs, MX_2 (M=Mo, W, Zr, and Hf, X=S and Se) using the first-principles DFT along with phonon BTE calculation as shown in Figure 2.2. They reported that the thermal conductivities of 2H-type TMDs are above 50W/mK at room temperature (MoS_2, 103W/mK) while the thermal conductivity values of the 1T-type TMDs are much lower. A very high thermal conductivity value of 142 W/mK was found in single-layer WS_2 due to the large atomic weight difference between W and S, which leads to a large phonon bandgap between acoustic and optical phonon modes resulting in very long phonon relaxation. Li et al. [122] studied the size effects on the thermal conductivity of monolayer MoS_2 by the DFT and iterative solution of BTE calculation. A room temperature thermal conductivity of 83 W/mK is reported with the size of 1μm.

In addition to the suspended monolayer MoS_2, the substrate also has significant influence on the thermal transport properties. The room temperature thermal conductivity of supported monolayer MoS_2 is reported as 62.2W/mK. [161] The value of the thermal conductivity of the supported MoS_2 monolayer was different with the previously determined value of a suspended MoS_2. This difference may also be associated with the different sample preparation and measurement procedures. The previous measurements of the suspended MoS_2 were performed under vacuum. This supported one was conducted in ambient air. This difference may substantially influence the measurement conditions and affect the obtained results.

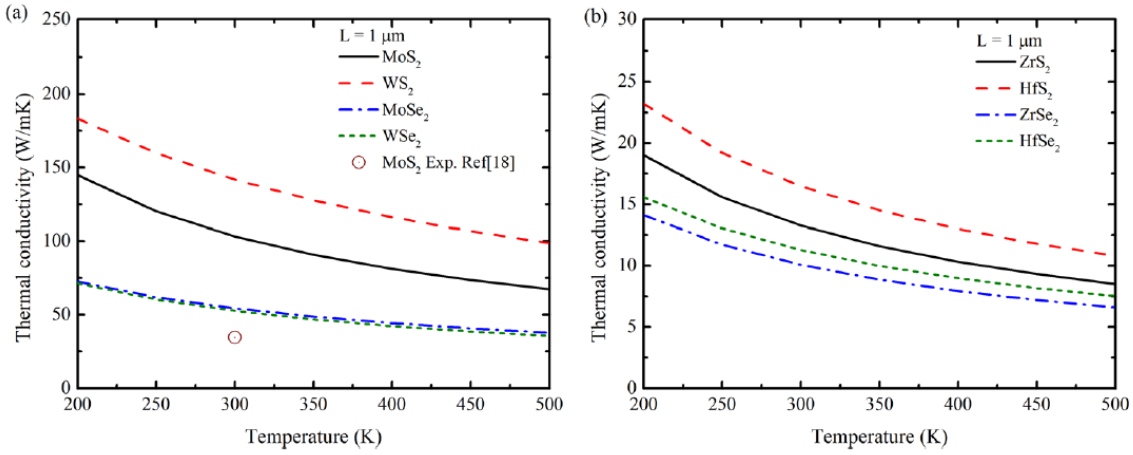

Figure 2.2 The thermal conductivity of (a) 2H and (b) 1T TMDC monolayers as a function of temperature.

Only few studies [92], nevertheless, have focused on analyzing thermal transport and predicting TBC at the interface of MoS_2 and metal substrates. Mao et al.[92] performed a theoretical calculation of thermal transport at the multi-layer MoS_2/metal interfaces using first-principles DFT calculation and Landauer formalism. They reported that the TBC of chemisorbed Sc/MoS_2, Ru/MoS_2 interfaces and physisorbed Au/MoS_2, Pd/MoS_2 interfaces are 52.6 MW/(m^2·K), 32.3 MW/(m^2·K), 17.2 MW/(m^2·K), 8.3 MW/(m^2·K), respectively at room temperature. They also identifies the presence of multiple distinct atomic planes and bonding patterns at the interface as the key origins of the observed large thermal resistance. Taube et al. [92] reported the TBC of MoS_2/SiO_2 interface as 1.94 MW/(m^2·K) by Raman measurement.

$MoSe_2$ is another promising 2D TMDs. The phototransistor based on $MoSe_2$ presents a much faster response time (<25ms) than the MoS_2 monolayer at room temperature. A room temperature thermal conductivity of 59±18 W/mK, [160] of monolayer $MoSe_2$ is measured by Raman spectroscopy, which is much lower than that of

monolayer MoS_2. The thermal conductivity reduces to 42±13 W/(m·K) for bilayer $MoSe_2$.[160] The low thermal conductivity of monolayer $MoSe_2$ is also calculated by different theoretical techniques such as (41 W/(m·K) from MD simulations,[162] and 54 W/mK from first-principles calculation[120]). In addition, a much lower thermal conductivity of 17.6 W/mK[121] is obtained using Slack model.[123, 124]

Due to the imperfection of growth processes, the crystal lattice of monolayer TMDs contains unintentional localized defects such as vacancies[125-129], dislocation cores and grain boundaries[130] which could further suppress the thermal transport.[131, 132] Peng et.al. found that the defect-induced quasi-localized phonon states have a significant influence on reducing the thermal conductivity of MoS_2 from the first-principles DFT calculations. [131] Using nonequilibrium MD simulations, Ding et al.[132] found that the thermal conductivity of monolayer MoS_2 can be effectively tuned by introducing even a small amount of lattice defects. A 0.5% concentration of mono-Mo vacancies is able to reduce the thermal conductivity by about 60% due to the reduction of the phonon relaxation time arising from phonon−defect scattering. A 12% tensile strain can reduce the thermal conductivity by another 60% due to the reduction of the group velocity and heat capacity. The defect engineering for Selenium vacancies in the monolayer $MoSe_2$ can provide promising opportunities for tailoring its properties for various device applications.[134, 163] Isoelectronic doping is one of the most effective strategies to suppress the vacancy concentration and precisely tailor its properties for desired applications.[126-128, 137] Yarali et al. [164] found that isoelectronic substitution of the W atoms for Mo atoms in CVD-grown $Mo_{0.82}W_{0.18}Se_2$ monolayers reduces the Se vacancy concentration by 50% compared to that found in the $MoSe_2$ monolayers. The thermal conductivity remains intact

in a wide temperature range (Figure 2.3). On the other hand, Se vacancies have a detrimental effect, which reduce the thermal conductivity up to 72% for a vacancy concentration of 4%.

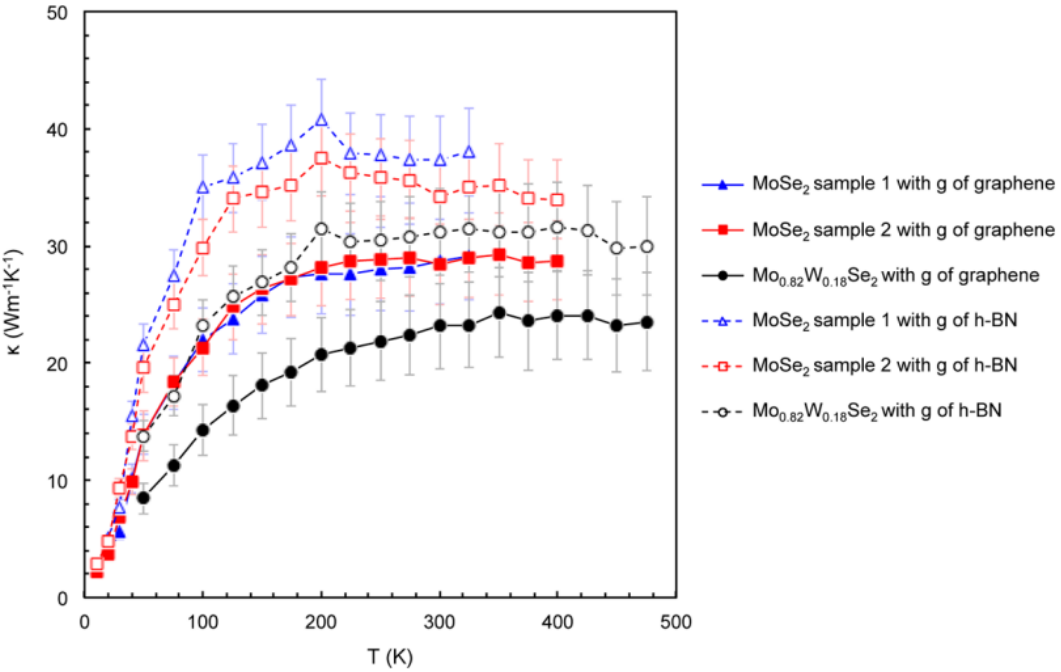

Figure 2.3 Intrinsic basal plane thermal conductivity of the samples as a function of temperature calculated with g of graphene for $MoSe_2$ sample 1 (filled triangles), $MoSe_2$ sample 2 (filled squares), $Mo_{0.82}W_{0.18}Se_2$ (filled circles), and g of h-BN for MoSe2 sample 1 (unfilled triangles), $MoSe_2$ sample 2 (unfilled squares), and Mo0.82W0.18Se2 (unfilled circles). Here, g is the used value of interfacial thermal conductance between the sample and the supporting membranes.

2.3 Experimental Study and Atomistic Modeling of Thermal Transport in β-Ga_2O_3

Due to the relatively low thermal conductivity of β-Ga_2O_3 which is one tenth of GaN[100, 101], the high power dissipation in β-Ga_2O_3 devices may cause critical challenges. Recently, a few studies have focused on the prediction and the measurement of the thermal conductivity of β-Ga_2O_3. As we expected, β-Ga_2O_3 shows a large anisotropy

due to the two crystallographically different Ga atoms in the asymmetric unit, one with tetrahedral and the other with octahedral coordination geometry. Guo et al. measured the thermal conductivities of β-Ga_2O_3 single crystals along three different crystal directions in the temperature range of 80-495 K using the time domain thermoreflectance (TDTR) method. They reported that the [010] direction has the highest thermal conductivity of 27±2.0 W/mK, while that along the [100] direction has the lowest value of 10.9±1.0 W/mK at room temperature. [001] direction has the thermal conductivity of 14.7±1.4 W/mK. They also found that the thermal conductivity follows a 1/T relationship characteristic of Umklapp phonon scattering, indicating phonon-dominated heat transport in the β-Ga_2O_3 crystal at high temperatures shown in Figure 2.2.

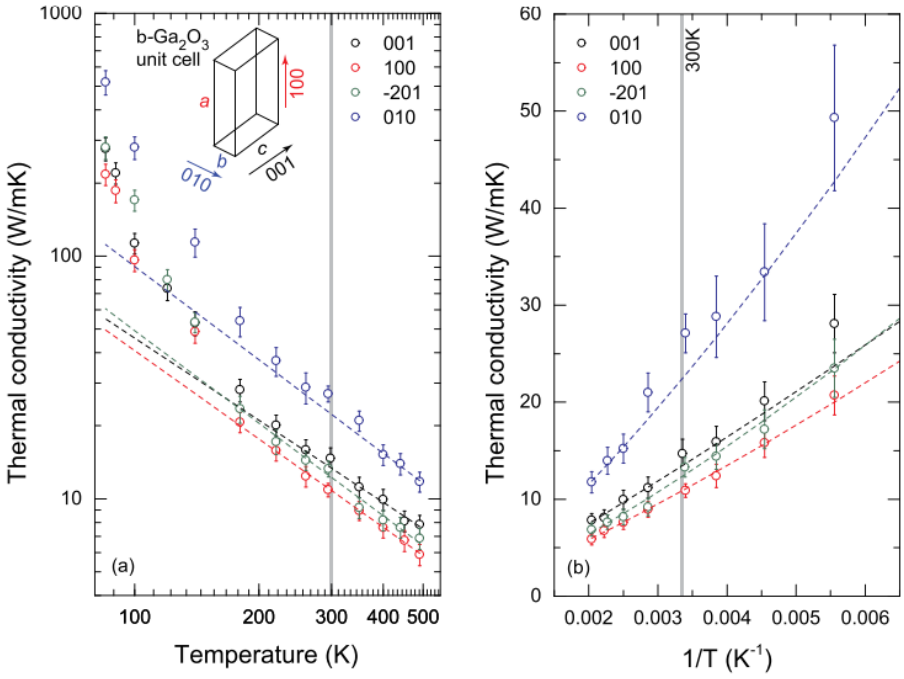

Figure 2.4 Temperature-dependent thermal conductivity of β-Ga_2O_3 measured along different crystal directions by the TDTR approach. In (a), the thermal conductivity and temperature are in the log scale. The inset shows a schematic of the unit cell of the β-Ga_2O_3 crystal. The thermal conductivity is larger along directions of smaller lattice constant: The

rough lattice constant ratios are c~2b and a~4b. The dashed lines show $1/T^m$ fits that capture the high temperature behavior of the thermal conductivity. The vertical dashed line separates the high-temperature behavior from the lower-temperature deviation to the fits. (b) Shows a linear plot of thermal conductivity against 1/T to highlight the dependence on temperature and the high-temperature $1/T^m$ fits more clearly.

Handwerg et al.[108] applied the electrical 3-ω method to obtain the thermal conductivity on Czochralski-grown β-Ga_2O_3 bulk crystals, which have a thickness of 200 μm and 800 μm. They reported a [100]-direction thermal conductivity of 13 ± 1 W/mK at room temperature for both Mg-doped electrical insulating and undoped semiconducting β-Ga_2O_3. The phonon contribution to the thermal conductivity dominates over the electron contribution below room temperature. A [100]-direction thermal conductivity of $(5.3\pm0.6)\times10^2$ W/mK is also observed at 25K due to weaker phonon-phonon-Umklapp scatterings.

Galazkae et al.[109] reported a room temperature thermal conductivity of bulk β-Ga_2O_3 along [010] direction, which is determined by NETZSCH-Gerätebau GmbH. Slomski et al. [32] measured the thermal conductivity of undoped, Sn-doped, and Fe-doped β-Ga_2O_3 bulk crystals by the 3-ω technique in the temperature range of 295-410 K. They found that the doped β-Ga_2O_3 has a slightly lower thermal conductivity compared to the undoped value of 29.21 W/mK along the [010] direction at the room temperature, which can be explained by enhanced phonon-impurity scattering contribution.

A recent computational study reported a thermal conductivity of 16.06 W/mK, 21.54 W/mK, 21.15 W/mK in the direction of [100], [010], [001], respectively at room temperature by solving the linearized Boltzmann transport equation along with the first-principles DFT calculation.[106] However, the results didn't have a great agreement with

the experimental results mentioned above. The summary of reported thermal conductivity of bulk β-Ga_2O_3 can be found in Table 2.1.

Due to the imperfection of growth processes, point vacancies [110, 111] may exist in the β-Ga_2O_3 which can provide promising opportunities for tailoring its electrical properties such as band structure[112], electrical conductivity [111, 113-115], and optical properties [116] such as luminescence spectrum [117] for various device applications. However, no study has been reported on the effects of the point defects like oxygen and gallium vacancies on thermal properties of bulk β-Ga_2O_3.

Table 2.1 Thermal conductivity of the bulk β-Ga_2O_3 at room temperature from literatures

Crystallographic orientation	Experiment	Simulation[106]
[100]	10.9± 0.7,[107] 13± 1.[108]	16.06
[010]	27.1± 2,[107] 21,[109] 29.21[32]	21.54
[001]	14.7±1.4.[107]	21.15

2.4 Contributions of Current Work

The major contributions and important findings of the current work are listed below.

In the study of thermal transport at graphene/h-BN interfaces:

(1) The atomistic framework based on the first-principles DFT and AGF is developed to investigate the impact of different lattice stacking configurations on the thermal transport across the vertically stacked h-BN/graphene/h-BN interfaces. This is the

first time that both frequency and wave vector dependent transmission for graphene/h-BN stacked interfaces is obtained to decipher the phonon modes contribution to TBC with different lattice stacking configurations. The findings clearly indicate how the interfacial lattice matching configurations impact the phonon-phonon coupling, phonon transmission and TBC at SLG/h-BN interfaces.

In the study of interfacial electronic properties on phonon transport at MoS_2/metals interfaces:

(2) The first-principles DFT and AGF simulation are used to elucidate the inherent connection between electronic structure and phonon properties at the interface of monolayer MoS_2 and its metal substrates (Au and Sc). The findings, for the first time, demonstrate that how characteristics of interfacial electronic structure and charge transfer between monolayer MoS_2 and metallic substrates significantly impact the phonon distribution/transmission, and TBC.

In the study of phonon mode contributions to thermal conductivity of pristine and defective β-Ga_2O_3:

(3) The first-principles DFT along with BTE simulation are performed to investigate the phonon transport properties of pristine and defective β-Ga_2O_3. The model for estimating the effect of point vacancies on phonon properties is developed by considering contributions of the defect-induced phonon scatterings. This study, for the first time, reports how the defects influence the thermal conductivity of β-Ga_2O_3, and how the modal contributions change in the presence of defects. The results from this work will help us to understand the mechanism of phonon transport considering the influence of defects

and to provide insights for the future design of β-Ga_2O_3-based high electron mobility transistors.

In the study of influence of defects and doping on phonon transport properties of monolayer $MoSe_2$:

(4) The first-principles DFT along with the phonon BTE is used to study the phonon transport properties of monolayer $MoSe_2$ considering the effects of phonon scattering by the boundary, defects, and Tungsten (W) doping. The model for estimating the effect of Se vacancies is developed by considering contributions of two different types of the defect-induced phonon scatterings. The results in this work, for the first time, report how the defects influence the thermal conductivity of monolayer $MoSe_2$, and how the W doping and resulting change in defect concentration can tune its thermal properties.

(5) The fully parameter-free first-principles DFT simulation and BTE calculation are performed to investigate the impact of different types of Se vacancies on the thermal conductivity of monolayer $MoSe_2$. The findings help us understand how the vacancy-induced phonon states affects the mechanism of phonon transport of $MoSe_2$. Furthermore, a modified empirical model of defects is developed, for the first time, which leads to a better match to the fully parameter-free DFT simulation results. This work provide insights and directions for validating and improving the empirical defect model for predicting thermal properties , which could be used for the future design of $MoSe_2$-based electronics.

CHAPTER 3 : METHODOLOGY

Atomistic Green's function (AGF), and Boltzmann transport equation (BTE) based methods are popular approaches to study the thermal transport at nano-scale. The AGF method is efficient in handling interface scatterings at complicated interface structures considering the chemistry at the interface, e.g., MoS_2/metal and graphene/h-BN interfaces in this work. The BTE based method is efficient to describe the phonon behavior including anharmonicity in the bulk semiconducting materials, e.g., monolayer $MoSe_2$, bulk β-Ga_2O_3 in this work. In this section, AGF and BTE methods will be briefly discussed in the context of simulation of thermal transport. The specific approaches to determine TBC and thermal conductivity will be introduced. In the absence of empirical potential models, the first-principles density functional theory (DFT) based calculations are used to determine the equilibrium atomic positions and interatomic force constants. The second order interatomic force constants (IFCs) and third order IFCs can be calculated by the finite difference method using DFT calculation.

3.1 Density Functional Theory Calculation for Interatomic Interactions

Computational quantum mechanics is a fundamental method to predict electronic structure and material properties. The electronic structure of material at ground state can be obtained by minimizing the energy eigenvalues of the time-independent Schrödinger equation [165]

$$\hat{H}\Psi\left(r_1, r_2, ..., r_N\right) = E\Psi\left(r_1, r_2, ..., r_N\right) \quad \textbf{(3-1)}$$

According to Hohenberg and Kohn theorems, [166] DFT has been developed as an alternative approach to solve Schrödinger equation using ground state electron density. To solve the many-body problem, the DFT 1) approximated the Hamiltonian of an interacting many-body system with that of a non-interacting system; 2) incorporate the interactions into an exchange-correlation functional of electron density instead of electron wave function. The density of electrons at a particular position in space can be written as[167]

$$n(r) = 2\sum_i \psi_i(r)\psi_i^*(r) \qquad \textbf{(3-2)}$$

The electron density that minimizes the energy of the overall functional is the true electron density corresponding to the full solution of the Schrödinger equation. The Kohn-Sham expression for the energy functional is [166, 167]

$$E[n(r)] = T_s[n(r)] + V_{ext}[n(r)] + V_H[n(r)] + V_{xc}[\rho] \qquad \textbf{(3-3)}$$

where T_s , V_{ext} , and V_H are functionals of kinetic energy, interaction with external potential, and Hartree energy, respectively. The exchange-correlation functional [165] V_{xc} represents the correction for approximating kinetic energy and electron interaction with a non-interacting kinetic energy and classical electron-electron interaction. Local density approximation (LDA) and generalized gradient approximation (GGA) are the most popular treatment of V_{xc}. The K-S equation can be solved by the self-consistent iterations shown in Figure 3.1.

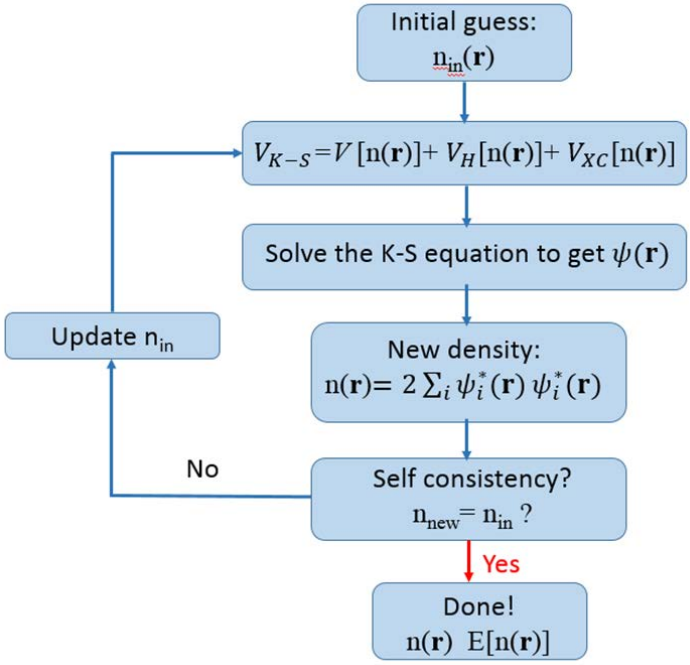

Figure 3.1 The workflow of self-consistent iteration.

In this work, we use DFT to calculate the second order force constants $\Phi_{ij}^{\alpha\beta}$ and third order force constants $\Phi_{ijk}^{\alpha\beta\gamma}$ for the harmonic matrix of AGF calculations and anharmonicity for the BTE simulation by the finite displacement method. [168] [169, 170]

$$\Phi_{ij}^{\alpha\beta}=\frac{\partial^2 E}{\partial r_i^{\alpha}\partial r_j^{\beta}} \qquad \Phi_{ijk}^{\alpha\beta\gamma}=\frac{\partial^3 E}{\partial r_i^{\alpha}\partial r_j^{\beta}\partial r_k^{\gamma}} \tag{3-4}$$

In harmonic approximation, the normal mode frequency and polarization of the phonon modes can be determined by harmonic lattice dynamics. In the dynamical equations, the equation of motion of the *j*th atom in *l*th unit cell is [171]

$$m_j\ddot{u}_{jl}=\sum_{j'}\sum_{k'}\Phi\left(jl,j'l'\right)\cdot u_{jl} \tag{3-5}$$

where u is the displacement of atom (j,l) with respective to its equilibrium position. $\Phi(jl, j'l')$ is the second-order force constant matrix. The normal mode frequency $\omega(q,v)$ of phonon mode v at wave vector q can be obtained by diagonalization of the dynamical matrix $D_{jj'}^{\alpha\beta}(q)$ between atom j and j' in a selected unit cell. [171]

$$D_{jj'}^{\alpha\beta}(q) = \frac{1}{\sqrt{m_j m_{j'}}} \sum_{l'} \Phi_{jj'}^{\alpha\beta}(0,l') \exp\left(iq \cdot \left[r_{j'l'} - r_{j0}\right]\right) \quad \textbf{(3-6)}$$

3.2 Atomistic Green's Function (AGF) Calculation

The Green's function method is a mathematical tool that solves non-homogeneous differential equations [172]. In the AGF model as shown in Figure 3.2, the system consists of a device (D) region sandwiched between two contacts: left contact (LC) and right contact (RC). The semi-infinite region beyond LC or RC is defined as left contact bulk (LCB) or right contact bulk (RCB) which does not interact with the device region. Only the phonon scattering at interfaces is considered, and the phonon transport in device region and contacts is ballistic. The group of unit cells whose primitive atoms share the same z coordinate are considered to be in the same layer. A unit cell can interact with unit cells in the nearest layer on either side of it. The purpose of defining the unit cell layers is to write the harmonic matrices in a finite plane-wave form so that an efficient sampling in transverse Brillouin zone $\vec{k}_{\parallel} = (k_x, k_y)$ can be used to include the phonons with all wavelengths [173, 174]. Considering phonons are waves that propagate through the system, the dynamics of phonons, to the second order, can be described as [175]

$$\left(\omega^2 I - H\right)\tilde{u} = 0 \quad \textbf{(3-7)}$$

where ω, H, and $\tilde{u}$ are the angular frequency, harmonic matrix, and displacement, respectively. The Green's function can be solved as

$$G(\omega)=\left[\left(\omega^2+i0^+\right)I-H\right]^{-1} \tag{3-8}$$

where 0^+ is a small positive infinitesimal factor that introduces damping in the open system. Therefore, the Green's function in the atomistic model can be interpreted as the impulse response of the lattice dynamics equation (3-7). With the knowledge of Green's function, one can obtain the information of atom's displacements $\tilde{u}$ in the device region which consists of phonon vibrations including the effect of coupling with contacts [175].

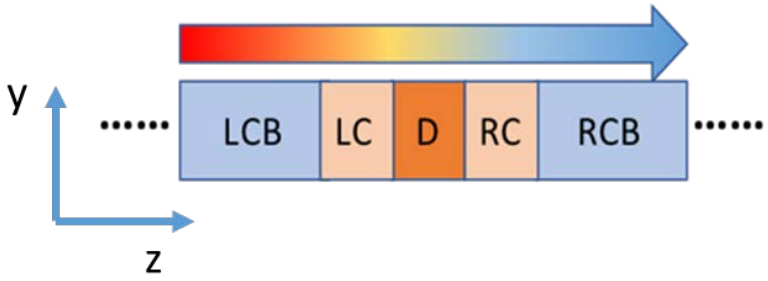

Figure 3.2 Schematic diagram of contact-device-contact sandwiched setup for the AGF calculations. The system is divided into a 'device' region (D), left contact (LC), right contact (RC), and two semi-infinite bulks, left contact bulk (LCB) and right contact bulk (RCB) which do not interact with the 'device' region.

The thermal conductance across the device region is determined by: [174, 176]

$$J=\int_0^\infty \int_{\vec{k}_\parallel} \frac{\hbar\omega}{2\pi}\left[N_L(\omega,T)-N_R(\omega,T)\right]\Xi\left(\omega,\vec{k}_\parallel\right)\frac{d\vec{k}_\parallel}{(2\pi)^2}d\omega \tag{3-9}$$

where $N(\omega,T)$ is the Bose-Einstein distribution function at frequency ω and temperature *T*. The subscript *L* and *R* mean the left and right contact. If the temperature difference between the contacts is sufficiently small, the phonon occupation difference in Eq. (3-9) becomes

$$N_L(\omega,T)-N_R(\omega,T)=\frac{\hbar\omega}{k_BT^2}\frac{e^{\hbar\omega/k_BT}}{\left(e^{\hbar\omega/k_BT}-1\right)^2}\Delta T \qquad \textbf{(3-10)}$$

$\Xi\left(\omega,\vec{k}_{\parallel}\right)$ is the transmission function at frequency ω and transverse k-point $\vec{k}_{\parallel}$.

$$\Xi\left(\omega,\vec{k}_{\parallel}\right)=\mathrm{Trace}\left[\Gamma_L G_{LD,RD}\Gamma_R G_{LD,RD}^{T}\right] \qquad \textbf{(3-11)}$$

where $G_{LD,RD}$ and $G_{LD,RD}^{T}$ are the part of the Green's function of device region and its complex conjugate. Γ_L and Γ_R are the interfacial phonon escape rate from the left and right contacts. They are defined as

$$\Gamma_{L(R)}\left(\omega,\vec{k}_{\parallel}\right)=i\left(\tau_{L(R)}-\tau_{L(R)}^{T}\right) \qquad \textbf{(3-12)}$$

$\tau_{L(R)}$ shows the change of phonon dynamical behavior caused by the left (right) contact, which is the element of the self-energy matrix in the sandwiched system's Green's function [174]. The harmonic matrices are constructed in a finite plane-wave form so that an efficient sampling in transverse Brillouin zone $\vec{k}_{\parallel}$ can be used to include the phonons of all wavelengths [177]. The Monkhorst-Pack scheme [178] is used to discretize the Brillouin zone. The TBC (σ) can be obtained by the definition

$$\sigma = \frac{J}{\Delta T} \tag{3-13}$$

3.3 Boltzmann Transport Equation

The phonon transport can be described by BTE considering the phonon scattering such as three phonon scattering, impurity scattering, defect scattering and boundary scattering. In this work, the full linearized Boltzmann transport equation is employed where the phonon relaxation time is used to include the scattering effects for each phonon mode. For the phonon mode, the BTE is shown as [179-181].

$$\frac{dn_\lambda}{dt} + \nabla T \cdot v_\lambda \frac{\partial n_\lambda}{\partial T} = \left.\frac{\partial n_\lambda}{\partial t}\right|_{scattering} \tag{3-14}$$

where v_λ is the group velocity of a phonon mode λ. n_λ is the phonon distribution function. The scattering term depends on the specific scattering processes due to phonon-phonon interactions and impurities. Under the assumption that the norm of ∇T is small enough, the n_λ can be expanded to the form of [181, 182]

$$n_\lambda = n_\lambda^0 - \mathrm{F}_\lambda \cdot \nabla T \cdot \frac{dn_\lambda^0}{dT} \tag{3-15}$$

where

$$\mathrm{F}_\lambda = \tau_\lambda^0 (v_\lambda + \Delta_\lambda) \tag{3-16}$$

when only two-phonon and three-phonon processes are considered. n_λ^0 is the Bose-Einstein distribution function. τ_λ^0 is the phonon lifetime. The Eq. (3-16) is solved

iteratively starting with Δ_λ. More details can be found in Ref.[181]. The phonon relaxation times and thermal conductivities can be calculated using Fermi's Golden rule [183] with the RTA and iterative solution of the BTE[122, 181, 184, 185]. The three-phonon scattering rates are

$$\Gamma^{\pm}_{\lambda\lambda'\lambda''} = \frac{\hbar\pi}{4N_0} \frac{\left|V^{\pm}_{\lambda,\lambda',\lambda''}\right|^2 \left(n^0_{\lambda}+1\right)\left(n^0_{\lambda'}+1/2\pm1/2\right)n^0_{\lambda''}}{\omega_\lambda \omega_{\lambda'} \omega_{\lambda''}} \times \delta\left(\omega_\lambda \pm \omega_{\lambda'} - \omega_{\lambda''}\right) \quad \textbf{(3-17)}$$

where N_0 is the number of unit cells, n^0_λ is the Bose-Einstein distribution function depending on the phonon angular frequency ω_λ. The delta function corresponds to the three-phonon processes that ensures conservation of energy. The three-phonon scattering matrix $V_{\lambda,\lambda',\lambda''}$ indicates the strength of the scattering events and is given by

$$V_{\lambda,\lambda',\lambda''} = \sum_{0k}\sum_{l'k'}\sum_{l''k''}\sum_{\alpha\beta\gamma} \Phi_{\alpha\beta\gamma}\left(0k, l'k', l''k''\right) \times \frac{e^{\lambda}_{\alpha k} e^{\lambda'}_{\alpha k'} e^{\lambda''}_{\alpha k''}}{\sqrt{M_k M_{k'} M_{k''}}} e^{i\vec{q}'\cdot\vec{R}_{l'}} e^{i\vec{q}''\cdot\vec{R}_{l''}} \quad \textbf{(3-18)}$$

where notation $\Phi_{\alpha\beta\gamma}\left(0k, l'k', l''k''\right)$ are third-order anharmonic IFCs, l and k specifies the k^{th} atom in the l^{th} unit cell. $e^{\lambda}_{\alpha k}$ is the α^{th} component of the phonon eigenvector for the k^{th} atom of the unit cell in mode λ, and $\vec{R}_l$ indicates the location of l^{th} unit cell.

The thermal conductivity tensor of the $\alpha\beta$ direction can be calculated as a sum of the contribution of all phonon modes λ [122]

$$\kappa_{\alpha\beta} = \frac{1}{N\Omega k_B T^2} \sum_{\lambda} n^0_\lambda (n^0_\lambda + 1)(\hbar\omega_\lambda)^2 v^{\alpha}_{\lambda} \mathrm{F}^{\beta}_{\lambda} \quad \textbf{(3-19)}$$

where N is the number of uniformly spaced q points in the Brillouin zone, Ω is the volume of the unit cell, k_B is the Boltzmann constant. v_λ^α is the group velocity along the α direction. The calculation stops at $F_\lambda^\beta = v_\lambda^\beta \tau_\lambda$ under the relaxation time approximation.

CHAPTER 4 : PHONON TRANSPORT AT THE INTERFACES OF VERTICALLY STACKED GRAPHENE AND HEXAGONAL BORON NITRIDE HETEROSTRUCTURES

In this chapter, the phonon transport at the interface of SLG sandwiched between h-BN layers is investigated with different lattice stacking configurations. First-principles density functional theory (DFT) and atomistic Green's function (AGF) simulations are used to investigate the phonon transmission and TBC of h-BN/SLG/h-BN interfaces. Five representative configurations are chosen from the twelve possible lattice stacking configurations. The phonon dispersion relations and density of states (DOSs) of SLG sandwiched between the h-BN layers are analyzed in different lattice stacking configurations. Furthermore, both frequency and wave-vector (k space) dependent transmission for graphene/h-BN interfaces are reported and the contributions of different phonon modes to TBC are analyzed in different configurations.

4.1 Computational Methods and Simulation Setup

4.1.1 Structure Optimization and IFCs Calculation of the Graphene/h-BN Interface

The Vienna ab initio simulation package (VASP) is used to perform the DFT calculations [186, 187]. A plane wave basis set and the projector augmented-wave (PAW) method are used with the local density approximation (LDA) exchange–correlation functional [188, 189]. The LDA shows a reasonable structural properties for the system near the equilibrium [186, 190], especially for the interlayer distance in systems like graphite [191] and h-BN [192], although LDA tends to underestimate the interlayer binding

energies and band gaps of graphite and h-BN due to the lack of description of van der Waals forces, which are the manifestation of long-range correlation effects [85, 86, 193]. Interfacial TBC in this study is strongly dependent on interlayer distance, and LDA leads to a very good performance in calculating interlayer distance and force constants [82, 85, 149]. The optimized in-plane lattice constant of graphene and bulk h-BN are $a_{\mathrm{SLG}} = 2.45$ Å, $a_{\text{h-BN}} = 2.49$ Å and $c_{\text{h-BN}} = 3.26$ Å which are in good agreement with the simulation and experimental results from the previous studies [57, 85, 194]. The optimized lattice constant of h-BN ($a = 2.49$ Å) is used in the sandwiched systems, where the SLG is under less than 2% strain. The kinetic energy cutoff of 500 eV and a 25×25×1 k-point grid are used to optimize the h-BN/graphene/h-BN sandwiched structures. The unit cell of these sandwiched structures contains two carbon atoms, eight h-BN layers with one boron and one nitrogen atoms in each layer (Figure 4.1). The distance between the graphene and h-BN substrates is optimized for the unit cell system shown in Figure 4.1. Using this optimized equilibrium structure, a 5x5 supercell of a graphene sheet sandwiched by 8 layers of h-BN bulks (Figure 4.2) is assembled for the calculations of the second order IFCs. This supercell contains 450 atoms and a vacuum region of 16 Å. The 3×3×1 k-point grids are applied to sample the Brillouin zone of this supercell. For IFCs of the h-BN bulk, a 5×5×4 supercell with the periodic boundary conditions and 3×3×1 k-point grids are used. To calculate the IFCs, we displace each atom in a unit cell into two directions: one in plane and one orthogonal to the plane of the graphene layer. The displacement length is 0.01 Å. The kinetic energy cutoff of the 5×5 supercell is 450 eV. The system energy convergence criterion is set to be 1e-6 eV. The force convergence criterion is set to be -0.01eV/Å. Then,

using the IFCs obtained from the DFT calculations, the harmonic matrices are constructed which describe the interatomic interactions in the AGF calculations.

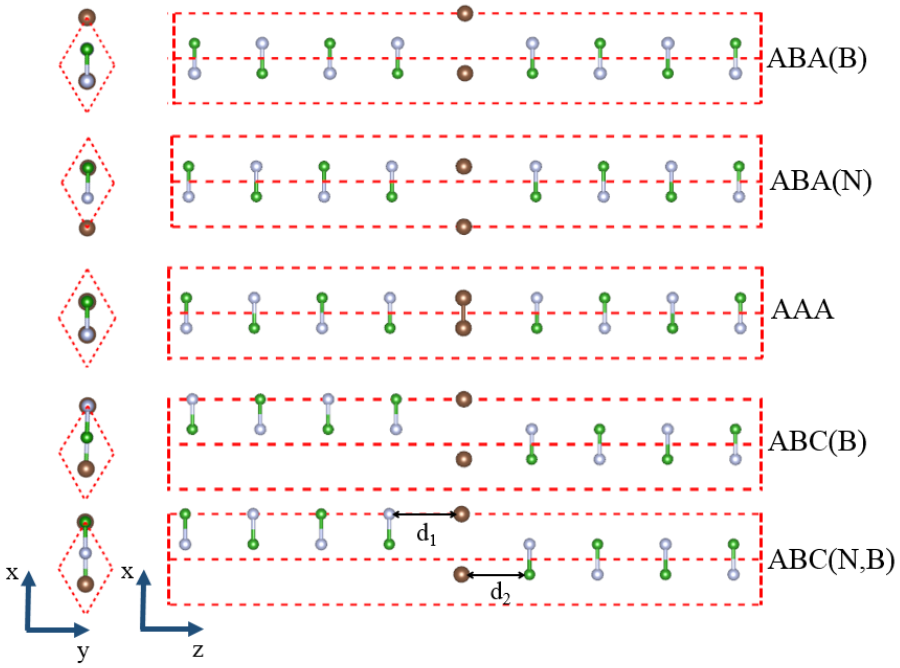

Figure 4.1 Side views of the five lattice stacking configurations of SLG sandwiched between h-BN layers in x-y plane and x-z plane. d_1 and d_2 presents the interfacial separation distances. The brown, green, and gray spheres represent carbon, boron, and nitrogen atoms, respectively.

4.1.2 Atomistic Green's Function (AGF) Calculation of the Graphene/h-BN Interface

The phonon transmission function and TBC are obtained from AGF calculations [149, 195], where graphene ('device') is sandwiched between two 'contacts' corresponding to the hot and cold thermal reservoirs represented by semi-infinite h-BN bulks (Figure 4.2). The heat flux *J* through the system carried by phonons is evaluated by Eq.(3-9). More details of AGF calculation can be found in Chapter 3.

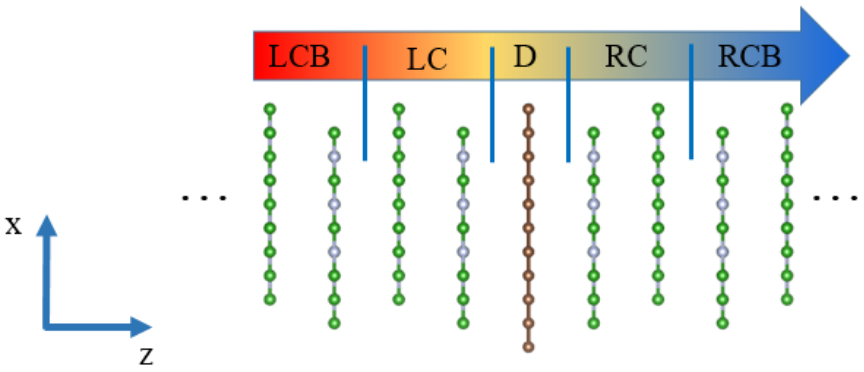

Figure 4.2 Schematic diagram of h-BN/SLG/h-BN sandwiched system for the AGF calculations. The system is divided into a 'device' region (D), left contact (LC), right contact (RC), and two semi-infinite h-BN bulks, left contact bulk (LCB) and right contact bulk (RCB) which do not interact with the 'device' region. The 'device' region only includes the SLG layer.

The harmonic matrices are constructed in a finite plane-wave form so that an efficient sampling in transverse Brillouin zone $\vec{k}_{\parallel}$ can be used to include the phonons of all wavelengths [177]. The Monkhorst-Pack scheme [178] is used to discretize the Brillouin zone with the mesh of 401×401. The frequency and wave vector (k space) dependent transmission $\Xi\left(\omega,\vec{k}_{\parallel}\right)$ can be computed which shows angular symmetry in the Brillouin zone. So, we present $\Xi\left(\omega,\vec{k}_{\Gamma-\mathrm{K}}\right)$ along $\Gamma-\mathrm{K}$ direction which is also convenient to compare with the phonon dispersion along $\Gamma-\mathrm{K}$ in a same figure. These results give us a detailed understanding of phonon mode contributions to the TBC.

4.2 Phonon Dispersion Relations and Phonon Density of states (DOSs)

After the structural optimization, the interfacial separation distance is 3.23Å for the ABA(B) and ABC(B), 3.45Å for the ABA(N), 3.51Å for the AAA. The ABC(N,B) has the

interfacial separation distance of 3.45Å at one side and 3.23Å at the other side because of the different configurations on different sides of the graphene layer. The structural optimization has a good agreement with the results from the previous studies [84-86, 196]. For example, Giovannetti's group [85] used the LDA as the exchange–correlation functional to calculate the interfacial separation distance of graphene/h-BN. For the structure ABA(B), ABA(N) and AAA, the value is 3.22Å, 3.40Å and 3.50 Å, respectively. Some important results of h-BN/graphene/h-BN sandwiched structure with different lattice stacking arrangements are shown in Table 4.1.

Table 4.1 Properties of h-BN/graphene/h-BN sandwiched structure with different lattice stacking arrangements.

Structure	Separation distance (Å)	TBC at room temperature ($MW/m^2 \cdot K$)	ZO/ZA gap at K point (THz)
ABC(B)	3.23	50.0	0
ABA(B)	3.23	46.6	0.24
ABA(N)	3.45	32.5	0.15
AAA	3.51	43.1	0.25
ABC(N,B)	3.45, 3.23	40.8	0.22

4.2.1 Phonon Dispersion Relations

Figure 4.3 shows the phonon dispersion of SLG, which is determined by diagonalizing the dynamical matrix of IFCs from the DFT calculations. Figure 4.3(a-e) compare the phonon dispersions of stretched and isolated SLG with the stretched SLG in the system of h-BN/SLG/h-BN with different stacking configurations. To decipher the different mechanisms that influence the phonon dispersion, the phonon dispersion relation of isolated SLG, un-stretched with equilibrium lattice constant (2.45Å) is plotted in Figure

4.3(a) for comparison. In Figure 4.3(a), the phonon dispersion relations show that stretching the isolated SLG will strongly soften the LO (Longitudinal optical) and TO (Transverse optical) modes for the entire $\Gamma - \mathrm{K}$ branch. In addition, there is a softening in LA (Longitudinal acoustic) mode compared with the un-stretched and isolated SLG. That is because stretching the SLG will increase the C-C bond length which will weaken the C-C bond and decrease the in-plane stretching force constant [197]. However, when the h-BN substrates is introduced, where SLG lattice is stretched to the h-BN lattice, the phonon dispersions reveal a further softening in LO and TO mode especially at the Γ point compared to the stretched isolated SLG. The additional "weakening" of the phonon vibrational modes LO and TO is initiated by the hybridization of graphene's out-of-plane π bond and h-BN's π bond. In graphene, the out-of-plane $2p_z$ orbitals are half-filled and the π band is half full, while in the h-BN, the $2p_z$ orbitals are either empty or full. The mixing of h-BN's $2p_z$ orbitals with those of graphene will change the occupation in the graphene's π states which results in further weakening of the C-C bond. A similar effect was observed in graphene on metal substrates, because the charge transfer happened from metal's *d* orbital to graphene's π states [197-199].

In Figure 4.3(a-e), a splitting between ZA and ZO modes can be observed at K point in most structures except ABC(B). The splitting is caused by breaking the equivalent of graphene's two carbon atoms in a unit cell [200]. For example, the structure ABA(B) introduces two bulks of h-BN on both sides of the graphene, with one carbon atom on top of the boron atom and the other carbon atom on the hollow of the h-BN ring. In other words, the carbon atom directly on top of the h-BN atoms will have a stronger interaction with h-BN than the other carbon atom. The AAA structure with the stacking of two carbon

atoms on either boron or nitrogen atoms has the largest ZA/ZO splitting at K point, because the repulsion and attraction from both sides of the interface by either nitrogen or boron atoms enhance the asymmetry of the two carbon atoms. However, the ABC(B) structure shows no ZA/ZO splitting at K point because of the centrosymmetric matching configuration on both sides of the graphene. The ZA/ZO splitting values for different configurations are shown in Table 4.1. Furthermore, Figure 4.3 shows a shift of the ZA mode at Γ point when graphene is sandwiched by h-BN. The shift of ZA mode at Γ point indicates the strength of the spring constant at the interfaces [194, 200].

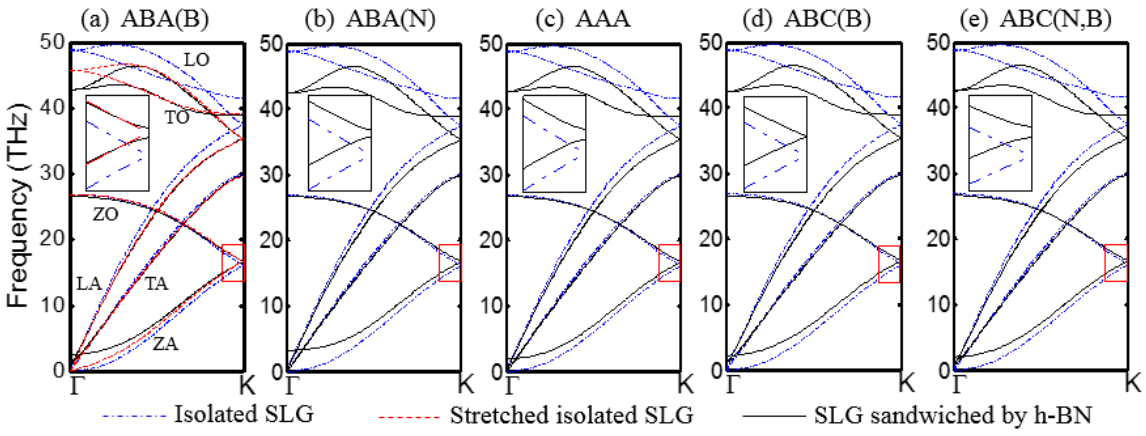

Figure 4.3 Phonon dispersions of (a) isolated SLG, stretched isolated SLG and SLG (stretched) in the ABA(B) sandwiched structure; (b-e) isolated SLG and SLG (stretched) in ABA(N), AAA, ABC(B), ABC(N,B) sandwiched structures, respectively. The splitting at K point between ZA and ZO modes are marked with red rectangles and also shown in inset as extended view.

4.2.2 Phonon Density of States (DOSs)

In order to investigate the effects of lattice stacking of h-BN/SLG/h-BN on phonon distribution, the phonon DOSs of the SLG sandwiched by h-BN in different stacking configurations are calculated. Figure 4.4 compares the DOSs of isolated SLG, stretched

isolated SLG, h-BN and SLG (stretched) sandwiched by h-BN in different stacking configurations. The results show that stretching the isolated SLG lower the cut-off frequency of DOSs. The sandwiched structure develops a new peak around 46 THz (highlighted by the blue arrow in Figure 4.4). It corresponds to the softening of the LO and TO modes at Γ point resulting from the interactions with the bulk h-BN substrates. The impact of lattice stacking on the DOSs of SLG is negligible as different stacking configurations results in almost identical DOSs. Compared with the un-stretched isolated SLG, the DOSs of sandwiched SLG is suppressed near zero frequency (< 2 THz) and then increases rapidly with a small overshoot near 3THz which is signature of shift of ZA mode near the Γ point. In addition, phonon spectrum mismatch between graphene and h-BN at high frequencies can be observed by comparing their DOSs. Results indicate that the DOSs mismatch between graphene and h-BN results in a small phonon transmission in the high frequency region (> 10 THz). More details will be discussed in Section 4.4.

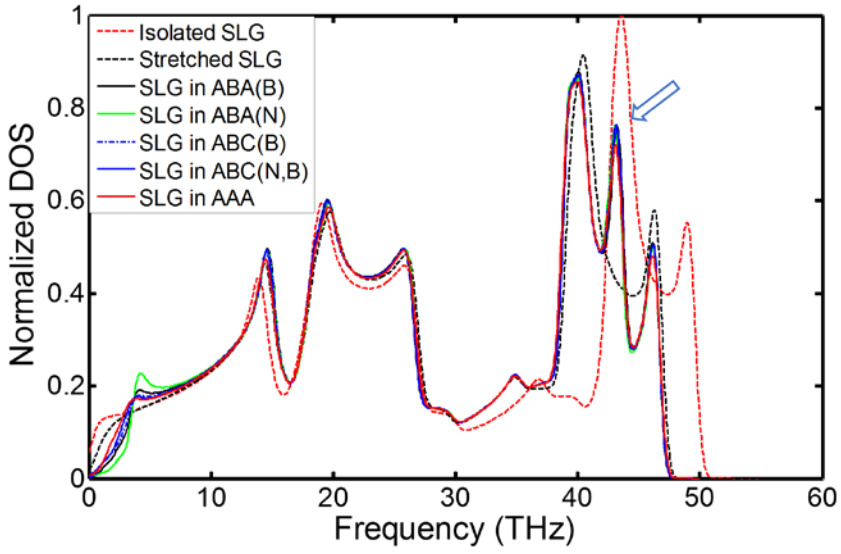

Figure 4.4 DOSs of isolated SLG, stretched isolated SLG, h-BN and SLG (stretched) sandwiched by h-BN with different stacking configurations.

4.3 Thermal Boundary Conductance of the Graphene/h-BN Interface

Following the Landauer formalism (Eq. 4-1), the temperature dependent and frequency dependent TBC of the five lattice stacking h-BN/SLG/h-BN configurations are obtained in Figure 4.5 and Figure 4.6. The results show that the TBC at room temperature is in the range of 32.5~50.0 MW/m^2·K depends on the stacking configurations in the order of ABC(B)>ABA(B)>AAA> ABC(N,B)>ABA(N) (Table 4.1). With the exception of the structure AAA (43.1 MW/m^2·K) (More details will be explained in section 4.4.), the order of the TBC's magnitude is consistent with the inverse order of interfacial separation distance: ABC(B)<ABA(B)<ABC(N,B)<ABA(N). The stacking configurations with C-B matched interfaces (boron atom on top of the carbon atom, such as in the ABC(B), and ABA(B)) have larger TBCs (50.0 and 46.6 MW/m^2·K) because of the smaller interfacial separation distances. The stacking configurations with C-B matched interfaces (ABC(B), ABA(B)) also have the lowest binding energy and the best structural stability. However, ABC(B) exhibits a virtually negligible electronic band gap in graphene because the centrosymmetric stacking is unable to break the equivalence of the two carbon atoms [86, 201]. Therefore, ABA(B)-stacked structure with TBC very close to ABC(B) can be considered to be the best configuration for the nano-electronic devices from the perspective of achieving good thermal and electric properties. Controlling the interfacial geometry can enhance the TBC and heat dissipation in nano-electronic devices.

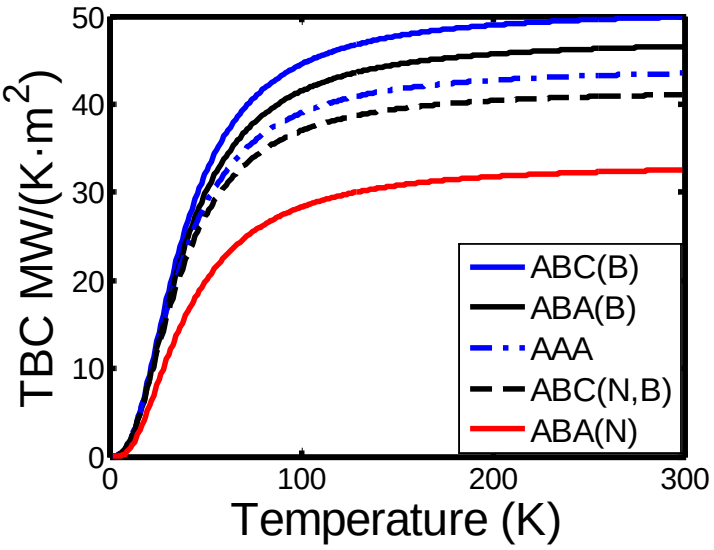

Figure 4.5 Temperature dependent thermal boundary conductance at h-BN/SLG/h-BN interfaces for different lattice stacking configurations.

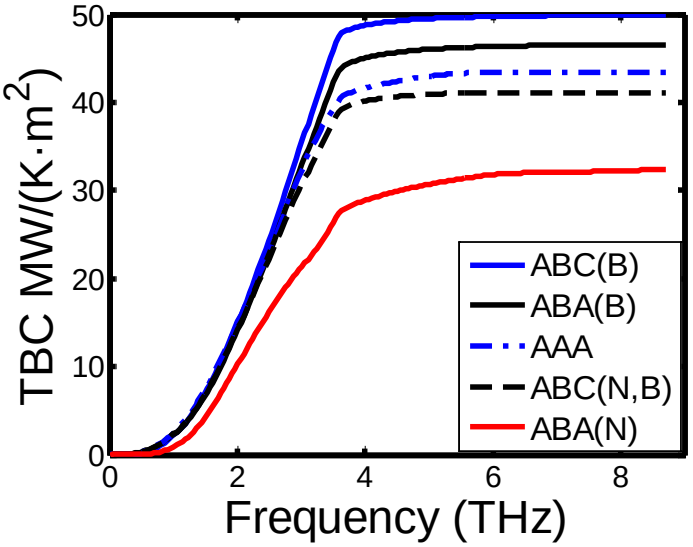

Figure 4.6 Frequency dependent thermal boundary conductance at h-BN/SLG/h-BN interfaces for different lattice stacking configurations at room temperature.

To understand the origin of the dependence of the TBC to the interfacial separation distance, the plane-averaged electron density difference Δn is calculated which will also

help in visualizing the electron redistribution upon the lattice stacking of the interfaces (Figure 4.7). The plane-averaged electron density difference Δn is defined as

$$\Delta n(z) = \Delta n_{\text{sandw}}(z) - \Delta n_{\text{BN}}(z) - \Delta n_{\text{SLG}}(z) \quad \textbf{(4-1)}$$

where $\Delta n_{\text{sandw}}(z)$, $\Delta n_{\text{BN}}(z)$, $\Delta n_{\text{SLG}}(z)$ indicate the plane-averaged densities of the sandwiched structure, h-BN layers and free-standing graphene, respectively. To keep consistent with the IFCs calculations, LDA is still used as the exchange-correlation functional. Although LDA tends to underestimate the interlayer binding energies and band gaps [85, 86], it is still a good approximation to predict structural parameters and the trend of electron density difference [186]. The details of the calculation can be found in Ref. [202]. Figure 4.7 shows that as interfacial separation distance decreases (from ABA(N) to ABA(B)), the magnitude of the plane-averaged electron density difference increase rapidly. This indicates that the electron wave functions of both graphene and h-BN have a stronger overlap at the interfacial gap as the separation distance decreases. This overlap was also observed by Xiong et al.'s [203], which is in agreement with our analysis of dispersion relations in the previous section.

The ABC(N,B)-stacked configuration is a combination of ABA(B) and ABA(N) arrangement, and reveals an intermediate TBC (40.8 MW/m^2·K). However, the AAA-stacked structure shows a larger TBC (43.1 MW/m^2·K) despite its largest interfacial separation distance even compared to the ABA(N). The phonon transport mechanism at interfaces will be discussed in detail in the next section. The results of this study (TBC 32.5~50.0 MW/m^2·K) are closer to the experimental measurement (3.7=0.5×7.4 MW/m^2·K[81]) compared to other studies (93= 0.5×186 MW/(m^2·K)[82]), but difference

is still large. One reason could be the quality of the samples in experiment. The corrugation and defects on the graphene samples, and the roughness and the contaminants at the interface may significantly decrease the TBC. Another reason could be the limitations and uncertainty in the Raman spectroscopy measurement in estimating heat flux across the interface[204]. In addition, the graphene and h-BN are not perfectly matched in the experiments. Different orientations of the two lattice in same sample and lattice mismatch [83] could lower the TBC [205]. While our simulation is based on five different lattice stacking configurations. Each of them correspond to a perfect interface made by stretching the graphene to fit the h-BN's lattice constant. The developed models and related analysis seek to decipher the mechanism of the phonon transport at the interface which is the focus of our study.

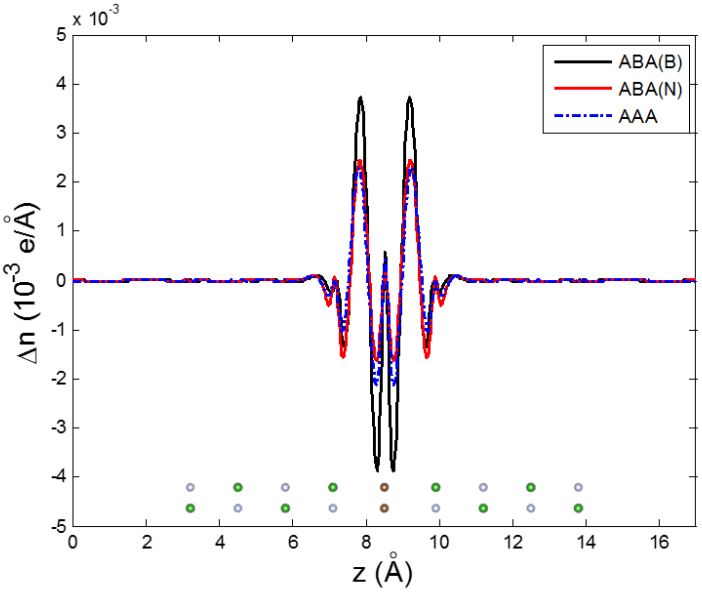

Figure 4.7 Plane-averaged electron density difference Δn (per unit cell) along out of plane direction showing the charge redistribution at the h-BN/graphene/h-BN interfaces. $-e$ is the charge of an electron. Here, Δn represents the difference in the plane-averaged electron density of the sandwiched structure from h-BN layers and free-standing graphene.

4.4 Phonon Transmission and Contributions to TBC

To explain the anomaly in the order of TBC with the interfacial separation distance, such as structure AAA, and to understand the mechanism of phonon transport at interface, the frequency dependent phonon transmission functions across h-BN/SLG/h-BN interfaces are calculated in all five configurations under consideration (Figure 4.8). Figure 4.8 clearly shows that the interfacial transmission is dominated by low-frequency (< 5THz) phonons. This study finds that the DOSs mismatch between graphene and h-BN results in a small phonon transmission in the high frequency region. The transmission peak in the high frequency region is located around 10THz, 20THz and 40THz, which is consistent with the positions of the peaks of phonon DOSs in h-BN but the transmission is low as peaks in DOSs of graphene are not co-located and these high frequency phonons may not efficiently couple. Since the high frequency make little contribution to the TBC, this study focuses more on the phonon transmission under 10THz, which make the dominant contribution to the TBC. In the low frequency region, two transmission peaks and one valley are observed for each structure. The valley between the two peaks is around 2.5 THz for structures ABA(B), AAA, ABC(B), ABC(N,B). However, for the structure ABA(N), there exists a broader valley around 2.5~3.1 THz, and the high frequency peak (the blue solid arrow in Figure 4.8) is much narrower than the low frequency peak. In contrast, structure ABA(B) has a much wider high frequency peak, indicated by the black solid arrow. In order to explain this, we also compute the phonon transmission function in the first Brillouin zone of the unit cell (Figure 4.9). In Figure 4.9, we present the phonon transmission along the Γ-K direction in k space for different frequencies and analyze the relative transmission of phonon modes across the interfaces. The color changes from dark blue to red show the

increase of the phonon transmission strength. Different phonon modes of graphene (Figure 4.9(a-e)) and the whole system (Figure 4.9(f-j)) are shown on top of the transmission contours. The graphene's phonon modes in Figure 4.9(a-e) were calculated by solving the 6×6 dynamic matrix which is a part of the system's 54×54 dynamic matrix, and belongs to the two carbon atoms in the system. Black dots in Figure 4.9(f-j) show the phonon modes of the sandwiched structure by solving the entire dynamic matrix of the system.

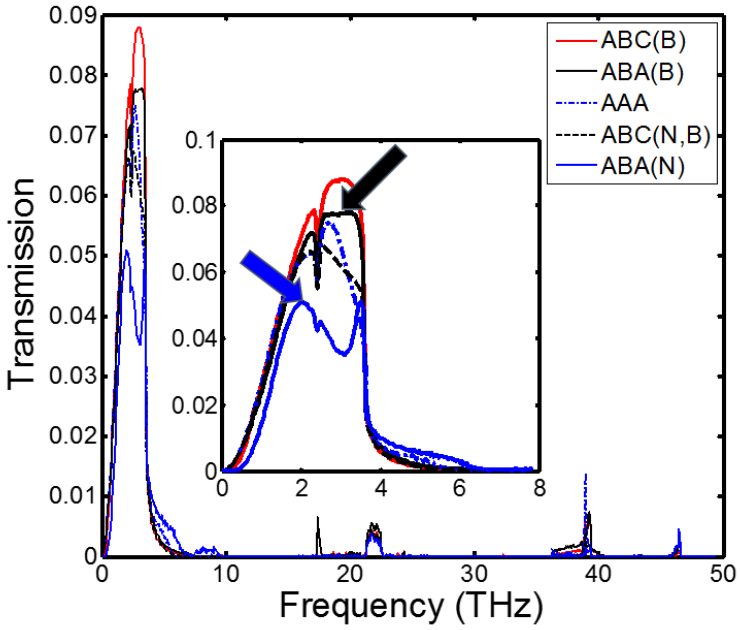

Figure 4.8 Angular frequency dependent phonon transmission for different lattice stacking configurations. Inset shows phonon transmission for frequency in the range of 0-8 THz. Blue arrow shows peak in transmission for ABA(N) for modes where contribution of N atoms is higher and black arrow shows peak in transmission for ABA(B) for modes where contribution of B atoms is higher.

For configurations with low interfacial separation distance (C-B matched interfaces, Figure 4.9(a, d) and Table 4.1), the in-plane acoustic modes (the LA, TA modes) have the dominant contributions to the transmission. As the interfacial gap increases

(Figure 4.9(b)), the in-plane acoustic modes' contribution decreases leading to higher contributions by out-of-plane acoustic modes (~ZA modes). This could be further understood by the frequency dependent TBC from Figure 4.6 and wave-vector dependent transmission from Figure 4.9. Compared to the ABA(B) configuration in Figure 4.6, the slope of the ABA(N)'s TBC ~ frequency curve decreases sharply after 2 THz. This is because of very low transmission between 2-3 THz for ABA(N) compared to ABA(B) as shown in Figure 4.9 (a) and (b). In addition, TBC difference between AAA and ABA(B) increases after 2 THz (Figure 4.6) resulting from the weakening of the contribution to transmission from LA and TA modes shown in Figure 4.9(c). However, the configuration AAA with a 3.50 Å interfacial gap have better transmission and larger TBC than the ABA(N) with a 3.45 Å interfacial gap. Despite of the higher interfacial separation distance, the TBC is higher because of the better phonon coupling between graphene and h-BN in structure AAA than that in the ABA(N).We found that the interfaces with C atoms directly on top of B atoms has stronger phonon-phonon coupling between graphene and h-BN than that with C atom directly on top of N atom. One explanation for this is that the mass of the B atom is much closer to the C atom than the N atom. The mass difference of B and C is 37.5% smaller than that of N and C, which leads to closer vibration frequency for energy transfer. An additional explanation for this observation is that the short-range Pauli's repulsive forces acting on the C-N matched layer is larger than that of C-B matched layer due to differences in the effective atomic volume of N and B and the difference in the local electron density around the N and B, which increases the separation distance and obstruct the phonon transmission. Therefore, the C-B matching in the AAA configuration in addition to C-N matching leads to higher transmission and TBC compared to the C-N

matched structure ABA(N). Furthermore, by considering the eigenvectors of the sandwiched system's dynamic matrix, we find that the phonon modes with higher frequency involve more B atoms for the same wave vector, while the N atoms make more contributions to the lower frequency phonon modes. Similar observation for contribution of B and N atoms to phonon modes were made by Slotman et al.'s [91]. This further explains the characteristics of transmission peaks in Figure 4.8. For the stacking arrangements ABA(B) and ABC(B), the transmission peak in the high frequency region is high and wide (black arrow in Figure 4.8) because of the C-B matched interfaces, corresponding to stronger phonon coupling. For the configuration ABA(N), the transmission peak in the low frequency region is much stronger than the peak in the high frequency region (blue arrow in Figure 4.8) resulting from the C-N matched interfaces.

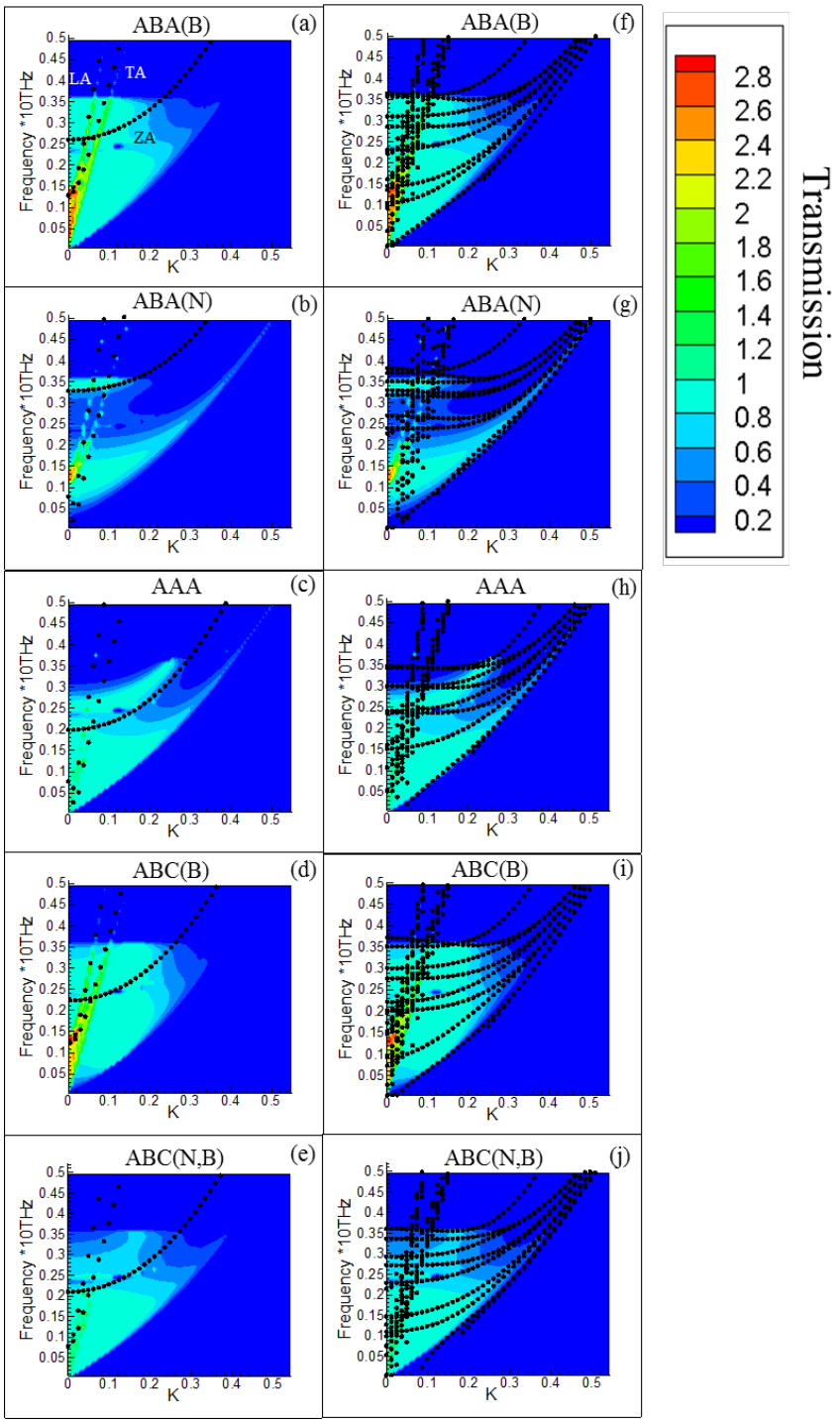

Figure 4.9 Frequency and wave vector dependent phonon transmission along $\Gamma - K$ direction for different stacking configurations. Black dashed lines in (a-e) show phonon dispersion (<5 THz) of SLG in the sandwiched structures along $\Gamma - K$ direction. Black dashed lines in (f-j) shown phonon dispersion (<5 THz) of entire sandwiched structure along $\Gamma - K$ direction.

4.4 Closure

In summary, this chapter have developed an atomistic framework based on DFT and atomistic Green's function to investigate the impact of different lattice stacking configurations on the thermal transport across the h-BN/graphene/h-BN interfaces. The h-BN substrates soften the TO and LO modes of graphene because of the overlap of orbitals. It introduces an asymmetry between carbon atoms in graphene's unit cell leading to gap of different magnitude between the TA and ZA modes of graphene at K point in different stacking configurations. Results indicate that the in-plane acoustic modes have the dominant contributions to the TBC for the C-B matched interfaces because of the low interfacial gap, but their contribution reduces as the interfacial separation distance increases. The frequency and wave vector dependent transmission reveal very low transmission between 2-3 THz for ABA(N) configurations with C-N matched interface leading to sharp drop in TBC compared to other structures which has C-B matched interfaces. The TBC can be enhanced by more than 50% by changing the lattice stacking arrangements from C-N matched to C-B matched interface. The TBC (32.5~50.0 MW/(m^2·K)) of this study is closer to the experimental measurement compared to the previous studies. The findings in this study will provide insights to better understand the experimental measurements on TBC and the mechanism of phonon transport at h-BN/graphene/h-BN interfaces.

CHAPTER 5 : THE ROLE OF INTERFACIAL ELECTRONIC PROPERTIES ON PHONON TRANSPORT IN TWO-DIMENSIONAL MOS_2 ON METAL SUBSTRATES

In this chapter, the first-principles density functional theory (DFT) and the atomistic Green's function (AGF) method are performed to elucidate the physical nature of the inherent connection between electronic structure and phonon properties at the interface of single-layer MoS_2 and its metal substrates. We compare phonon transport at Au and Sc contacts with MoS_2 to investigate the differences in the interfacial spacing and electronic structure, which results in two types of interfaces: physisorption and chemisorption. To further illustrate how the electronic structure affects the phonon distribution and thermal transport across the interface, we investigate the effects of the lattice-stacking configurations of MoS_2/Sc on electronic and phononic properties. We examine the transport for three typical lattice-stacking at MoS_2/Sc interfaces. This study will help understanding the inherent connection among the interfacial electronic structure, the phonon distribution, and TBC, which will provide insights into the future design of MoS_2-based electronics and methods of enhancing heat dissipation at the interfaces of MoS_2-based electronic devices.

5.1 Structure Optimization and IFCs Calculation of the $MoSe_2$/Metals Interfaces

The monolayer MoS_2 and its sandwiched structure with metals (Au, Sc) are optimized by the Vienna ab initio simulation package (VASP). A plane-wave basis set and the projector augmented-wave (PAW) method are used with the local density approximation (LDA) exchange–correlation functional [188, 189]. A precise description

of the interface properties of metal substrates and MoS_2 might require an inclusion of the long-range dispersion interaction (vdW). However, a proper treatment of vdW into the framework of DFT is not a trivial task, despite it being actively investigated by the DFT community for the past decade[206, 207]. In fact, there is no universal DFT functional with a rigorous vdW correction that works for all types of systems. It is generally accepted in the community that generalized gradient approximation (GGA) to the exchange-correlation functional (without adding any vdW corrections) significantly underestimates vdW interactions, while LDA overestimates them or sometimes closely reproduces optimized structures of high-level functional calculations. Specifically, LDA is suitable for calculating interfacial TBC that is highly sensitive to the interlayer structure property.[94, 98, 208] The lattice constants of the single-layer MoS_2 are obtained via structural optimization with the value of 3.12 Å, which is in good agreement with the experimental results from the previous studies [209, 210]. In this study, the in-plane lattice constant of single-layer MoS_2 is used as the surface lattice constant in the sandwiched systems. The 2×2 unit cell of Au (111) substrate can match the $\sqrt{3}\times\sqrt{3}$ unit cell of MoS_2 with an ~3.9% lattice mismatch, whereas the 1×1 unit cell of Sc (0001) has the lattice mismatch below 3.2% with the 1×1 unit cell of MoS_2 as illustrated in Figure 5.1 a-d. The most stable contact geometries are obtained by optimizing the structures from various lattice-stacking configurations (Table 5.1). In the MoS_2/Au(111) system, the three Mo atoms in the unit cell sit above the fcc hollow, hcp hollow, and top sites, respectively, while the three pairs of S atoms are located at the triangle center formed by the fcc, hcp, and top sites. In the MoS_2/Sc(001) system, Mo atom is on top of the first layer Sc atom and the pair of S atoms are on top of the second layer Sc atom. The interfacial distances of the Au/MoS_2/Au and

Sc/MoS_2/Sc systems are optimized for the unit cell system with a sampling of 17×17×1 k-point grids and 25×25×1 k-point grids, respectively. Using this optimized equilibrium spacing (2.82Å for MoS_2/Au interface and 1.86Å for MoS_2/Sc interface), a 3×3 supercell of single layer MoS_2 sandwiched by 4 layers of Au bulks and a 5×5 supercell of MoS_2 sandwiched by 4 layers of Sc bulks are assembled for the calculations of second order interatomic force constants (IFCs) (Figure 5.2 a,b). These supercells contain 369 atoms for Au/MoS_2/Au system and 275 atoms for the Sc/MoS_2/Sc system with the vacuum region of 16.5 Å. 3×3×1 k-point grids are applied to sample the Brillouin zone of these supercells. For the supercell system, the kinetic energy cutoff is set to 400 eV. To calculate the IFCs, the displacement length of each atom from its equilibrium position is 0.01 Å.

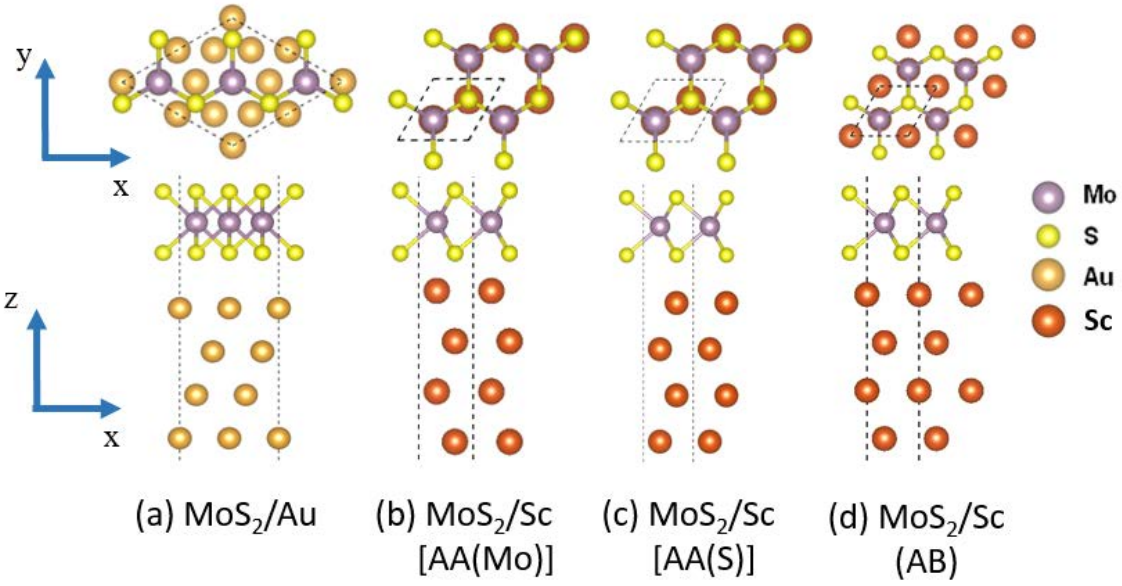

Figure 5.1 (a) Top and side views of the unit cell of monolayer MoS_2 on the substrate of Au. (b-d) Top and side views of the unit cell of MoS_2/Sc structures with different lattice stacking configurations. (b) For structure AA(Mo), Mo in the parentheses presents that the molybdenum atom is on top of the first-layer Sc atom. (c) For structure AA(S), S in the parentheses presents that the pair of sulfur atoms are on top of the first-layer Sc atom. (d) For structure AB, Mo is on top of the second layer Sc atom while the first layer Sc atom is centered under the MoS_2 hexagonal ring.

With the second order IFCs directly obtained from the DFT calculations, harmonic matrices are constructed which provide a reliable prediction of the interatomic interactions for the AGF calculations[211, 212]. The phonon transmission function and TBC at the metal/ MoS_2/metal interfaces can be obtained by AGF calculations[98, 149, 174, 177], where single-layer MoS_2 ("device") is sandwiched between two "contacts" corresponding to the hot and cold thermal reservoirs represented by semi-infinite metal bulks (Figure 5.2 a, b).

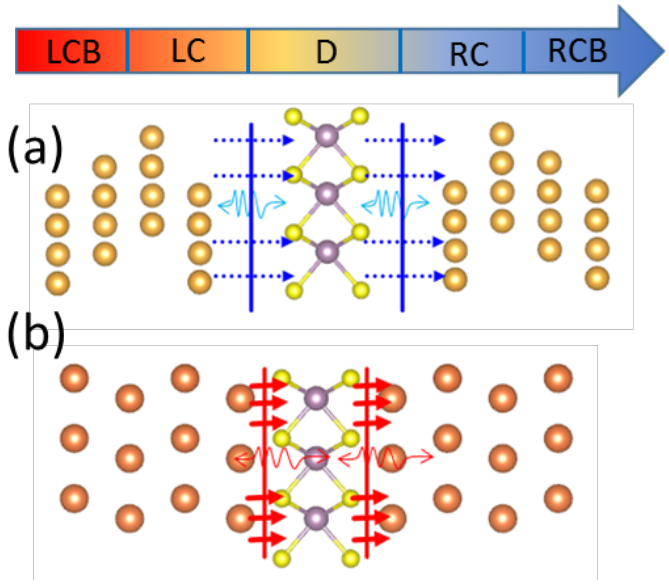

Figure 5.2 (a-b) Schematic of (a) physisorbed interface of Au/MoS_2/Au, (b) chemisorbed interface of Sc/MoS_2/Sc for the AGF calculations. The interface regions of Sc/MoS_2/Sc and Au/MoS_2/Au are marked as red and blue. The system is divided into a "device" region (D), left contact (LC) and right contact (RC) and two semi-infinite metal bulks, left contact bulk (LCB) and right contact bulk (RCB) which do not interact with the "device" region. The "device" region only includes the monolayer MoS_2.

5.2 Chemisorption or Physisorption ?

The LDA optimized distances between MoS_2 and the metal substrates are 2.82Å for Au and 1.86Å for Sc (for details see Table 5.1). The significant difference of the

interfacial spacing is a good measure of identifying the nature of their interactions; Sc forms a strong bonding with MoS_2 (chemisorption type interaction), while MoS_2 bounds to Au by weak wave function overlaps (physisorption type interaction).

Table 5.1 Structure optimization and thermal properties of MoS_2/metal interface

Structure		Interfacial distance (Å)	Sc-S distance at the interface (Å)	TBC at room temperature ($MW/m^2 \cdot K$)	Binding energy per S at the interface(eV/atom)
MoS_2/Sc	AA(Mo)	1.86	2.58	282	-1.38
	AA(S)	2.58	2.58	172	-0.82
	AB	2.16	2.81	107	-0.82
MoS_2/Au		2.82	--	14.3	-0.20

Figure 5.3 a-d presents the partial density of states (PDOS) that reveal their interaction mechanism. For an isolated MoS_2, its conduction band minimum (CBM) is characterized by the d_{z^2} orbitals of weakly interacting cations in *xy*-plane, while the valence band maximum (VBM) is contributed by both d_{xy} and $d_{x^2-y^2}$ orbitals[213]. The CBM and VBM characters are identified in the atomic orbital decomposed PDOS in Figure 5.3(a), where d_{xy} + $d_{x^2-y^2}$ states (solid green line) are located at VBM, right below Fermi level (E_F) and d_{z^2} states (solid red line) are the frontier states above the Fermi level. The changes of those frontier states upon the interaction with the metal substrates are monitored in Figure 5.3(b-d). Interaction with the metal substrates overall shifts down MoS_2 states from the isolated states, which indicates charge transfer from the substrates to MoS_2. However, the degree of orbital hybridization between them shows significant differences.

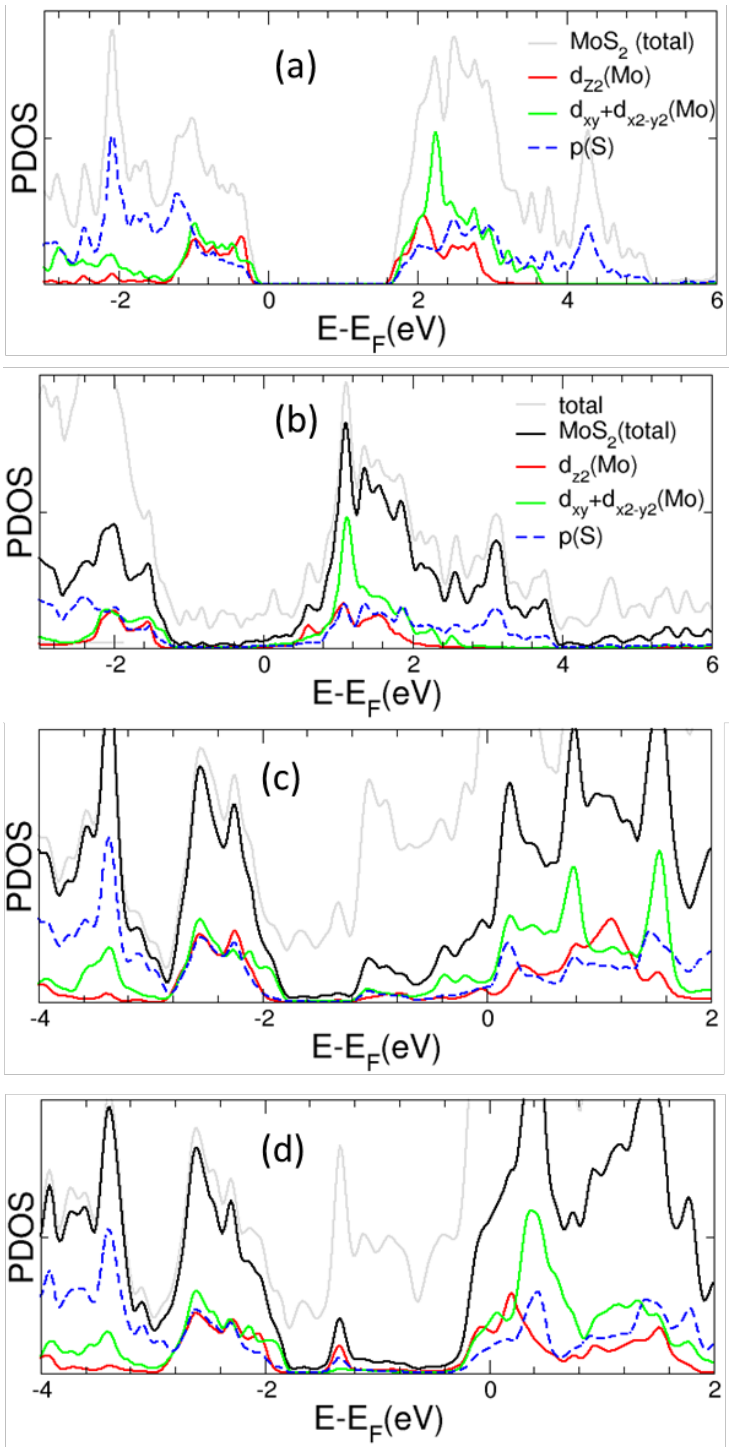

Figure 5.3 (a-d) Electron PDOS of (a) isolated monolayer MoS_2, (b) MoS_2/Au, (c) MoS_2/Sc (structure AA(Mo)), (d) MoS_2/Sc (structure AB).

For the case of MoS_2/Au system, the dispersion of frontier states below the Fermi level involves the hybridization of Au surface states and *s* and p_z orbitals of sulfur, yet the amount of occupation is small (see Figure 5.3(b)). This indicates that the weak attractive binding is originated from the weak overlap between the S and Au orbitals and charge transfer to S. On the other hand, for MoS_2 on the Sc substrates, a significant portion of the previous conduction band states become occupied below Fermi level (see Figure 5.3(c-d)), indicating a strong charge transfer from Sc to MoS_2.

Figure 5.4 shows the electron localization function (ELF) contours of the unit cell of MoS_2/Au and MoS_2/Sc. The ELF provides a description of chemical bonds by the probability of finding another same-spin electron in the neighborhood of a reference electron.[214, 215] At the MoS_2/Au interface, electron localization is hardly observed, which means the Au substrate do not have much influence on the electron distribution of the MoS_2 and its interface. It can be called the physisorbed interface. However, the strong interaction is indicated in Figure 5.4(b) at the interface of MoS_2 and Sc. A strong ELF overlap can be observed at the MoS_2/Sc interface between the S and Sc atoms. Furthermore, the region of high ELF around S is not spherically symmetric and exhibits lobes directed toward the Mo and Sc atoms, which makes the bonding between Mo-S and S-Sc a mixture of ionic and covalent bonds[216]. It can be called the chemisorbed interface. To better understand the impact of the metal substrates on the electron redistribution of the interface, the plane-averaged electron density difference Δn was calculated in Figure 5.5. The plane-averaged electron density difference Δn is defined as

$$\Delta n(z) = \Delta n_{\text{Sandw}}(z) - \Delta n_{\text{MoS}_2}(z) - \Delta n_{\text{Metal}}(z) \quad (2)$$

where $\Delta n_{\text{Sandw}}(z)$, $\Delta n_{\text{MoS}_2}(z)$ and $\Delta n_{\text{Metal}}(z)$ indicate the plane-averaged densities of the sandwiched structure, free-standing single layer MoS_2, and metals, respectively. The large wavy peak between the S and Sc atoms in the red region of Figure 5.5 indicates that the absolute magnitude of the plane-averaged electron density difference is dramatically higher at the MoS_2/Sc interface than that at the MoS_2/Au interface. It can also be explained by the stronger electron wave function overlap of both MoS_2 and Sc, resulting from the smaller interfacial separation distance.

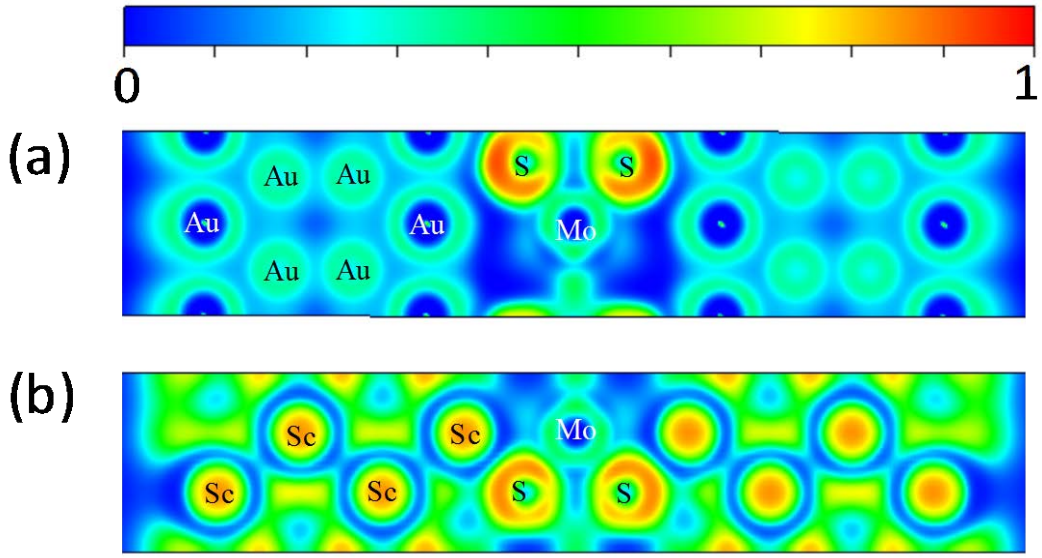

Figure 5.4 (a-b) Electron localization function (ELF) for the unit cell of (a) MoS_2/Au, (b) MoS_2/Sc.

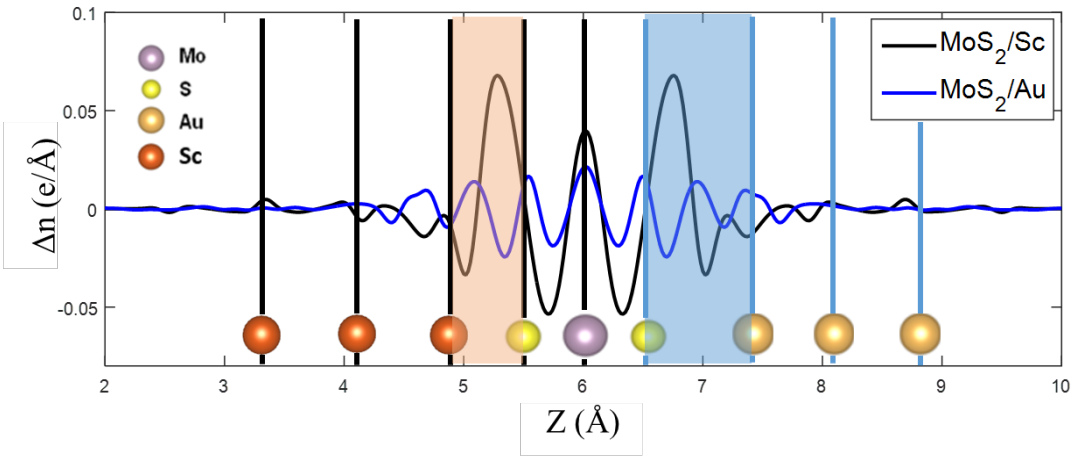

Figure 5.5 Plane-averaged electron density difference Δn (per unit cell) along out-of-plane direction showing the charge redistribution at the metal/MoS_2/metal structures. Δn represents the difference in the plane-averaged electron density of the sandwiched structure from metal substrates and free-standing monolayer MoS_2. For comparison, the left part shows only the location of Sc atoms in left half structure of Sc/MoS_2/Sc while the right part shows the location of Au atoms in right half structure of Au/MoS_2/Au.

5.3 Impact of the Interfacial Electron Structure on Phonon Properties

In order to investigate the impact of the interfacial electron structure on the thermal transport of different interfaces, the phonon transmission at the interfaces is calculated using the AGF method (Figure 5.6). The TBCs shown in Figure 5.7 are calculated by the Landauer formula using the transmission function obtained from AGF calculations. Results show that phonon transmission across the MoS_2/Sc interface is much greater than that of the MoS_2/Au interface (Figure 5.6). In addition, Figure 5.7 shows that the TBC of MoS_2/Sc is 19 times larger than that of MoS_2/Au because of the strong bonding strength at the MoS_2/Sc interface with chemisorbed interactions.

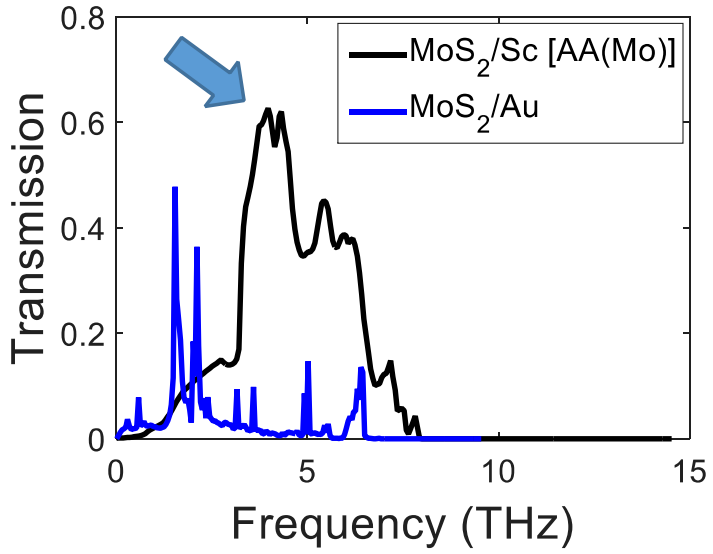

Figure 5.6 Angular frequency dependent phonon transmission for single layer MoS_2 with Au and Sc substrates.

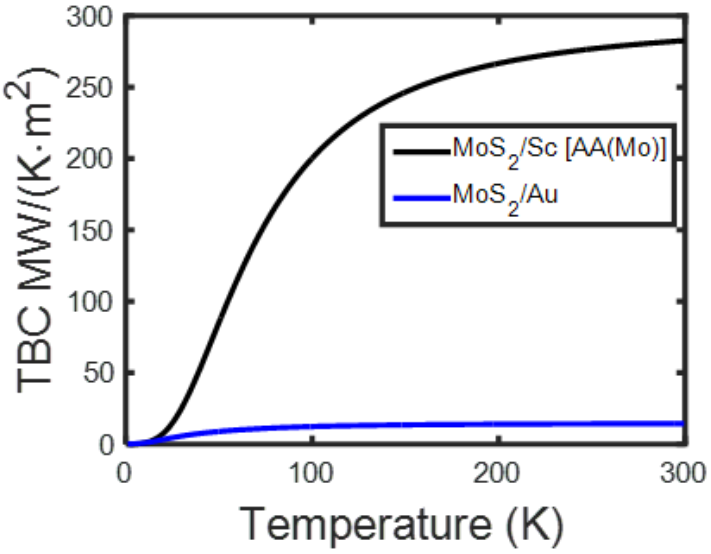

Figure 5.7 Temperature dependent thermal boundary conductance at interfaces of single layer MoS_2 and metal substrates.

To understand the mechanism of the thermal transport of these two different types of interfaces, the phonon DOSs of MoS_2 and its metal substrates is calculated using IFCs obtained from the DFT calculations[98, 217] in Figure 5.8(a-c). Figure 5.8(a) compares the

phonon DOSs of isolated monolayer MoS_2, monolayer MoS_2 with Au substrates and monolayer MoS_2 with Sc substrates. Results indicate that the strong interaction between metal and MoS_2 leads to significant redistribution in the phonon DOSs of MoS_2. After the introduction of the Au substrate, the phonon distribution of MoS_2 does not change much compared with isolated monolayer MoS_2 (Figure 5.8(a)). On the other hand, the phonon DOSs of MoS_2 in MoS_2/Sc structure shift to the lower frequencies under the influence of the Sc substrate. It can be explained by the charge transfer among the Mo, S and Sc atoms, which weakens the Mo-S bond. More details about the impact of charge transfer on the phonon distribution and the force constant will be discussed later. The DOSs shift of MoS_2 in MoS_2/Sc leads to a better match with the DOSs of the Sc bulk, which enhances phonon-phonon coupling and results in a huge transmission peak in Figure 5.8 around 4THz.

Furthermore, by comparing Figure 5.8(b) and Figure 5.8(c), the significant phonon DOSs mismatch occurs between MoS_2 and Au, which results in low phonon transmission and TBC. In addition, the strong chemisorbed interaction at the MoS_2/Sc interface not only influences the phonon distribution of MoS_2 but also changes the phonon distribution of first-layer Sc atoms. On the other hand, because of the weak physisorbed interaction at the MoS_2/Au interface, the shape of phonon DOSs of first-layer Au atoms near the interface remains similar to that of the Au bulk. These results also explain the different influence on the interface electronic structure and phonon properties caused by the two different type of interfaces.

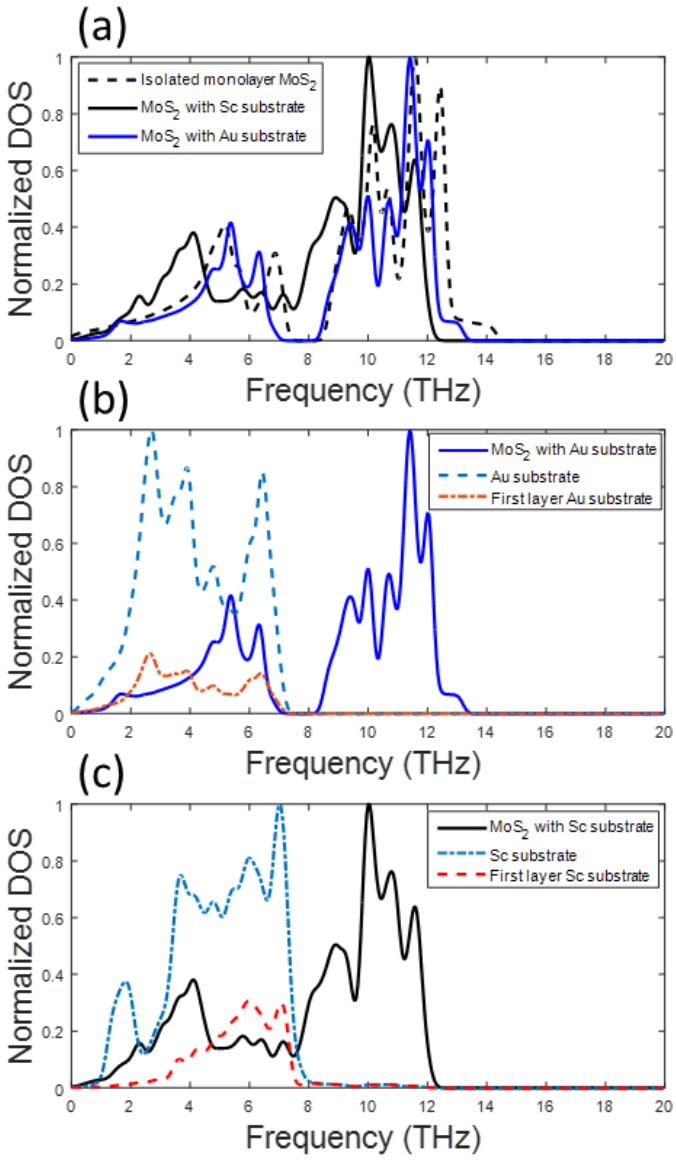

Figure 5.8 (a) Phonon density of states (DOSs) of isolated monolayer MoS_2, and monolayer MoS_2 with different metal substrates. (b) Phonon DOSs of monolayer MoS_2 with Au substrate, Au substrate, and the first layer of Au substrate. (c) Phonon DOSs of monolayer MoS_2 with Sc substrate, Sc substrate, and first-layer of Sc substrate.

5.4 MoS_2/Sc Interface with Different Lattice-Stacking Configurations

To further illustrate how interface electronic structure affects the phonon distribution and phonon transport across the interface, the effects of lattice-stacking

configurations of MoS_2/Sc on electronic and phononic properties are investigated. Because of the strong chemisorbed interaction across the MoS_2/Sc interface, thermal transport becomes more sensitive to the change of the electron structure.

Three typical lattice-stacking MoS_2/Sc interfaces are examined. Figure 5.1(b-d) show the top and side views, in the x-y plane and x-z plane, of various lattice-stacking configurations of MoS_2/Sc structures. We distinguish them as AA(Mo), AA(S), and AB. For structure AA(Mo), which has the most stable structure and lowest binding energy (Table 5.1), Mo in the parentheses presents that the molybdenum atom is on top of the first layer scandium atom. The pair of S atoms is on top of the second layer scandium atom. The MoS_2/Sc structure used in Figure 5.2(b) is AA(Mo). For structure AA(S), S in the parentheses presents that the pair of sulfur atoms are on top of the first layer scandium atom. The molybdenum atom is on top of the second layer scandium atom. For structure AB, Mo is on top of the second layer scandium atom while the first layer scandium atom is centered under the MoS_2 hexagonal ring. Structural optimization is conducted by DFT calculation and results are shown in Table 5.1. The results show that the TBC at room temperature is in the range of 107~282 $MW/m^2 \cdot K$ depending on the stacking configurations in the order of AA(Mo)>AA(S)>AB (Figure 5.9).

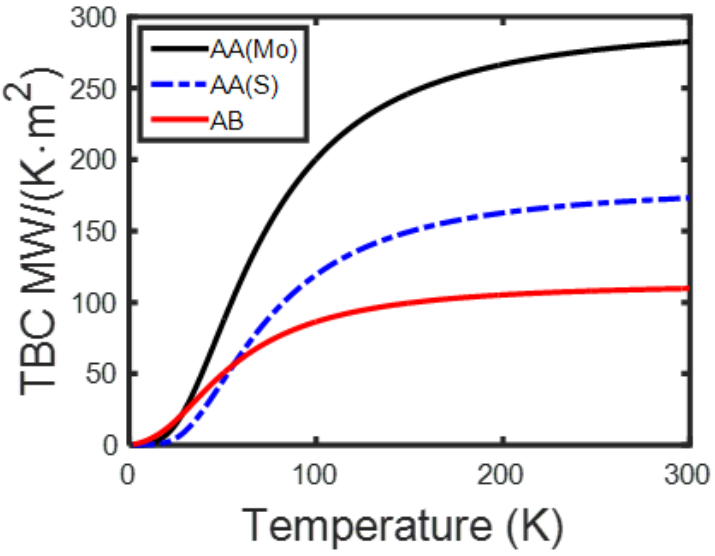

Figure 5.9 Temperature dependent thermal boundary conductance at the interface of MoS_2/Sc for different lattice stacking configurations.

It is clear that structure AA(Mo) has the highest TBC because of its shortest interfacial distance and the best structural stability. However, structure AB has a lower interfacial distance but a lower TBC compared with the structure AA(S). One reason could be the Sc-S distance at the interface of structure AB is larger than that of AA(S). The strong bonding between Sc and S atoms makes the Sc-S distance more important than the actual interfacial gap. However, it can't explain the significant difference of the shape of the phonon transmission curve in AB compared with the AA(Mo) and AA(S) structures (Figure 5.10). To explain this, the phonon DOSs of MoS_2 in various lattice-stacking structures are calculated shown in Figure 5.11. The phonon distribution of MoS_2 in AB reveal a significant difference compared with other structures. For structure AB, there are two large DOSs peak at the low-frequency range under 3THz and almost no DOSs are between the 3 and 6THz, which leads to a large peak in phonon transmission marked by

the red arrow in Figure 5.10 and the low transmission right after the peak. The difference in phonon DOSs and transmission will be further explained in the next section.

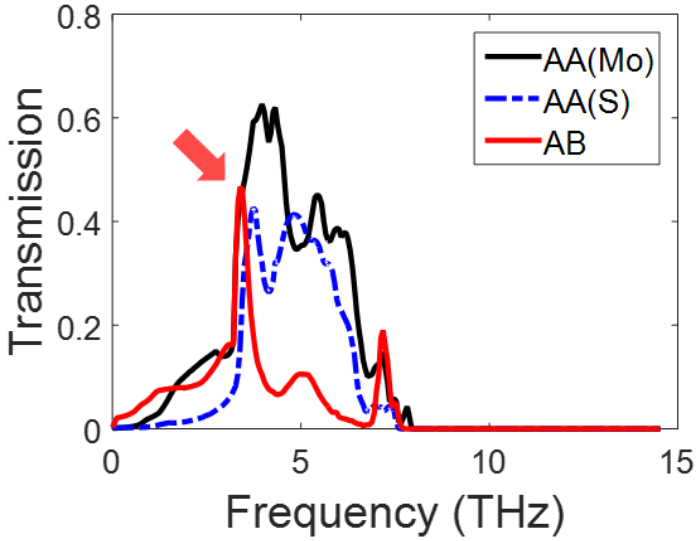

Figure 5.10 Angular frequency dependent phonon transmission at the interface of MoS_2/Sc for different lattice stacking configurations.

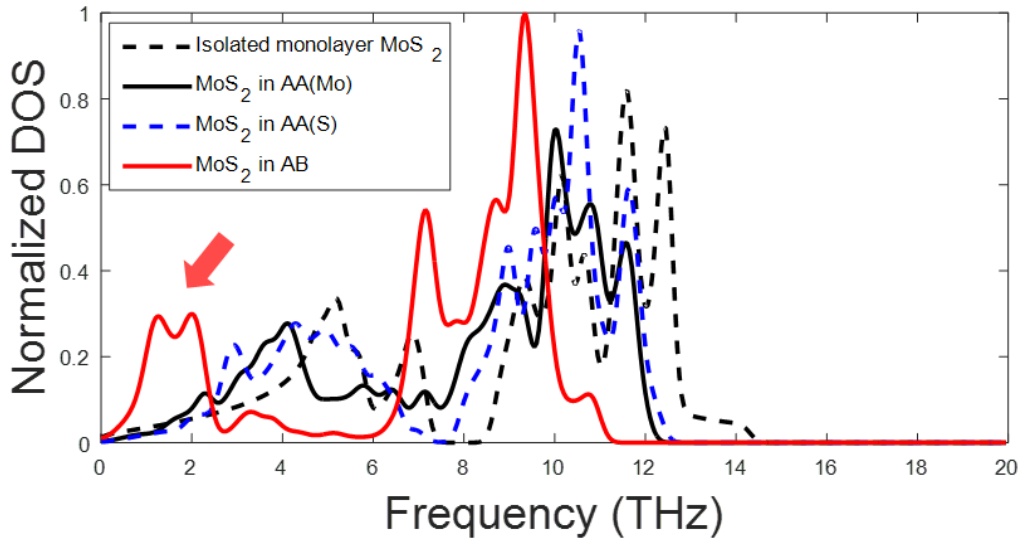

Figure 5.11 Phonon DOSs of isolated monolayer MoS_2, the MoS_2 sandwiched by Sc substrate with different stacking configurations, and the Sc substrate. The red arrow in this figure indicates the phonon redistribution of MoS_2 in AB, which results in the phonon transmission peak in Figure 5.10 marked by another red arrow.

5.5 Inherent Connection among Interfacial Electronic Properties, Phonon Transmission, and TBC

To further illustrate the changes in phonon DOSs and transmission, the effects of interfacial lattice-stacking configurations of MoS_2/Sc on their properties are considered. Specifically, we consider two types of stackings, AA and AB, of MoS_2 on Sc. The structure AA(Mo) is used here as a representative of the AA structure. For the AA(Mo) structure, Mo *d* orbitals form slightly hybridized states with S *p* orbitals, which is shifted down ~1.0eV below Fermi level, indicating charge transfer from Sc to the Mo *d* and S *p* hybridized states (see Figure 5.3(c)). PDOS in Figure 5.3(d) reveals that the AB stacking involves a stronger hybridization between Mo *d* and S *p* orbitals, which results in a high intensity in PDOS within ~0.3eV below the Fermi level. A defect like state located ~1.3eV below E_F is the hybridized state of S *p* and Mo dz^2 orbitals, where extra charges are transferred.

In order to confirm the understanding from the PDOS, we further visualize changes of charge density upon the adsorption of MoS_2 on Sc. Figure 5.12(a-b) shows the charge difference between the MoS_2/Sc system and the sum of isolated MoS_2 and Sc substrate with the lattice stacking of AA(Mo) and AB. The yellow regions represent the accumulation of electrons and the blue regions represent the depletion of electrons in the MoS_2/Sc system. In both structures, there exist the electron depletion region between the Mo and S atom, electron accumulation region around the Mo atom and the region between S and Sc interface. It indicates that the charge transfer has two routines after introducing the Sc substrate. One is from Sc atoms to Mo and S atoms. The other is from the bonded region of Mo-S to Mo atom. Both of the routines will weaken the Mo-S bond[94, 208]

which results in the phonon redistribution of MoS_2 in Figure 5.11. The intrinsic nature behind the charge transfer and phonon redistribution is the change of the force constant among atoms. More electrons transfer to S-Sc interface in structure AA(Mo) than that in structure AB, which enhances the strength of the bonding between S and Sc. Therefore, the interactions between S and Sc become stronger and lead to a significant increase of the

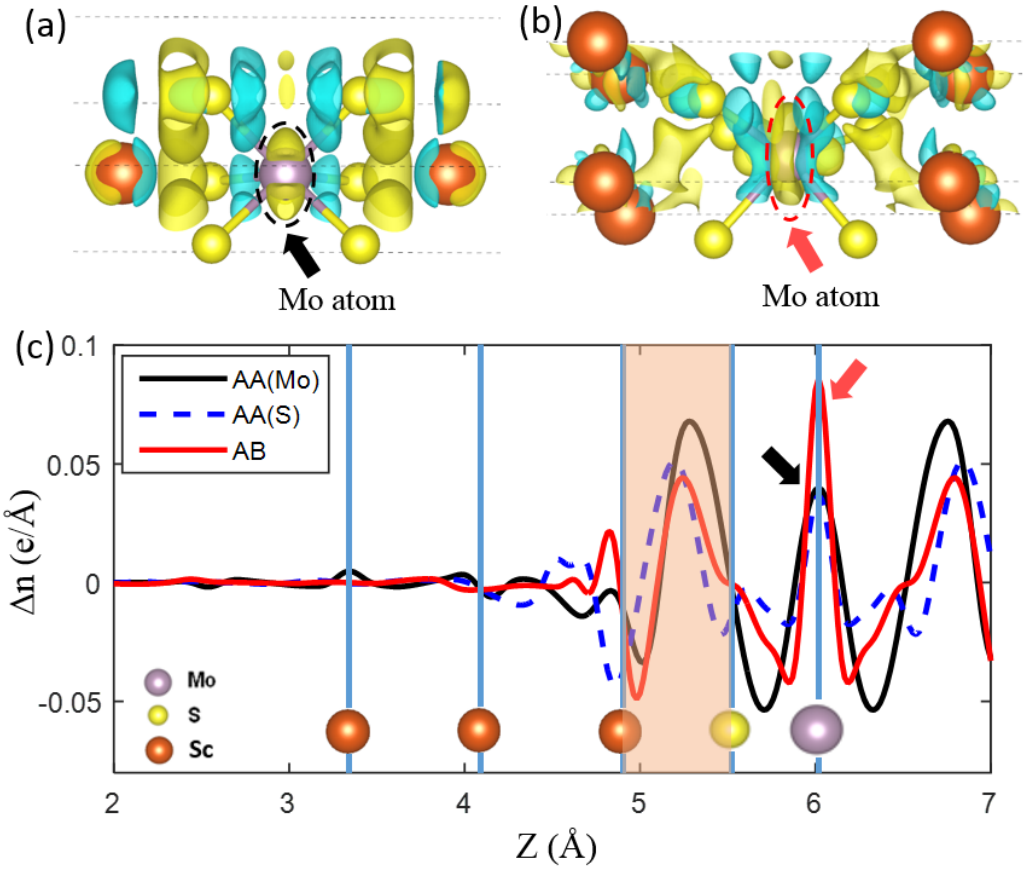

Figure 5.12 (a-b) Side view of the charge difference between the MoS_2/Sc system and the sum of the isolated MoS_2 and Sc substrate with different stacking configurations, (a) structure AA(Mo), (b) structure AB. The yellow regions represent the accumulation of electrons and the blue regions represent the depletion of electrons in the MoS_2/Sc system. Dashed red ellipse in (b) indicates high accumulation of electrons at Mo for structure AB (c) Plane-averaged electron density difference Δn (per unit cell) along out of plane direction showing the charge redistribution at the Sc/MoS_2/Sc structures with different stacking configurations. The interface of MoS_2/Sc is marked as the shaded region. The

peaks pointed by the red and black arrows at 6 Å indicate the charge accumulation around Mo atom which are also marked with dashed ellipse in (a) and (b).

phonon transmission and TBC. On the contrary, the electron transfer to Mo atom in structure AB is larger than that in AA(Mo), which further weakens the strength of the Mo-S bond. The physical connection behind this is the resultant decrease of the force constant between Mo and S atom, which will lower the phonon vibration frequency which keeps more phonons located in the relatively low-frequency region. The phonon DOSs of MoS_2 in structure AB in Figure 5.11 are the comprehensive results of the weakening of the Mo-S bond. It can also be demonstrated by Figure 5.12(c). Figure 5.12(c) shows the plane-averaged electron density difference along the z direction to differentiate the impact of three different lattice-stacking configurations. It is obvious that AB reveals the largest electron accumulation at the plane of Mo atom compared with the other two structures. On the other hand, AA(Mo) has the largest electron accumulation at the interface between S-Sc, which enhances the interaction between the MoS_2 and Sc substrate leading to the increase of the phonon transmission and TBC. The results are also consistent with our previous conclusions.

5.6 Closure

In summary, this chapter investigate the role of interfacial electronic properties on the phonon transport at the interface of monolayer MoS_2 and metal substrates. Different degree of orbital hybridization caused by the introduction of a metal substrate affects the interfacial phonon-phonon coupling and phonon transmission significantly. Strong chemical coupling between MoS_2 and the Sc substrate leads to a 19 times higher TBC than that of the weakly bound MoS_2/Au system. For MoS_2 on the Sc substrates, a strong charge

transfer from Sc to MoS_2 can be demonstrated by the significant portion of the previous conduction band states occupied below Fermi level. Furthermore, the effect of interfacial lattice-stacking configurations of MoS_2/Sc leads to a significant redistribution of phonon DOSs and transmission at the interface. The extra charge transfer further weakens the Mo-S bond strength in lattice-stacking configuration of structure AB compared to structure AA(Mo). The resultant decrease in the force constant between Mo and S atoms keeps more phonons located in a low-frequency region which results in a 60 % decrease in TBC. The findings in this study demonstrate the inherent connection among the interfacial electronic structure, the phonon distribution, and TBC.

CHAPTER 6 : PHONON MODE CONTRIBUTIONS TO THERMAL CONDUCTIVITY OF PRISTINE AND DEFECTIVE β-GA2O3

In this study, the first-principles density functional theory along with the Boltzmann Transport Equations (BTE) is used to predict the phonon transport properties of pristine and defective β-Ga_2O_3. The thermal conductivities of bulk β-Ga_2O_3 along three crystal directions are calculated based on the iterative solution of the BTE. Our predictions of thermal conductivity using the conventional unit cell is in better agreement with the experimental results[107-109] than the previous theoretical study[106]. To better understand the influence of defects on the phonon transport mechanism, the thermal conductivities with 1-2% oxygen and gallium vacancies are further investigated respectively. The model for estimating the effect of point vacancies on phonon properties is developed by considering contributions of the defect-induced phonon scattering, which is caused by the missing mass of the oxygen or gallium atoms. Phonon modes contribution to the thermal conductivity is studied along with the influence of the point vacancies.

6.1 Simulation Setup and Model Parameters

β-Ga_2O_3 is a monoclinic crystal with space group C2/m containing 20 atoms per conventional unit cell. Although recent work[218] reported that they have resolved the ambiguity in defining the Brillouin zone for transferring the conventional monoclinic unit cell to a reduced primitive cell, the 20-atom conventional unit cell (Figure 6.1) is used instead of the 10-atom unit cell in order to exclude the potential risk of the Brillouin zone transfer. Considering this, the conventional unit cell will provide the anisotropic thermal conductivity along three crystallographic directions directly.

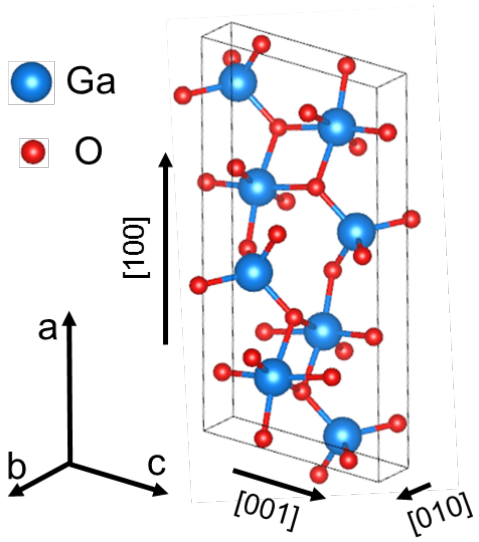

Figure 6.1 The conventional unit cell of the bulk β-Ga_2O_3. The blue and red spheres represent gallium atoms and oxygen atoms, respectively.

6.1.1 Structure Optimization and 2nd and 3rd IFCs Calculation of bulk β-Ga_2O_3

The first-principles DFT simulation is performed to calculate the total energy of the bulk β-Ga_2O_3 by Vienna ab initio simulation package (VASP).[219] A plane-wave basis set and the projector augmented-wave (PAW) method are used with Perdew, Burke, and Ernzerhof (PBE) exchange–correlation functional.[189, 220, 221] 500 eV kinetic energy cutoff is used to perform the structure optimization and calculate the second-order harmonic and third-order anharmonic interatomic force constants (IFCs). The system energy convergence criterion is set to be 10^{-9} eV. The force convergence criterion is set to be -0.001eV/Å. The unit cell of the β-Ga_2O_3 with 20 atoms shown in Figure 6.1 is optimized with a 4×16×8 grid for Brillouin zone sampling. The optimized lattice parameters are a=12.45 Å, b=3.08 Å, and c=5.86 Å with β=103.76°, which are in good agreement with the computational [106] and experimental results [222]. Using these optimized lattice parameters, the 1×4×2 supercell of the 20-atom unit cell is assembled for

the calculations of the second-order harmonic IFCs and third-order anharmonic IFCs. The displacement length of each atom from its equilibrium position is 0.01 Å. The interactions between atoms up to the 4th nearest neighboring shell are taken into account for the third-order IFCs calculation.

6.1.2 Model of Defective bulk β-Ga_2O_3 with Oxygen or Gallium Vacancies

Using the second-order and third-order IFCs obtained from the first-principles calculations, the phonon relaxation times and the anisotropic thermal conductivities of bulk β-Ga_2O_3 along various directions can be calculated using Fermi's Golden rule[183] with the iterative solution of the Boltzmann transport equation.[181, 185] The effects of oxygen or gallium vacancies in the bulk β-Ga_2O_3 on the phonon scattering rate and thermal conductivity are also considered by adding the defect-induced phonon scattering to the anharmonic phonon scattering rate:[119]

$$1/\tau = 1/\tau_{\text{anh}} + 1/\tau_{\text{V}} \tag{6-1}$$

where $1/\tau_{\text{anh}}$ is the intrinsic anharmonic phonon scattering rate. $1/\tau_{\text{V}}$ is the defect-induced phonon scattering rate which is caused by the missing of oxygen or gallium atoms in the crystal. It can be expressed as [223-226]

$$1/\tau_{\text{V}} = x(-\frac{M_V}{M} - 2)^2 \frac{\pi}{2} \frac{\omega^2 g(\omega)}{G} \tag{6-2}$$

where x is the density of vacancies, M is the average mass per atom, M_V is the mass of the missing atom, $g(\omega)$ is the phonon density of states (DOSs), G is the number of atoms in the crystal.

6.2 Thermal Conductivity of bulk β-Ga_2O_3 Vs. GaN

Results indicate that β-Ga_2O_3 has a significant anisotropy of the thermal conductivity along three directions of basis vectors of the conventional unit cell, see Figure 6.2. The largest thermal conductivity of β-Ga_2O_3 is observed in the direction of [010] with the value of 20.00 W/mK at the room temperature. Our observation has a better agreement with the experimental results [107-109] compared to the previous theoretical study [106] as shown in Table 6.1. The thermal conductivity of the bulk β-Ga_2O_3 is fitted to the functional form of $\kappa(T) = AT^{-m}$. The fitting value of each parameter in the equation is listed in the Table 6.2.

Table 6.1 Thermal conductivity of the bulk β-Ga_2O_3 at 300K

Crystallographic orientation	This study	Experiment	Simulation[106]
[100]	12.73	10.9± 0.7,[107] 13± 1.[108]	16.06
[010]	20.00	27.1±2,[107] 21.[109] 29.21[32]	21.54
[001]	17.80	14.7±1.4.[107]	21.15

Table 6.2 The thermal conductivity of the bulk β-Ga_2O_3 is fitted to a functional form of $\kappa(T) = AT^{-m}$ (T>200K). The fitting value of each parameter in the equation is listed in the table.

Crystallographic orientation	This study		Experiment[107]		Simulation[106]	
	A ($\times 10^4$)	m	A($\times 10^4$)	m	A($\times 10^4$)	m
[100]	1.35	1.22	1.06	1.21	1.99	1.13
[010]	2.01	1.21	3.28	1.27	2.47	1.27
[001]	1.78	1.20	0.814	1.12	3.5	1.26

The temperature dependent thermal conductivity of bulk β-Ga_2O_3 with bulk GaN are compared in Figure 6.2. The thermal conductivity of bulk β-Ga_2O_3 is much lower than that of GaN, which can be explained by the phonon lifetime shown in Figure 6.3(a). β-Ga_2O_3 has a much shorter phonon lifetime than GaN in the entire frequency domain. This is supported by the three-phonon scattering phase space in Figure 6.3(b) which indicates the volume of phase space available for three-phonon scattering. This could be a consequence of smaller band-gap or absence of band-gap between acoustic and optical phonon bands of β-Ga_2O_3 in difference crystallographic directions (see Figure 6.5(a)). The three-phonon scattering phase space is another way to indicate the likelihood of phonons being scattered. It shows that the phase space of the β-Ga_2O_3 is larger than that of the GaN, which means GaN has fewer channels for three-phonon scatterings leading to the longer phonon lifetime and larger thermal conductivity.

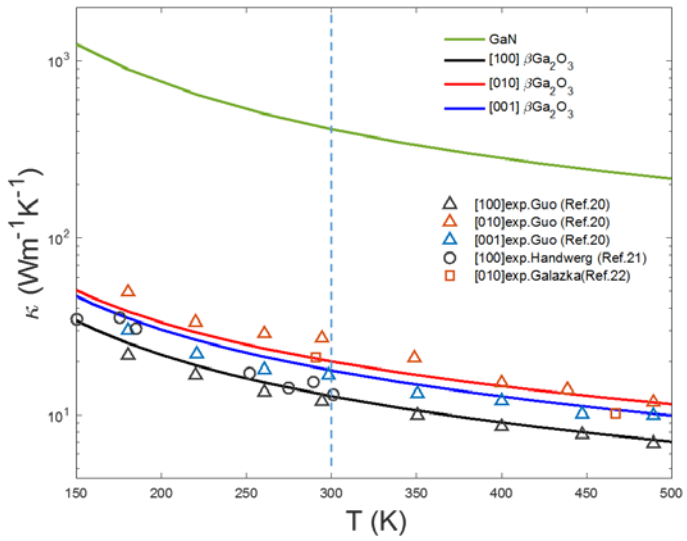

Figure 6.2 Temperature-dependent thermal conductivity of the bulk β-Ga_2O_3 and GaN compared to the experimental measurements.

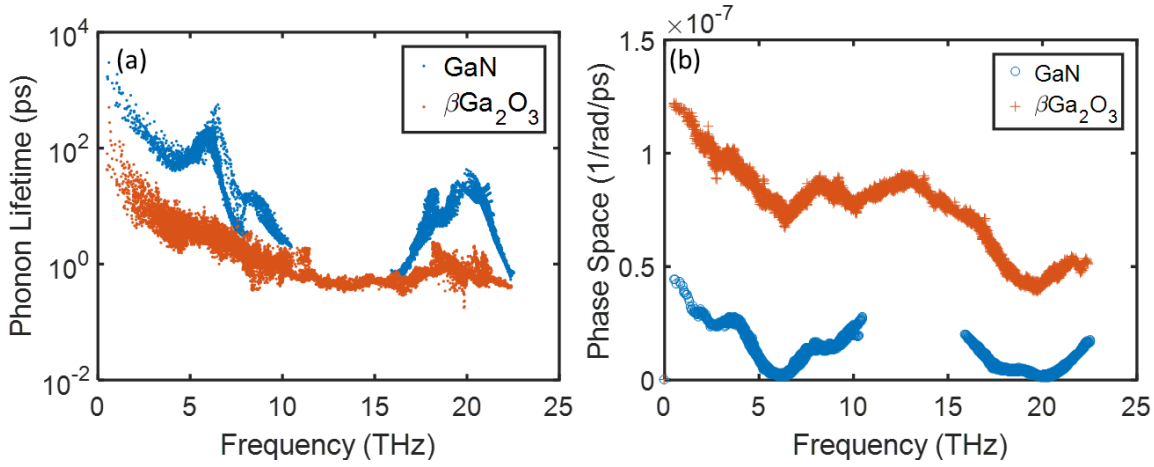

Figure 6.3 (a) Angular frequency dependent phonon lifetime of the bulk β-Ga_2O_3 and GaN at 300K. (b) Three-phonon scattering phase space of the bulk β-Ga_2O_3 and GaN.

6.3 Contribution of Phonon Modes to Thermal Conductivity

To better understand the mechanism of phonon transport in β-Ga_2O_3, the phonon modes' contributions to the thermal conductivity along three directions are calculated, which is shown in Figure 6.4. Results show that the optical modes make a significant contribution to the thermal conductivity compared to the acoustic modes, especially in the [010] direction. However, this observation is not consistent with the assumption that typically acoustic modes have the dominant contribution to the thermal transport and that the optical modes' contribution is negligible, which is observed for some semiconductors such as graphene, MoS_2.[76, 227] To further understand it, the phonon dispersions are calculated along three basis vectors of the conventional unit cell which is shown in Figure 6.5(a). One of the explanations for the high contribution of optical modes is that the group velocities of the optical modes can't be neglected (Figure 6.5 (a)). Smaller band-gap between acoustic and optical phonon bands and hence larger three-phonon scattering phase space are also attributed to low conductivity. However, this can't explain the observation

of the largest thermal conductivity of β-Ga_2O_3 in the direction of [010] in both simulations and experiments considering the fact that no band-gap is observed along [010] direction, while gaps exist in [100] and [001] directions; this is also mentioned by Santia.[106] In Figure 6.4, results show that the optical modes have 53.45% contribution to the thermal conductivity in [010] which don't have optical phonon band-gap, but 36.98% and 39.18% in [100] and [001], respectively, which have the gaps. Compared to [010], relative flat optical phonon branches can be observed in [100] and [001], which suggest smaller phonon group velocities and low thermal conductivity. Actually, strong contribution of optical modes to conductivity has been found in other semiconductor materials such as GaN.[100]

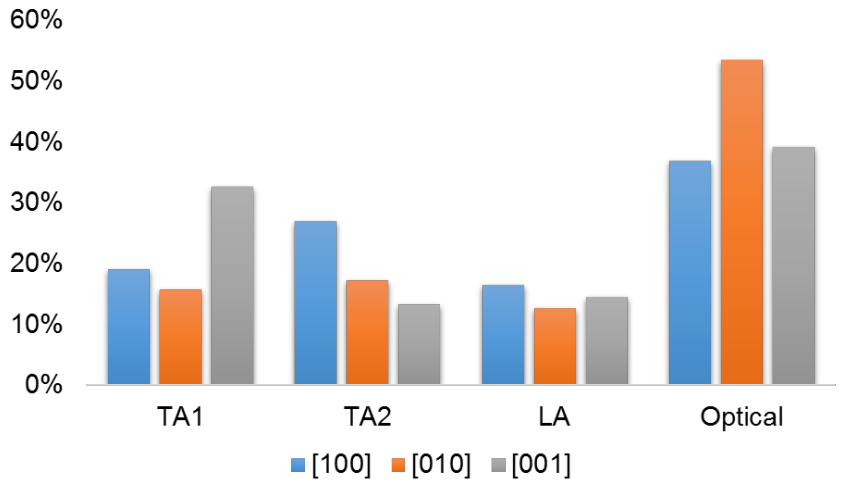

Figure 6.4 Phonon mode contribution to the thermal conductivity of pristine bulk β-Ga_2O_3 along three basis vectors of the conventional unit cell at the room temperature.

In addition, for acoustic modes, the TA2 mode has the largest contribution in [100] and [010] directions. The TA1 mode has the largest contribution in [001] direction. This can be explained by the flattening of the LA modes which may be caused by the hybridization between the low energy optical modes and LA modes. As a result, the lower

group velocities of LA phonons result in a lower thermal conductivity. The hybridization is also another reason for the strong optical phonon contributions.

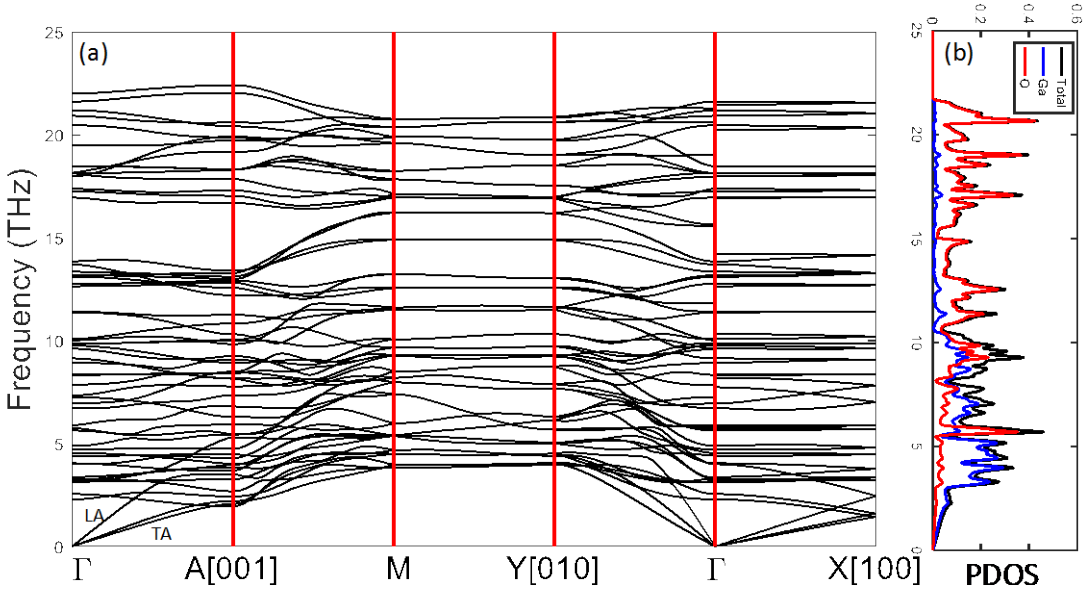

Figure 6.5 (a) Phonon dispersions of the bulk β-Ga_2O_3 with the conventional unit cell. (b) Phonon partial density of states (PDOS) of the bulk β-Ga_2O_3, gallium atoms and oxygen atoms.

6.4 Effect of Point Defects on the Thermal Transport of Bulk β-Ga_2O_3

In order to understand how the phonon transport and modes contribution influenced by the defects, the anharmonic and defect-induced phonon scattering rates of β-Ga_2O_3 are plotted in Figure 6.6(a), the thermal conductivity of bulk β-Ga_2O_3 with 1-2% oxygen and gallium vacancies along three crystallographic directions in Figure 6.6(b-d), and phonon mode contribution to the thermal conductivity under the influence of oxygen vacancies in Figure 6.7. Results indicate that at room temperature, 1% and 2% oxygen vacancies decrease the thermal conductivity by 8.5% and 14.3% in [100] direction, 14.9% and 24.1% in [010] direction, 10.7% and 17.4% in [001] direction, respectively. 1% and 2% Ga

vacancies decrease the thermal conductivity by 16.6% and 25.3% in [100] direction, 27.6% and 39.4% in [010] direction, 20.4% and 29.9% in [001] direction, respectively. For future convenience in device modeling, the thermal conductivities of the defective bulk β-Ga_2O_3 with the O and Ga vacancies are also fitted to the functional form of $\kappa(T) = AT^{-m}$. The fitting value of A and m in the equation can be found in the Table 6.3. Based on our defect model (Eq.(6-1,2)), the missing atom at a vacancy site results in a mass difference (compared to the average mass of the cell), which results in the kinetic energy and potential energy change. The defect-induced phonon scatterings result in the suppression of the thermal conductivity. Due to the heavier mass of the gallium atom than that of the oxygen atom, the gallium point vacancies could result in the larger kinetic energy and potential energy change than oxygen vacancies, which leads to larger defect-induced phonon scattering and suppression in the thermal conductivity.

Table 6.3 The thermal conductivity of the bulk β-Ga_2O_3 under the influence of oxygen vacancies and gallium vacancies is fitted to a functional form of $\kappa(T) = AT^{-m}$ (T>200K). The fitting value of each parameter in the equation is listed in the table.

Crystallographic orientation	O vacancy (1%)		O vacancy (2%)		Ga vacancy (1%)		Ga vacancy (2%)	
	A($\times 10^3$)	m	A($\times 10^3$)	m	A($\times 10^3$)	m	A($\times 10^3$)	m
[100]	8.92	1.16	6.26	1.11	5.42	1.09	3.32	1.03
[010]	6.27	1.04	3.23	0.96	2.84	0.93	1.43	0.84
[001]	9.94	1.13	6.67	1.07	5.71	1.05	3.44	0.98

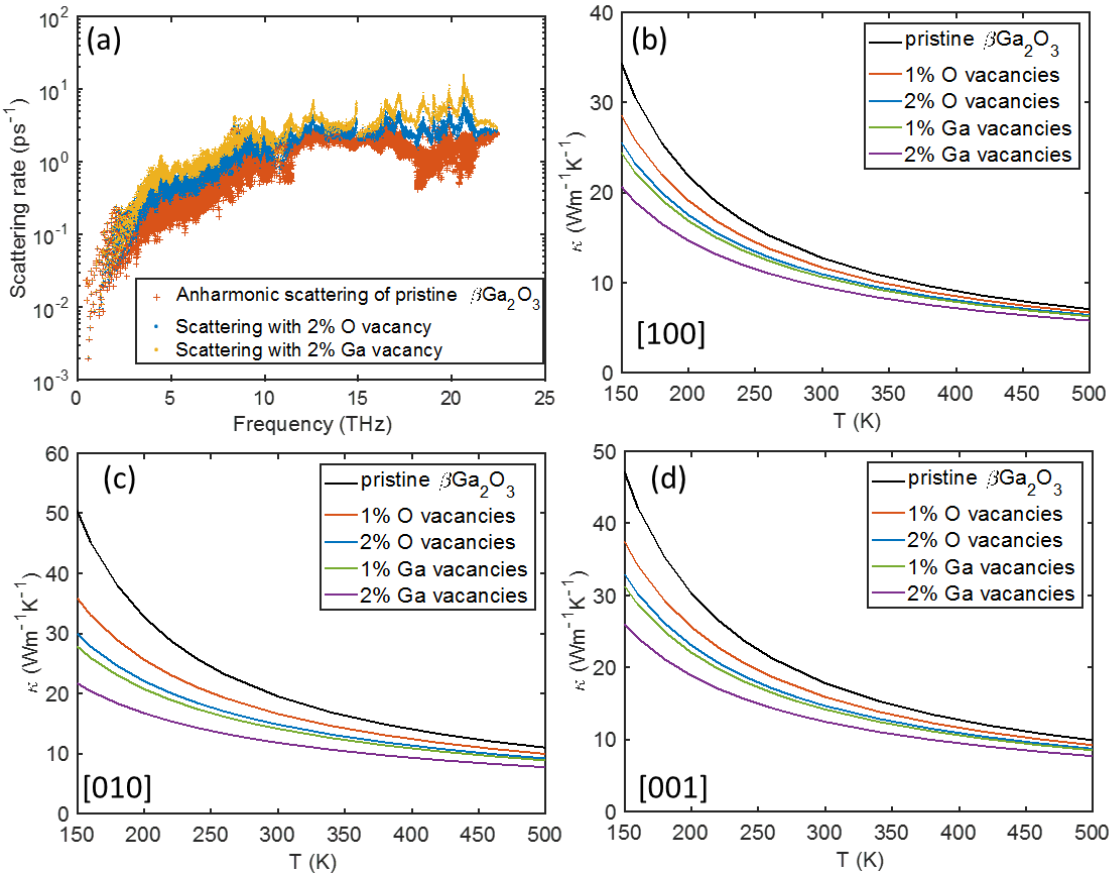

Figure 6.6 (a) Angular frequency dependent anharmonic and defect-induced phonon scattering rates of the bulk β-Ga_2O_3 with 2% oxygen vacancies and gallium vacancies at 300K, respectively (b-d) Temperature-dependent thermal conductivity of the defective β-Ga_2O_3 with oxygen and gallium vacancies along the direction of (b) [100], (c) [010], (d) [001].

Furthermore, the oxygen vacancies have more influence on the optical modes than that on the acoustic modes, which leads to larger suppression in the contribution of optical modes to the thermal conductivity. In other words, under the influence of defects, the percentage of acoustic modes' contribution to the thermal conductivity increases, although the absolute value of thermal conductivity contribution is decreased. To illustrate why the introduced oxygen vacancies suppress the contribution of the optical phonon modes to the thermal conductivity, the phonon partial density of states (PDOS) of the bulk β-Ga_2O_3 are

investigated in Figure 6.5(b). Results indicate that the DOSs of the optical modes are larger than those of acoustic modes. In addition, oxygen atoms in the bulk β-Ga_2O_3 make the most contribution to the optical energy. Due to the correlation between the phonon DOSs and the defect-induced phonon scattering rate as shown in Eq. (6-2), the defect-induced phonon scatterings for optical modes would have higher impact on the thermal conductivity than that of acoustic modes. The gallium vacancies have similar effects and trends on the mode contributions to the thermal conductivity.

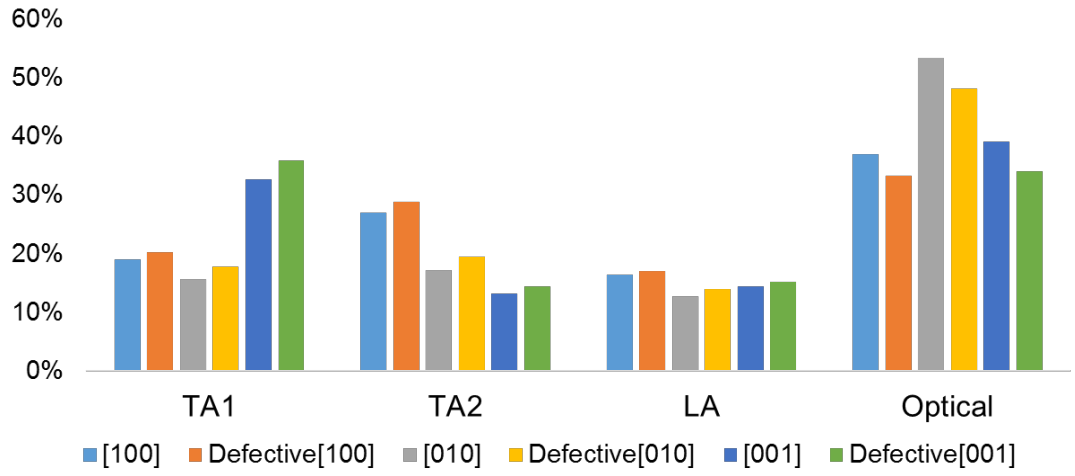

Figure 6.7 Phonon mode contribution to the thermal conductivity of defective bulk β-Ga_2O_3 under the influence of 1% oxygen vacancies along three crystallographic orientation at the room temperature.

6.5 Closure

In summary, the thermal conductivity and phonon mode contributions of pristine and defective β-Ga_2O_3 are investigated by the first principles calculation and the phonon Boltzmann transport equation. For the pristine β-Ga_2O_3, the thermal conductivity of 12.73 W/mK, 20.00 W/mK, 17.80 W/mK in the direction of [100], [010], [001], are reported respectively, which have a better agreement with the experimental results than the previous

study. The optical phonon modes make a significant contribution to the thermal conductivity compared to the acoustic modes, especially in the [010] direction because of the non-negligible group velocities at optical branches and the hybridization between the low energy optical modes and LA modes. For the bulk β-Ga_2O_3 with oxygen vacancies, 1% and 2% oxygen vacancies decrease the thermal conductivity by 8.5% and 14.3% in [100] direction, 14.9% and 24.1% in [010] direction, 10.7% and 17.4% in [001] direction, respectively at the room temperature. 1% and 2% Ga vacancies decrease the thermal conductivity by 16.6% and 25.3% in [100] direction, 27.6% and 39.4% in [010] direction, 20.4% and 29.9% in [001] direction, respectively due to the larger defect-induced phonon scatterings. Furthermore, the vacancies have more influence on the optical modes than that on acoustic modes, which leads to larger suppression of the contribution of optical modes to the thermal conductivity.

CHAPTER 7 : INFLUENCE OF DEFECTS AND DOPING ON PHONON TRANSPORT PROPERTIES OF MONOLAYER MOSE2

This chapter present the study of the phonon transport properties of monolayer $MoSe_2$ considering the effects of scattering by the boundary, defects, and doping. The first-principles density functional theory (DFT) along with the phonon Boltzmann transport equation (BTE) is performed in this chapter. The effect of sample size on thermal conductivity at different temperatures is studied along with the influence of Se vacancies. The model for estimating the effect of Se vacancies on phonon properties of the monolayer $MoSe_2$ is developed by considering contributions of two different types of the defect-induced phonon scatterings: one caused by the missing mass of the Se atoms, the other caused by the change of force constants between the under-coordinated atoms near the vacancies. To further illustrate how the Se vacancies affect the phonon transport in the monolayer $MoSe_2$ meanwhile suppressing the Se vacancy concentration, the phonon property of the monolayer $MoSe_2$ with 16.7% W doping is investigated. This percentage of W doping is selected for the present study because samples with such percentage doping has been fabricated and Se vacancy suppression has been demonstrated in References.[127, 228]

7.1 Computational Methods and Simulation Setup

7.1.1 Structure Optimization and 2nd and 3rd IFCs Calculation of Monolayer $MoSe_2$

Total energy calculations are based on the first-principles DFT as implemented in the VASP.[219] A plane-wave basis set and the projector augmented-wave (PAW) method

are used with Perdew, Burke, and Ernzerhof (PBE) exchange–correlation functional.[189, 220, 221] The kinetic energy cutoff of the supercell is 500 eV. The system energy convergence criterion is set to be 10^{-9} eV. The force convergence criterion is set to be -0.01eV/Å. The structure of monolayer $MoSe_2$ shown in Figure 7.1(a) is optimized with an 18×18×1 grid for Brillouin zone sampling. An 18 Å vacuum space along the z-axis is used to eliminate the interaction emerging from the periodic boundary condition. The lattice constant of the monolayer $MoSe_2$ is obtained with the value of 3.32 Å, which is in good agreement with the theoretical result of 3.32 Å, [120] and the experimental result of 3.30 Å.[229]

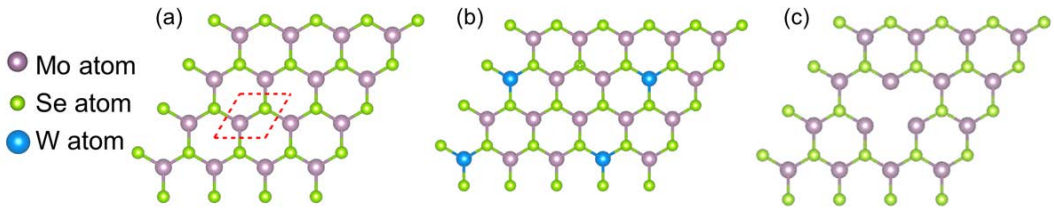

Figure 7.1 Top view of the structure of (a) monolayer $MoSe_2$, (b) W doped monolayer $MoSe_2$, (c) monolayer $MoSe_2$ with Se vancancies (schematic). The purple, green, and blue spheres represent molybdenum, selenium, and tungsten atoms, respectively.

Using this optimized lattice constant, the 6×6 and 4×4 supercells of monolayer $MoSe_2$ with 3×3×1 k-point grid are assembled for the calculations of the second-order harmonic and third-order anharmonic interatomic force constants (IFCs), respectively. The displacement length of each atom from its equilibrium position is 0.01 Å. The interactions between atoms up to the 4th nearest neighboring shell are taken into account for the third-order IFCs calculation.

7.1.2 Model of Defective $MoSe_2$ with Selenium Vacancies

Using the second-order and third-order IFCs obtained from the first-principles calculations, the phonon relaxation times and thermal conductivities of monolayer $MoSe_2$ can be calculated using Fermi's Golden rule[183] with the relaxation time approximation (RTA) and the iterative solution of the Boltzmann transport equation.[122, 181, 184, 185] The in-plane thermal conductivity tensor of monolayer $MoSe_2$ can be calculated as a sum of the contribution of all phonon modes λ based on the relaxation time approximation [122]

$$\kappa_{\alpha\alpha} = \frac{2}{N\sqrt{3}a_0^2 h}\sum_{\lambda}\frac{\partial n_{\lambda}^0}{\partial T}(\hbar\omega_{\lambda})v_{\lambda}^{\alpha}v_{\lambda}^{\alpha}\tau_{\lambda} \qquad \textbf{(7-1)}$$

where N is the number of uniformly spaced q points in the Brillouin zone, a_0 is the lattice constant, and h is the thicknesses of the monolayers. v_{λ}^{α} is the group velocity along the α direction, and τ is the phonon lifetime.

In addition, following the Matthiessen's rule,[230] the size dependent thermal conductivity at different temperatures can be calculated by combining the phonon scattering due to anharmonicity and boundary. The relaxation time due to boundary scattering could be written as

$$\frac{1}{\tau_{\mathrm{b}}} = \frac{\upsilon_{\lambda}}{L}\frac{1-p}{1+p} \qquad \textbf{(7-2)}$$

where L is the characteristic length of the sample, υ_λ is the phonon group velocity. This work expects that the boundary scattering is predominantly diffusive, where p=0. [231, 232]

Furthermore, the effects of Se vacancies in the monolayer $MoSe_2$ on the phonon scattering rate and thermal conductivity are considered by adding two different types of the defect-induced phonon scattering to the total phonon scattering rate:

$$1/\tau = 1/\tau_{anh} + 1/\tau_b + 1/\tau_V + 1/\tau_F \quad \textbf{(7-3)}$$

where $1/\tau_{anh}$ and $1/\tau_b$ are the intrinsic anharmonic phonon scattering rate and phonon boundary scatting rate, respectively. $1/\tau_V$ is the scattering rate caused by the missing mass of the Se atom in the crystal, and $1/\tau_F$ is the scattering rate caused by the change of force constants between the under-coordinated atoms near the vacancies. They can be expressed as[223-226],

$$1/\tau_V = x(-\frac{M_V}{M} - 2)^2 \frac{\pi}{2} \frac{\omega^2 g(\omega)}{G} \quad \textbf{(7-4)}$$

$$1/\tau_F = x(\frac{\delta C}{C})^2 4\pi \frac{\omega^2 g(\omega)}{G} \quad \textbf{(7-5)}$$

where x is the density of vacancies, M is the average mass per atom, M_V is the mass of the missing atom, $g(\omega)$ is the phonon density of states (DOSs), G is the number of atoms in the crystal and C is the force constant.

7.2 Effect of Boundary Scatterings on the Thermal Conductivity

Figure 7.2 presents the size-dependent thermal conductivity of monolayer $MoSe_2$ at different temperatures. Results show that the phonon boundary scattering has a significant influence on the thermal conductivity if the sample size is smaller than 1 μm. Below that size, most of the phonons will have a higher probability to hit the boundary before they scatter with other phonons[122]. Furthermore, the boundary effects also play a significant role in the thermal conductivity at the low temperature. It is because the strength of the Umklapp three-phonon process[233] at low temperatures is relatively weak and the phonon boundary scattering becomes much more dominant in the phonon transport process. On the other hand, at high temperatures (> 800K), the size effect can be ignored because the phonon transport is dominated by the strong Umklapp process.

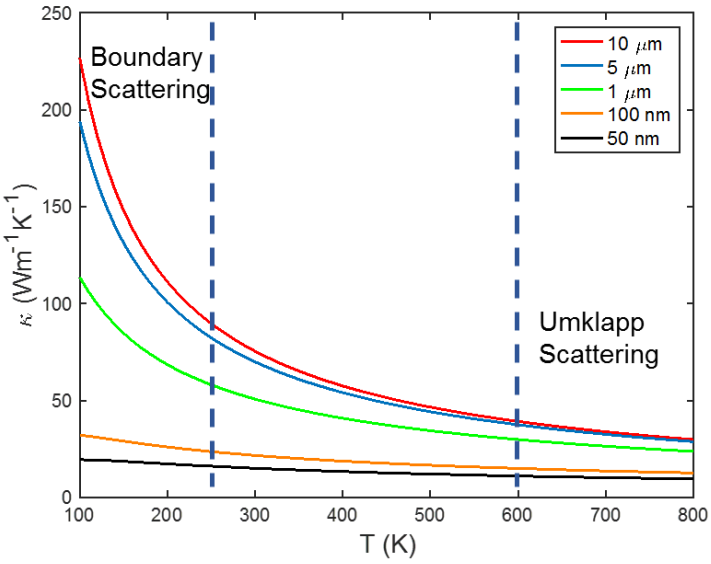

Figure 7.2 Size-dependent thermal conductivity of monolayer $MoSe_2$ as a function of temperature.

7.3 Effect of Se Vacancy on the Thermal Conductivity of Monolayer $MoSe_2$

Besides the boundary effects, defects also have a significant impact on the thermal conductivity of monolayer $MoSe_2$. Figure 7.3 shows the temperature-dependent thermal conductivity and Figure 7.4 indicates the phonon lifetime of monolayer $MoSe_2$ with Se vacancies. The calculations are based on the sample size of 2 μm. Results indicate that 1%, 2% and 4% Se vacancies decrease the thermal conductivity of monolayer $MoSe_2$ by 27.7%, 39.5% and 51.9%, respectively at room temperature.

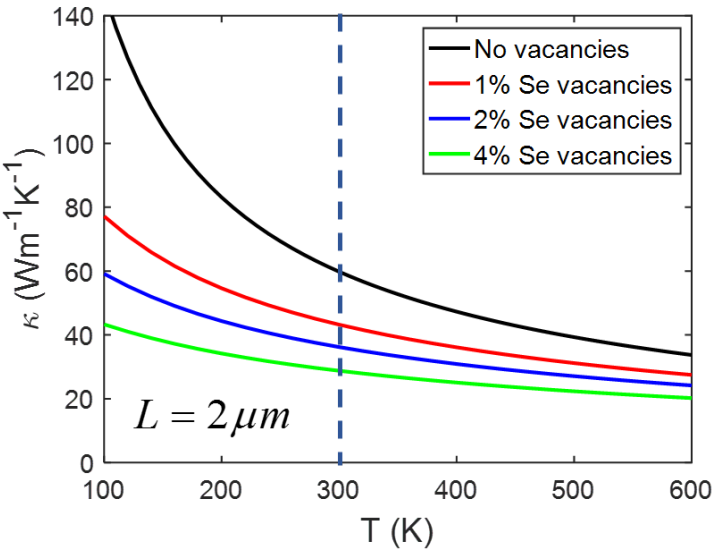

Figure 7.3 Temperature-dependent thermal conductivity of monolayer $MoSe_2$ with Se vacancies. The sample size is 2μm.

In our model (Eqs. (7-4), (7-5)), the effect of Se vacancies in crystals on phonon transport is treated by perturbation theory, i.e., contribution to the phonon scattering rate by two different types of the defect-induced phonon scatterings. One corresponds to the missing mass of the Se atoms, which implies the removal of the kinetic energy and potential energy. The other corresponds to the change of force constants between the under-

coordinated atoms near the vacancies. Both of these defect-induced phonon scattering increase the total phonon scattering rate and decrease the phonon lifetime in the entire frequency range (Figure 7.4). Furthermore, this study also finds that the defect-induced phonon scattering rate caused by the change of the force constants near the vacancies has more impact on the total thermal conductivity than that caused by the atom mass missing as shown in Figure 7.5. Results indicate that Se vacancies have a weak impact on the thermal conductivity at high temperatures. It is because that the three-phonon scattering rates corresponding to anharmonicity become dominant at high temperatures and the scattering rates corresponding to the defect related terms, $1/\tau_V$ and $1/\tau_F$ in Eq. 1, have less contribution to the total phonon scattering rate.

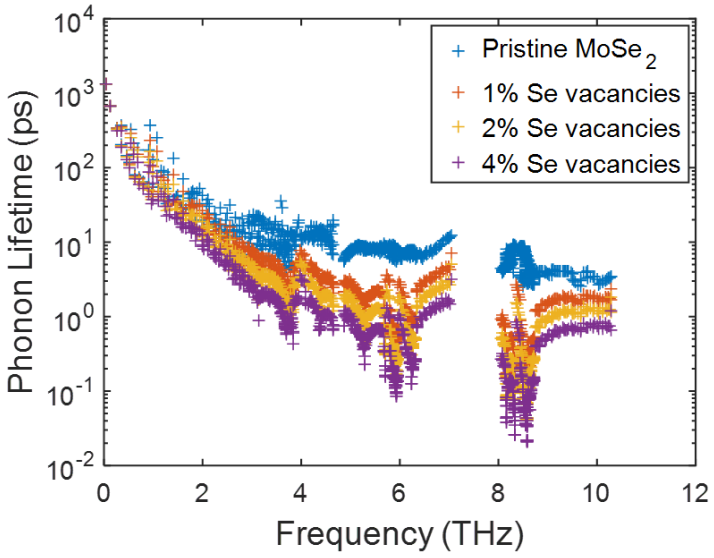

Figure 7.4 Angular frequency dependent phonon lifetime of monolayer $MoSe_2$ with Se vacancies at 300K.

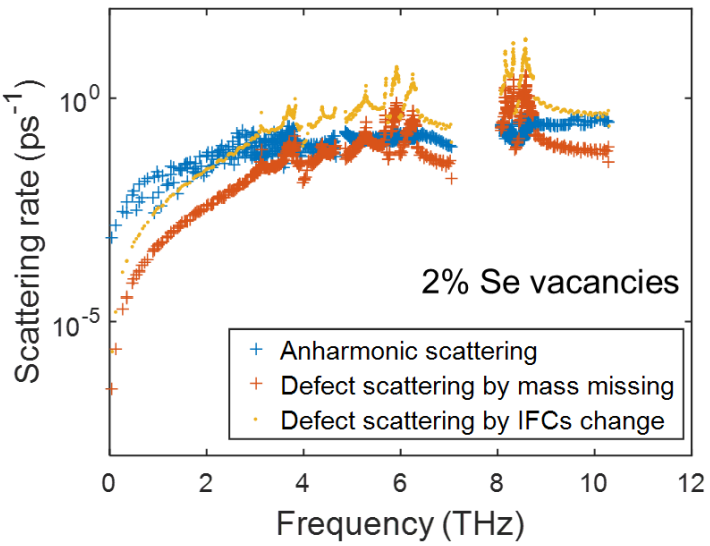

Figure 7.5 Anharmonic and two types of defect-induced phonon scattering rates (due to mass missing and IFC change) of monolayer $MoSe_2$ with 2% Se vacancies.

7.4 Effect of Tungsten Doping on the Thermal Conductivity of Monolayer $MoSe_2$

In order to understand the influence of methods to suppress the defect concentration in the monolayer $MoSe_2$, we study the phonon transport property of $MoSe_2$ under the influence of the W doping. The structure of the W doped monolayer $MoSe_2$ used in this work is shown in Figure 7.1(b), which is optimized with the same lattice constant as of monolayer $MoSe_2$. The concentration of W atoms is about 16.7%, which makes the W doped $MoSe_2$ as $Mo_{0.83}W_{0.17}Se_2$. The 2×2 supercell of monolayer $MoSe_2$ is assembled for the calculations of the second-order harmonic and third-order anharmonic interatomic force constants (IFCs). Figure 7.6 shows the temperature-dependent thermal conductivity of monolayer pristine $MoSe_2$ and W doped $MoSe_2$ with various sample sizes. Results show that the W doping increases the thermal conductivity of monolayer pristine $MoSe_2$. In addition, the difference becomes larger as the temperature increases (Figure 7.6).

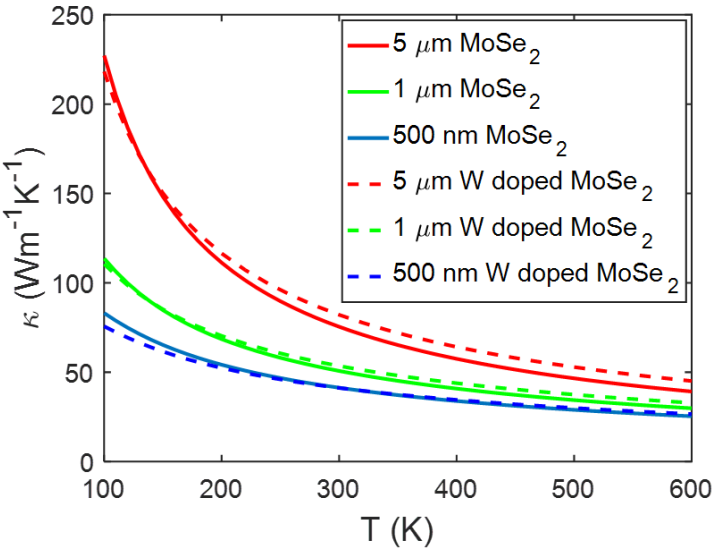

Figure 7.6 Temperature-dependent thermal conductivity of monolayer pristine $MoSe_2$ and W doped $MoSe_2$ with various sample sizes.

To better understand the impact of W doping on the thermal conductivity of the pristine $MoSe_2$, we also calculated the size-dependent thermal conductivity of the monolayer $MoSe_2$ and the W doped $MoSe_2$,which is compared to that of the monolayer WSe_2 at 300K (Figure 7.7). Results indicate that the thermal conductivity of W doped $MoSe_2$ is similar to that of the pristine $MoSe_2$ for sample sizes smaller than 1 μm. The phonon scattering from boundary effect has a greater impact on the thermal conductivity of the W doped $MoSe_2$ than that of the pristine $MoSe_2$. If the boundary scattering influence is reduced by considering large-size samples, the W doping could increase the thermal conductivity of pristine $MoSe_2$, e.g., 23.6% increase is observed for 10 μm sample (Figure 7.7). This indicates that for low sample size, boundary scattering effect is significant leading to similar conductivity but the intrinsic thermal conductivity of W doped $MoSe_2$ is higher than pristine $MoSe_2$ as observed in large-size samples.

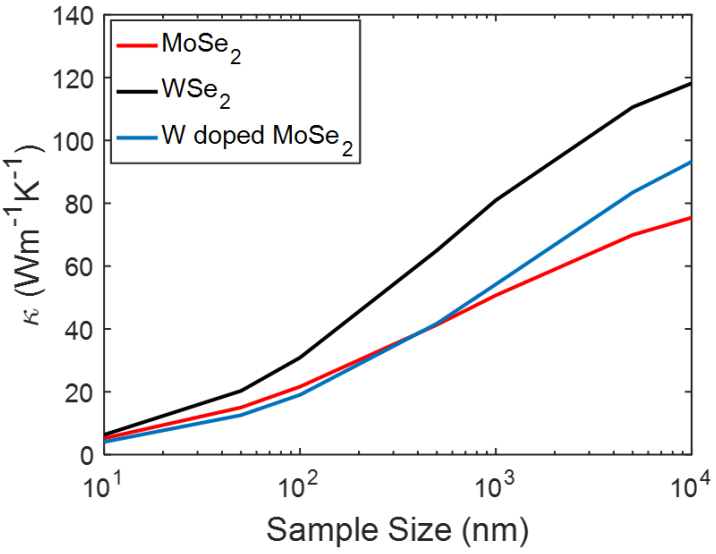

Figure 7.7 Effect of sample size on the thermal conductivity of monolayer pristine $MoSe_2$, WSe_2 and W doped $MoSe_2$ (16.7%), i.e., $Mo_{0.83}W_{0.17}Se_2$ at 300K.

To further understand it, the phonon dispersions of monolayer $MoSe_2$ and WSe_2 along $\Gamma - M$ direction are calculated which is shown in Figure 7.8(a). As expected, all the phonon branches of WSe_2 are lower in frequency than that of $MoSe_2$ because of the mass difference between W and Mo atoms. In addition, a larger gap between the optical and acoustic phonon branches in WSe_2 (1.3 THz) is observed than that in $MoSe_2$ (0.21THz). Due to the larger gap between optical and acoustic phonon branches of WSe_2, more energy is needed for the annihilation process of two acoustic phonon modes into one optical mode in WSe_2. As a result, probability of this type of phonon scatterings becomes less leading to the decrease of the Umklapp scattering strength in WSe_2 compared to the $MoSe_2$. Therefore, the thermal conductivity of the monolayer WSe_2 is larger than that of the monolayer $MoSe_2$. Introducing W atoms in the $MoSe_2$ results in thermal conductivity values between that of $MoSe_2$ and WSe_2. Furthermore, it can also be supported by the three-phonon scattering phase space in Figure 7.8(b). It indicates the volume of phase space

available for three-phonon scattering, which is another way to indicate the likelihood of phonons being scattered. The total phase space available for three-phonon processes, normal and umklapp, summing over each mode is calculated as[184, 234]

$$P_3 = \frac{2}{3\Omega}\left(\sum_j \int d\mathrm{q} D_j^{(+)}(\mathrm{q}) + \frac{1}{2}\sum_j \int d\mathrm{q} D_j^{(-)}(\mathrm{q}) \right) \quad \textbf{(7-6)}$$

where

$$D_j^{(\pm)}(\mathrm{q}) = \sum_{j',j''} \int d\mathrm{q}' \delta(\omega_j(\mathrm{q}) \pm \omega_{j'}(\mathrm{q}') - \omega_{j''}(\mathrm{q}'')) \quad \textbf{(7-7)}$$

where q, and j refer to the wave-vector and polarization of a phonon mode, respectively. $\omega_j(\mathrm{q})$ refers to the phonon frequency of mode (j,q). The prime and double prime superscripts are used to label different phonon modes involved in three-phonon scattering $\mathrm{q}'' = \mathrm{q} \pm \mathrm{q}' - \mathrm{G}$. Here, G is the reciprocal lattice vector which is zero for the normal processes and non-zero for the umklapp processes. Umklapp scattering is the dominant process for thermal resistivity at high temperatures for low defect crystals. Ω is a normalization factor equal to the unrestricted phase space for each type of process.

The phase space of the monolayer $MoSe_2$ is larger than that of the $Mo_{0.83}W_{0.17}Se_2$ as expected from the smaller phonon frequency gap between optical and acoustic branches (Figure 7.8(b)). In other words, the phonons in $Mo_{0.83}W_{0.17}Se_2$ will have fewer channels for three-phonon scatterings, which results in the relatively longer phonon relaxation time (Figure 7.10) and larger thermal conductivity.

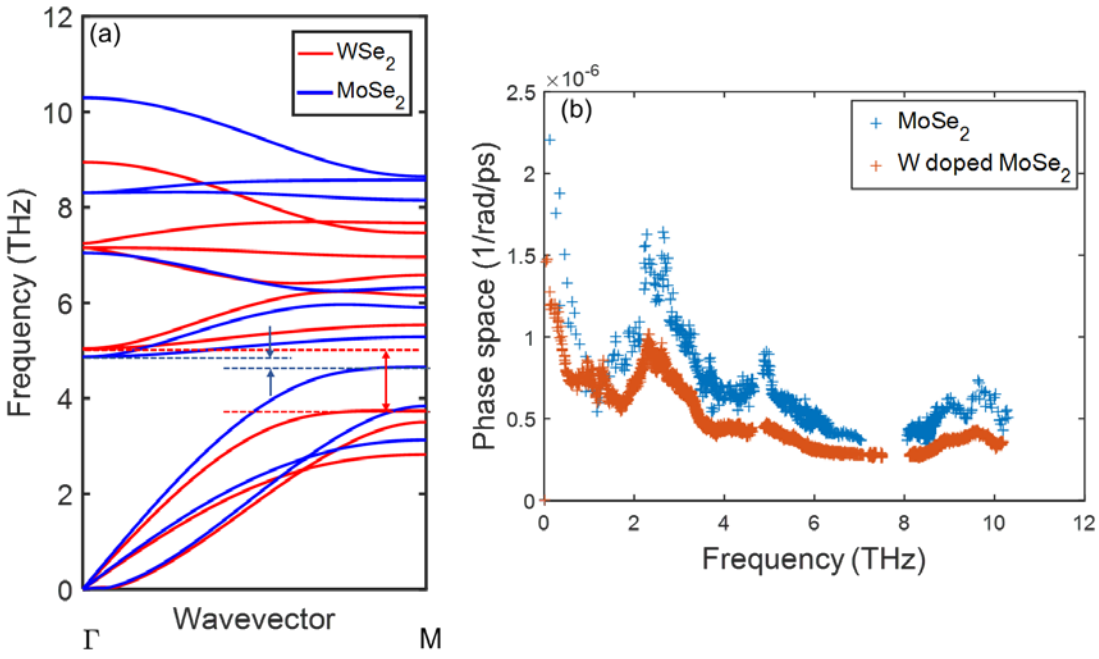

Figure 7.8 (a) Phonon dispersions of monolayer $MoSe_2$ and WSe_2 along $\Gamma - M$ direction. The gap between the acoustic modes and optical modes are marked in the figure. (b) Three-phonon scattering phase space of monolayer $MoSe_2$ and $Mo_{0.83}W_{0.17}Se_2$.

7.5 Effect of Se Vacancy on the Thermal Conductivity of W doped Monolayer $MoSe_2$

What happens to the thermal conductivity of the monolayer $MoSe_2$ if there still exist defects such as Se vacancies after the W doping? In order to investigate the impact of the defects on the thermal conductivity of the W doped $MoSe_2$, the temperature-dependent thermal conductivity and phonon lifetime of the W doped $MoSe_2$ with Se vacancies are calculated in Figure 7.9 and Figure 7.10. Results indicate that after 16.7% W doping, the existence of 1%, and 2% Se vacancy concentration decreases the thermal conductivity of the monolayer $MoSe_2$ by 34.0%, and 46.2%, respectively, at room temperature. Compared with the 27.7%, and 39.4% decrease of the thermal conductivity of monolayer $MoSe_2$ with

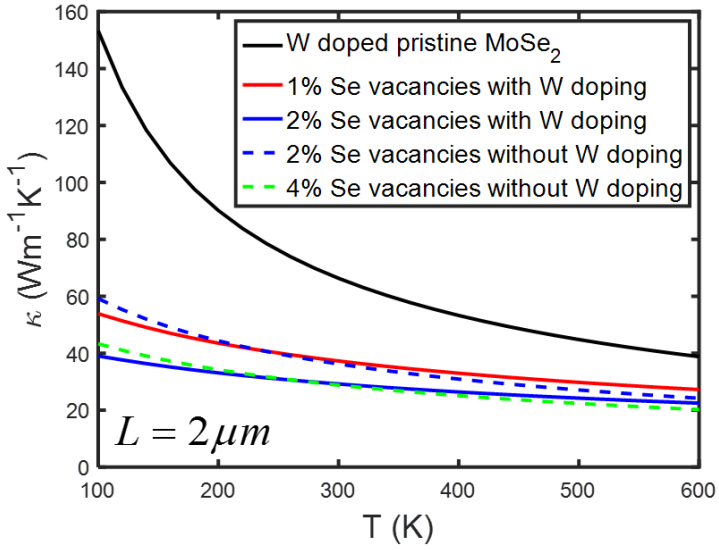

Figure 7.9 Temperature-dependent thermal conductivity of W doped $MoSe_2$ with Se vacancies. The sample size is 2μm.

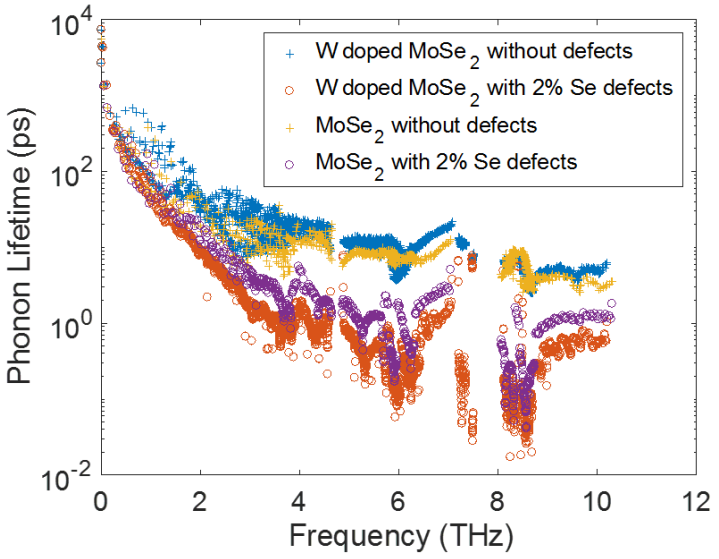

Figure 7.10 Phonon lifetime of monolayer $MoSe_2$ and W doped $MoSe_2$ with or without Se vacancies at 300K.

the same Se vacancy concentration, we find that the introduction of W atoms in the defective $MoSe_2$ amplifies the influence of the phonon scattering caused by the Se

vacancies, which results in a further decrease in thermal conductivity compared to that of monolayer $MoSe_2$ with defects. For example, the W doping suppresses the Se-vacant sites by 50% (from 4% to 2%). The thermal conductivity of the 2% defective W doped $MoSe_2$ is just 1.4% higher than that of 4% defective monolayer $MoSe_2$ in Figure 7.9. However, if the doping process makes the 2% Se-vacant $MoSe_2$ into the W doped $MoSe_2$ with no Se vacancies, the thermal conductivity can be increased dramatically by more than 80%.

To further illustrate why the introduced defects amplify the influence of the phonon scattering in the W doped $MoSe_2$, the phonon DOSs of the monolayer pristine $MoSe_2$ and $Mo_{0.83}W_{0.17}Se_2$ are investigated in Figure 7.10. Results show that in the low-frequency range, the DOSs of the $Mo_{0.83}W_{0.17}Se_2$ is larger than those of the $MoSe_2$. Due to the correlation between the phonon DOSs and the defect-induced phonon scattering rate as shown in Eqs. (7-4) and (7-5), the defect-induced phonon scatterings of the W doped $MoSe_2$ would have more impact on the thermal conductivity than that of the monolayer $MoSe_2$. In addition, it can be noticed that the $Mo_{0.83}W_{0.17}Se_2$ generates a new peak of DOSs at around 7.5THz. However, this new peak of DOSs has a very limited contribution to the thermal conductivity because the group velocities of phonons around the 7.5THz frequency are almost zero. Another explanation of how the introduced Se vacancies amplify the influence of the phonon scattering in W doped $MoSe_2$ is the mass difference between the W and Mo atoms. Since the mass of the W atom is larger than that of the Mo atom, the missing Se atom at a vacancy site results in a larger mass difference (compared to the average mass of the cell), which results in the larger kinetic energy and potential energy change. It enhances the defect-induced phonon scatterings and results in the further suppression of the thermal conductivity of the W doped $MoSe_2$.

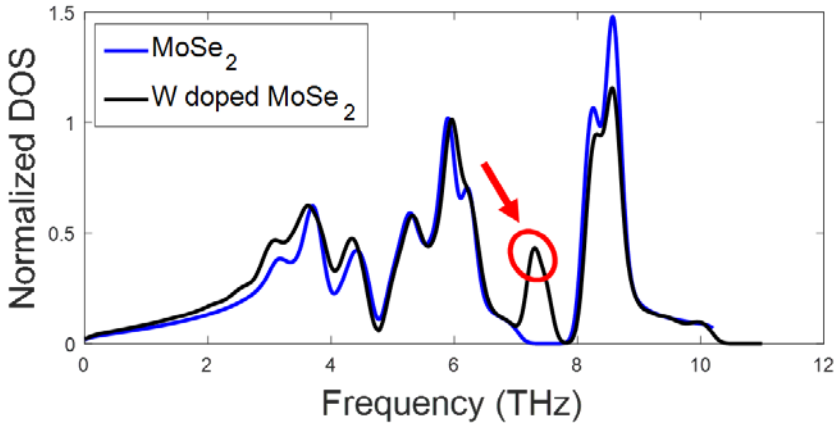

Figure 7.11 Phonon density of states of monolayer $MoSe_2$ and 16.7% W doped $MoSe_2$.

7.6 Closure

In summary, this chapter investigate the role of size, defects and W doping on thermal conductivity of monolayer $MoSe_2$ by the first principles calculation and the phonon Boltzmann transport equation. Results indicate that 1%, 2% and 4% Se vacancies decrease the thermal conductivity of monolayer $MoSe_2$ of size 2μm by 27.7%, 39.5% and 51.9%, respectively at the room temperature. However, 16.7% W doping could enhance the thermal transport of the monolayer $MoSe_2$ with 2% Se vacancy by 80% if all vacancies can be suppressed by W-doping, which could be explained by the fewer three-phonon scattering phase spaces of $Mo_{0.83}W_{0.17}Se_2$ and also supported by the larger gap between the optical and acoustic phonon branches in WSe_2 than that in $MoSe_2$. However, the W doping in the defective $MoSe_2$ amplifies the influence of the phonon scattering caused by the Se vacancies, which results in a further decrease in thermal conductivity due to the higher phonon DOSs of $Mo_{0.83}W_{0.17}Se_2$ and larger mass difference between W and Se atoms compared to Mo and Se atoms. Results indicate that for 16.7% W doping, the existence of 1%, and 2% Se vacancy concentration decreases the thermal conductivity of the monolayer

$MoSe_2$ by 34.0%, and 46.2%, respectively, at the room temperature. The results from this work will help to understand the phonon transport properties of monolayer $MoSe_2$ under the influence of defects and doping, and provide insights for the future design of $MoSe_2$-based electronics.

CHAPTER 8 : FIRST-PRINCIPLES STUDY AND MODIFIED EMPIRICAL EQUATION FOR PREDICTING THERMAL CONDUCTIVITY OF DEFECTIVE $MOSE_2$

In this chapter, the first-principles DFT and the phonon Boltzmann transport equations based simulations are used to study the phonon transport properties of pristine and defective monolayer $MoSe_2$ with Se vacancies. A model, which is fully parameter-free, is built using first-principles approach. The impact of three different types of Se vacancies on the thermal conductivity of monolayer $MoSe_2$ is studied. Phonon density of states (DOSs), and the phonon group velocities are calculated to explain the impact of defect-induced phonon states on the thermal conductivity. The findings will indicate how the vacancy-induced phonon states and the three-phonon scatterings are influenced by different type of Se vacancies. Furthermore, an empirical model to estimate the effect of Se vacancies is developed to compare with the DFT results. This modified empirical model to consider defects provides a better match with the parameter-free DFT simulation. The results from this study will help us understand the mechanism of phonon transport under the influence of different types of point defects. This work provides insights and directions for validating and improving the empirical defect model, which can be used for estimating the material properties considering the influence of defects.

8.1 Computational Methods and Simulation Setup

The energy calculations are based on the DFT simulations and are performed using the Vienna ab initio simulation package (VASP).[219] A plane-wave basis set and the projector augmented-wave (PAW) method are used with Perdew, Burke, and Ernzerhof

(PBE) exchange–correlation functional.[189, 220, 221] The kinetic energy cutoff of the supercell is 500 eV. The system energy convergence criterion is set to be 10^{-9} eV. The force convergence criterion is set to be -0.01eV/Å. The structure of monolayer $MoSe_2$ shown in Figure 8.1(a) is optimized with a 25×25×1 grid for Brillouin zone sampling. An 18 Å vacuum space along the z-axis is used to eliminate the interaction emerging from the periodic boundary condition. The optimized lattice constant of the monolayer $MoSe_2$, with the value of 3.32 Å, is in good agreement with the theoretical result of 3.32 Å, [120] and the experimental result of 3.30 Å.[229] Using this optimized lattice constant, the 6×6×1 supercells of pristine monolayer $MoSe_2$ with 3×3×1 k-point grid are assembled for the calculations of the second-order harmonic and third-order anharmonic interatomic force constants (IFCs). Three defective $MoSe_2$ crystal structures (Fig. 1(b-d)) are generated by removing one or two atoms from a 3×3×1 supercell, which make the vacancy concentration 3.7% and 7.4% respectively. The same size of the supercell for the pristine monolayer $MoSe_2$ is used for the harmonic and anharmonic IFC calculations. The displacement length of each atom from its equilibrium position is 0.01 Å. The interactions between atoms within 5.04Å are taken into account for the third-order IFCs calculation.

Using the second-order and third-order IFCs obtained from the first-principles calculations, the phonon relaxation times and thermal conductivities of monolayer pristine and defective $MoSe_2$ is calculated using Fermi's Golden rule[183] with the iterative solution of the Boltzmann transport equation[122, 181, 184, 185]. The in-plane thermal conductivity tensor can be obtained as a sum of the contribution of all phonon modes λ in Eq. (7-1). In addition, following the Matthiessen's rule,[230] the size-dependent thermal

conductivity at different temperatures can be calculated by combining the phonon scattering due to anharmonicity and boundary as shown in Eq. (8-1):

$$1/\tau = 1/\tau_{\text{anh}} + 1/\tau_{\text{b}} \quad \textbf{(8-1)}$$

Here, $1/\tau_{\text{anh}}$ and $1/\tau_{\text{b}}$ are the intrinsic anharmonic phonon scattering rate and phonon boundary scatting rate, respectively. The relaxation time due to boundary scattering could be decribed by Eq. (7-2).

8.2 Thermal Conductivity of Pristine and Defective Monolayer $MoSe_2$ with Three Types of Se Vacancies

Figure 8.1(a-d) shows the top and side views of the structures of pristine and defective monolayer $MoSe_2$. Three types of defects are investigated in this study: (b) Mono-selenium vacancy (MSeV), (c) Di-selenium vacancy (DiSeV), (d) Double mono-selenium vacancy (DMSeV). MSeV has only one Se atom missing in one 3×3 unit cell, which corresponds to vacancy concentration of 3.7%. The DiSeV and DMSeV have a vacancy concentration of 7.4% for the two Se atoms missing in the 3×3 unit cell. The difference between the DiSeV and DMSeV is the location of the Se vacancies: in the DiSeV, two Se atoms are missing at both sides of one Mo atom, while in DMSeV, two Se atoms are missing at sides of different Mo atoms. In other words, DMSeV is similar to MSeV but with the vacancy concentration doubled.

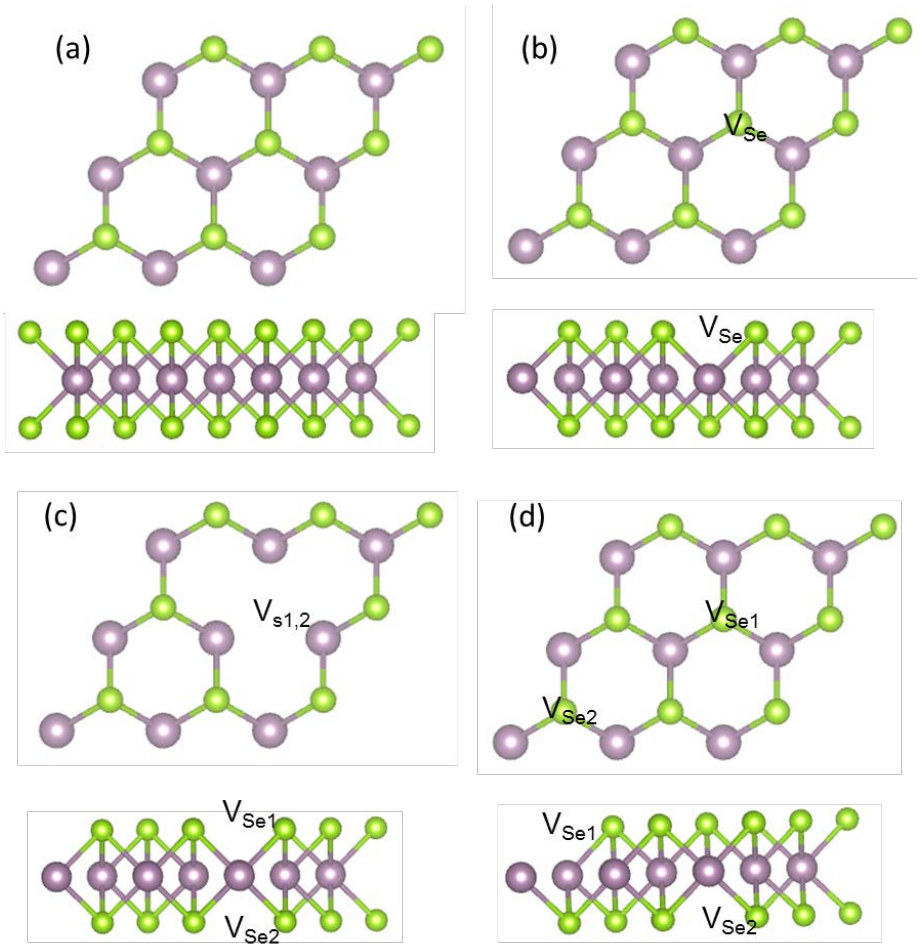

Figure 8.1 Top and side views of the structure of (a) Pristine monolayer $MoSe_2$, (b) Mono-selenium vacancy (MSeV), (c) Di-selenium vacancy (DiSeV), (d) Double mono-selenium vacancy (DMSeV). The purple and green spheres represent molybdenum and selenium atoms, respectively.

Figure 8.2(a) shows the temperature-dependent thermal conductivity of pristine and defective monolayer $MoSe_2$ with three types of Se vacancies. The calculations are based on the sample size of 2 μm. Results indicate that MSeV, DiSeV and DMSeV decrease the thermal conductivity of monolayer $MoSe_2$ by 41.3%, 50.5% and 55.2%, respectively at room temperature. The difference between three types of Se vacancies decreases as temperature increase due to the dominant contribution of the three-phonon process compared to the defect-induced phonon scattering at high temperature.

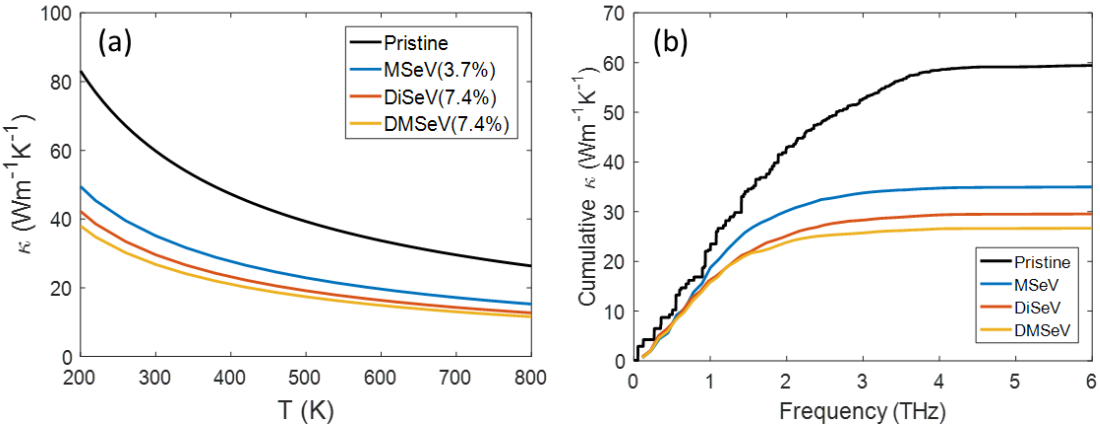

Figure 8.2 (a) Temperature-dependent thermal conductivity of pristine and defective monolayer $MoSe_2$ with three types of Se vacancies. (b) Frequency-dependent thermal conductivity of pristine defective monolayer $MoSe_2$ with three types of Se vacancies at 300K.

To better understand the thermal conductivity difference between the defective $MoSe_2$ and the pristine $MoSe_2$, the frequency-dependent thermal conductivities at room temperature are calculated in Figure 8.2(b). Compared to the pristine $MoSe_2$, the thermal conductivity of three defective $MoSe_2$ is dominantly contributed by the phonons with lower frequencies. For example, for the pristine monolayer $MoSe_2$, 90% of the heat is carried by the phonon lower than 3.2THz. While, for the MSeV, DiSeV and DMSeV, they are reduced to 2.28THz, 2.33THz and 2.08THz, respectively. More detailed explanations are in the next section.

8.3 Phonon properties of Defective Monolayer $MoSe_2$ with Three Types of Se Vacancies

To further understand the influence of defects, the phonon dispersions and DOSs of pristine and defective monolayer $MoSe_2$ with three types of Se vacancies are calculated and presented in Figure 8.3 and Figure 8.4, respectively. As expected, all the phonon

branches of defective $MoSe_2$ are lower in frequency than that of pristine $MoSe_2$. It can be explained by the missing mass of the Se vacancies which results in the increase of the unit cell's average mass. The heavier unit cell of the defective $MoSe_2$ softens the phonon modes, especially the low-frequency modes. It can also be observed by the phonon DOSs in Figure 8.4. The existing Se vacancies redistribute the phonon DOSs by lowering the frequency cutoff and generating defect-induced phonon states. The new generated peaks in DOSs resulting from the defect-induced phonon states lead to a lower phonon group velocity at the certain frequency in Figure 8.7(a). It is also consistent with the observation of the flattened low-frequency braches in the dispersion relations.

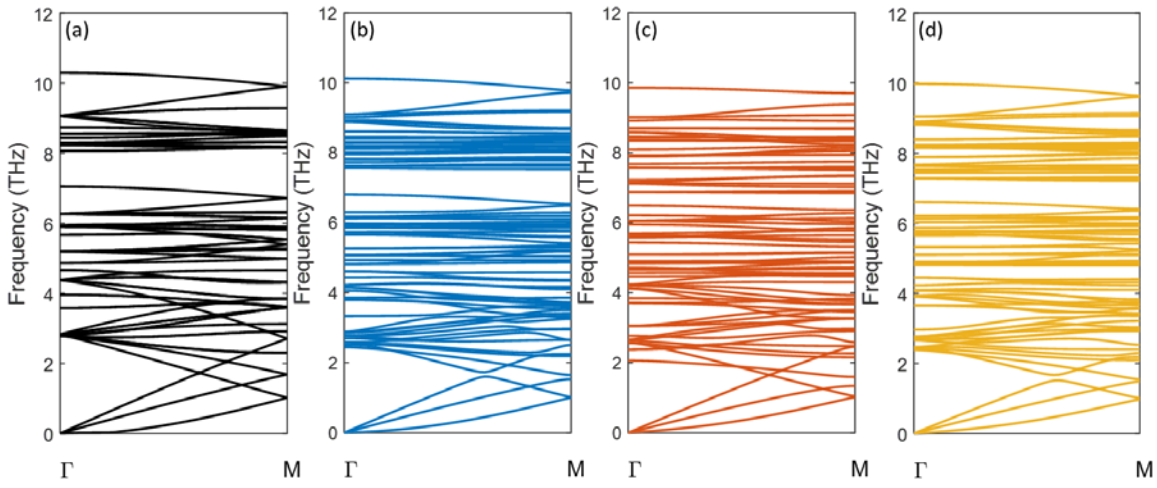

Figure 8.3 Phonon dispersions of (a) pristine monolayer $MoSe_2$, (b) MSeV, (c) DiSeV (d) DMSeV, along $\Gamma - M$ direction.

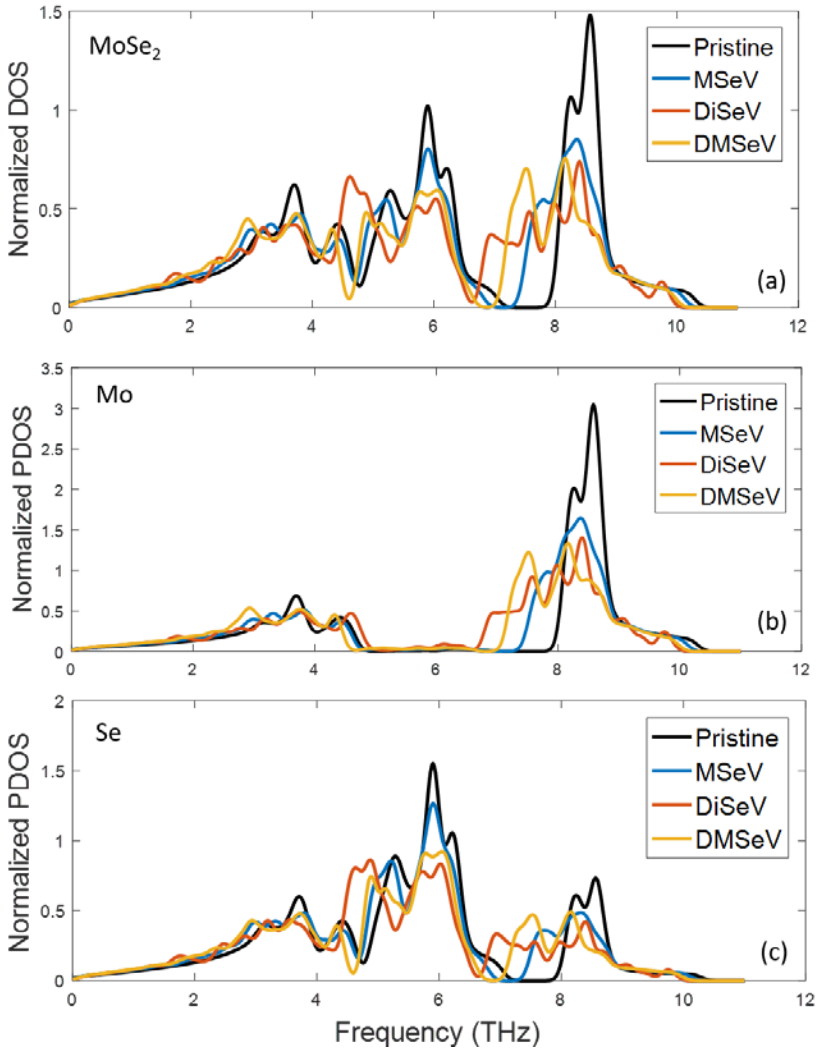

Figure 8.4 (a) Phonon DOSs of pristine and defective monolayer $MoSe_2$. (b) Phonon partial DOSs of Mo atom in pristine and defective monolayer $MoSe_2$. (c) Phonon partial DOSs of Se atom in pristine and defective monolayer $MoSe_2$.

Furthermore, it can also be supported by the three-phonon scattering phase space in Figure 8.5(a) which indicates the volume of phase space available for three-phonon scattering. The details of calculation can be found in Chapter 7. Results indicate that the three-phonon scattering phase space of the defective monolayer $MoSe_2$ is larger than that of the pristine $MoSe_2$ between 0-3THz, which means that the phonons in defective $MoSe_2$ will have more channels for three-phonon scatterings. In addition, the Grüneisen parameter

is calculated to characterize the strength of phonon anharmonicity of each scattering channel in Figure 8.5(b). Results indicate that the defective $MoSe_2$ has a slightly larger Grüneisen parameter at the low-frequency range, which means it has stronger phonon scatterings of each scattering channel. As a result of the combined effects from larger scattering phase space and higher Grüneisen parameter, the defective monolayer $MoSe_2$ results in the stronger anharmonic phonon scattering rate at low-frequency range (Figure 8.6) and smaller thermal conductivity.

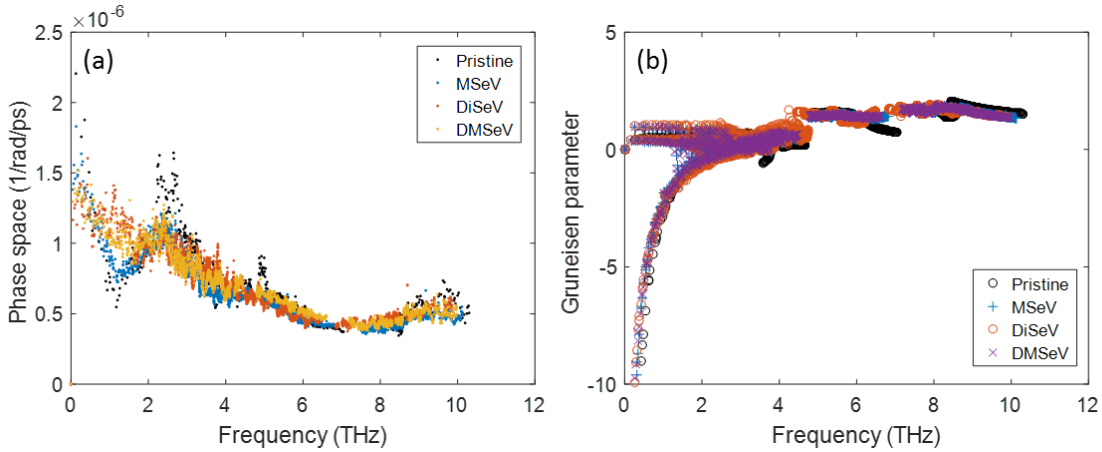

Figure 8.5 (a) Three-phonon scattering phase space and (b) Grüneisen parameter of pristine and defective monolayer $MoSe_2$.

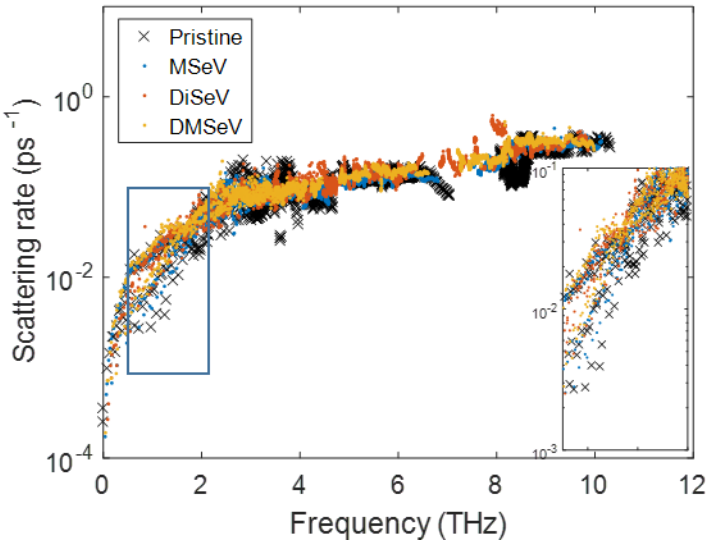

Figure 8.6 Anharmonic phonon scattering rates of pristine and defective monolayer $MoSe_2$.

8.4 Effects of Types of Se Vacancies

What happens to the thermal conductivity of the defective $MoSe_2$ if the type of the Se vacancies is different? In order to investigate the impact of the locations of Se vacancies on the thermal conductivity of the defective $MoSe_2$, the phonon properties of DiSeV and DMSeV are compared, which have the same Se vacancy concentration (7.4%). We find that the existence of di-Se vacancies and double mono-Se vacancies have a significant but slightly different impact on the phonon DOSs redistribution of not only Se atoms but also Mo atoms shown in Figure 8.4(b-c). Due to the difference of DOSs' redistribution caused by di-Se vacancies and double mono-Se vacancies, DMSeV presents lower group velocities especially at low frequency (0-3THz) as shown in Figure 8.7(b), which results in a lower thermal conductivity compared to DiSeV. The DMSeV further flattens the low frequency branches in the dispersion than that of DiSeV, which is caused by the different defect-induced phonon states (small peaks in DOSs) of these two types of defects. We also

observe that these two types of defects also have the influence on the redistribution of the DOSs of optical modes, which can be observed in new peaks generation and mismatch, especially at 4.6 THz and 7.5 THz. It may not have much effect on the thermal conductivity due to the low contribution of optical modes to thermal conductivity. However, it may still influence the optical properties of the defective $MoSe_2$.

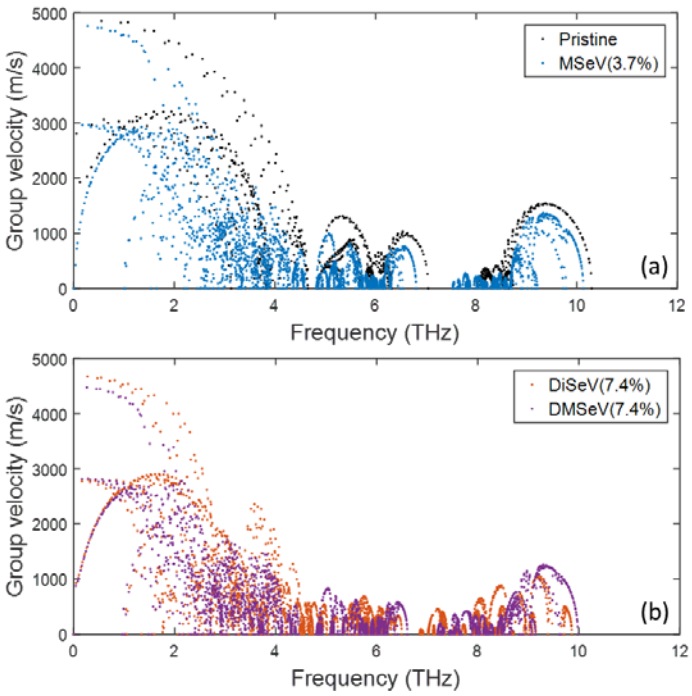

Figure 8.7 Phonon group velocities of (a) pristine monolayer $MoSe_2$ and MSeV, (b) DiSeV and DMSeV.

8.4 Empirical Defect Model

We compare the thermal conductivity of defective $MoSe_2$ from the DFT simulations (parameter-free) to the one obtained from the empirical formula (Figure 8.8). The empirical defect model for estimating the effect of Se vacancies on thermal conductivity of the monolayer $MoSe_2$ is developed by considering contributions of two

different types of the defect-induced phonon scatterings: one caused by the missing mass of the Se atoms, and the other caused by the change of force constants between the under-coordinated atoms near the vacancies. Following our previous study [119], empirical defect model consider the effects of Se vacancies in the monolayer $MoSe_2$ on the phonon scattering rate by adding two different types of the defect-induced phonon scattering to the total phonon scattering rate as shown in Eq. (7-3).

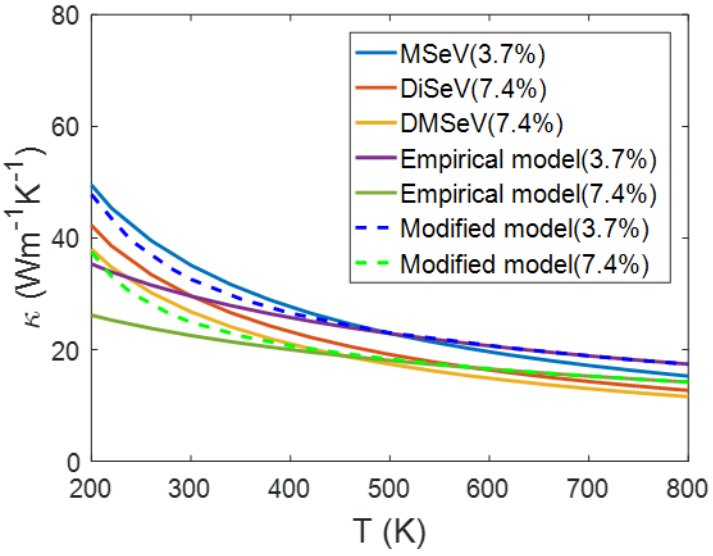

Figure 8.8 Temperature-dependent thermal conductivity of defective monolayer $MoSe_2$ calculated by the DFT simulation, empirical model and the modified empirical model.

Figure 8.8 shows that the empirical defect model (Eqs. (7-3,4,5)) overestimates the influence of point vacancy at the low temperature (T<500K), which results in a much lower thermal conductivity of defective $MoSe_2$ compared to the results from DFT calculation. One reason could be the defect-induced phonon scattering rates described by the empirical model are independent of temperature, which may overestimate the phonon scattering rate at low temperature. In other words, the strength of the frequency dependent defect-induced phonon scattering of the empirical model is constant at different temperatures which may

not true in reality. However, modifying the parameters of the empirical equation cannot change the fact that it is temperature independent. This way can only shift the curve in Figure 8.8 but can't change the slope of it. A temperature dependent term must be introduced to the equation to consider the fact that defect-induced phonon scatterings decrease as the temperature decreases, especially at low temperature. In this study, we attempt to modify the empirical model by introducing term of the normalized specific heat, which decreases as the temperature decreases. A form of $(\frac{Cv(T)}{Cv0})^{(\frac{A}{T})}$ is used in the empirical model as multiplication to the defect-induced phonon scatterings (Eqs. (7-4,5)). $\frac{Cv(T)}{Cv0}$ is the normalized specific heat. A is the constant showing the cutoff temperature (1000K is used in this study). The improvement can be found in Figure 8.8, which indicate a much better match with the DFT results. Although the modified equation is not strictly proved, the result provides insight and direction for future improvement.

8.5 Closure

In summary, this study investigates the thermal transport properties of pristine and defective monolayer $MoSe_2$ by the first principles calculation and the phonon Boltzmann transport equation, which is fully parameter free. Results indicate that MSeV, DiSeV and DMSeV decrease the thermal conductivity of monolayer $MoSe_2$ by 41.3%, 50.5% and 55.2%, respectively at room temperature. The existing Se vacancies redistribute the phonon DOSs by lowering the frequency cutoff and generating defect-induced phonon states, which soften the phonon modes in the dispersion relations and result in a lower phonon group velocity. Furthermore, it's found that the empirical defect model overestimates the

influence of point vacancy at low temperature. The temperature dependent term, which is based on the normalized specific heat, is introduced to the defect-induced scattering rates to improve the reliability of the empirical defect model. This work provides insights and directions to estimate the material properties considering the influence of defects, which could be used for the future design of $MoSe_2$-based electronics.

CHAPTER 9 : SUMMARY AND FUTURE WORK

9.1 Summary of Current Work

In this work, the thermal transport properties of nano-electronic semiconducting materials considering the influence of interfaces, boundaries, and defects has been studied using multiple atomistic simulation techniques including first-principles DFT calculations, AGF and BTE simulations. The research in this work focuses on the nano-electronic semiconducting materials: graphene, 2D transition metal dichalcogenides and β-Ga_2O_3. The present work is summarized below.

(1) An atomistic framework based on DFT and atomistic Green's function has been developed to investigate the impact of different lattice stacking configurations on the thermal transport across the h-BN/graphene/h-BN interfaces. The h-BN substrates soften the TO and LO modes of graphene because of the overlap of orbitals and introduces an asymmetry between carbon atoms in graphene's unit cell leading to gap of different magnitude between the TA and ZA modes in different stacking configurations. Results indicate that the in-plane acoustic modes have the dominant contributions to the TBC for interfaces with the carbon atom located directly on top of the boron atom (C-B matched) compared to the C-N matched interfaces where the carbon atom is located directly on top of the nitrogen atom, because of the low interfacial gap, but their contribution reduces as the interfacial separation distance increases. The C-B matched interfaces have stronger phonon-phonon coupling than the C-N matched interfaces, even though C-N atoms have more intense force interactions. The analysis suggests that the TBC can be enhanced by more than 50% by changing the lattice stacking arrangements from C-N matched to C-B

matched. The findings in this study will provide insights to better understand the experimental measurements on TBC and the mechanism of phonon transport at h-BN/graphene/h-BN interfaces.

(2) The role of interfacial electronic properties on the phonon transport at the interface of monolayer MoS_2 and metal substrates are investigated by DFT and AGF methods. Different degree of orbital hybridization caused by the introduction of a metal substrate affects the interfacial phonon-phonon coupling and phonon transmission significantly. Strong chemical coupling between MoS_2 and the Sc substrate leads to a 19 times higher TBC than that of the weakly bound MoS_2/Au system. For MoS_2 on the Sc substrates, a strong charge transfer from Sc to MoS_2 can be demonstrated by the significant portion of the previous conduction band states occupied below Fermi level. Furthermore, the effect of interfacial lattice-stacking configurations of MoS_2/Sc leads to a significant redistribution of phonon DOSs and transmission at the interface. The extra charge transfer further weakens the Mo-S bond strength in lattice-stacking configuration of structure AB compared to structure AA(Mo). The resultant decrease in the force constant between Mo and S atoms keeps more phonons located in a low-frequency region which results in a 60 % decrease in TBC. The findings in this study demonstrate the inherent connection among the interfacial electronic structure, the phonon distribution, and TBC.

(3) The thermal conductivity and phonon mode contributions of pristine and defective β-Ga_2O_3 are investigated by the DFT and the phonon BTE simulations. The model for estimating the effect of point vacancies on phonon properties is developed by considering contributions of the defect-induced phonon scatterings. For the pristine β-

Ga_2O_3, the thermal conductivity of 12.73 W/mK, 20.00 W/mK, 17.80 W/mK in the direction of [100], [010], [001], are reported respectively, which have a better agreement with the experimental results than the previous study. For the defective β-Ga_2O_3 with oxygen vacancies, 1% and 2% oxygen vacancies decrease the thermal conductivity by 8.5% and 14.3% in [100] direction, 14.9% and 24.1% in [010] direction, 10.7% and 17.4% in [001] direction, respectively at the room temperature. 1% and 2% Ga vacancies decrease the thermal conductivity by 16.6% and 25.3% in [100] direction, 27.6% and 39.4% in [010] direction, 20.4% and 29.9% in [001] direction, respectively due to the larger defect-induced phonon scatterings. Furthermore, the optical phonon modes make a significant contribution to the thermal conductivity compared to the acoustic modes, especially in the [010] direction because of the non-negligible group velocities at optical branches and the hybridization between the low energy optical modes and LA modes. The point vacancies have more influence on the optical modes than that on acoustic modes, leading to a significant suppression in the contribution of optical modes to the thermal conductivity.

(4) The role of size, defects and W doping on thermal conductivity of monolayer $MoSe_2$ is investigated by the first-principles DFT and BTE calculations. An empirical model is developed for estimating the effect of Se vacancies on phonon properties of the monolayer $MoSe_2$ by considering contributions of two different types of the defect-induced phonon scatterings: one caused by the missing mass of the Se atoms, and the other caused by the change of force constants between the under-coordinated atoms near the vacancies. Results indicate that 1%, 2% and 4% Se vacancies decrease the thermal conductivity of monolayer $MoSe_2$ of size 2μm by 27.7%, 39.5% and 51.9%, respectively at the room temperature.

However, we found that for samples without Se vacancy, the W doping could enhance the thermal transport of monolayer $MoSe_2$, which is just opposed to what is typically observed after doping. This was a consequence of reduced three-phonon scattering phase space and the larger gap between the optical and acoustic phonon branches in WSe_2 than that in $MoSe_2$. However, the W doping in the defective $MoSe_2$ amplifies the influence of the phonon scattering caused by the Se vacancies, which results in significant decrease in thermal conductivity compared to $MoSe_2$ with Se vacancies. The results from this work will help to understand the phonon transport properties of monolayer $MoSe_2$ under the influence of defects and doping, and provide insights for the future design of $MoSe_2$-based electronics.

(5) The thermal transport properties of pristine and defective monolayer $MoSe_2$ are investigated by the fully parameter-free first principles DFT and the phonon BTE calculations. The effect of three types of Se vacancies: mono-selenium vacancy, Di-selenium vacancy, double mono-selenium vacancy is studied. The existing Se vacancies redistribute the phonon DOSs by lowering the frequency cutoff and generating defect-induced phonon states, which soften the phonon modes and result in a lower phonon group velocity as observed in the dispersion relations. Furthermore, we found that the empirical defect model overestimates the influence of point vacancy at low temperature compared to the parameter-free DFT simulation. The temperature dependent term, which is based on the normalized specific heat, is introduced to the defect-induced scattering rates to improve the reliability of the empirical defect model. This work provides insights and directions to develop reliable empirical models for estimating the thermal properties considering the influence of defects, which could be used for the future design of $MoSe_2$-based electronics.

9.2 Suggestions for Future Work

The work in present thesis can be extended and continued in several topics as suggested below.

9.2.1 Anharmonicity in Green's Function Method

The harmonic assumption is employed for the AGF methods used in Chapter 4 and Chapter 5. This assumption is valid in present work because the interface scattering due to phonon mismatch dominates the phonon transport of present work at relatively low temperature. A main drawback of the harmonic AGF method is that it has not included the anharmonicity. That could be a serious limitation especially at high temperature. Because anharmonicity is a ubiquitous source of phonon scattering in any solid, and it is very important to quantify its effect.[235] Inclusion of the inelastic phonon scattering can also extend the modeling capability of Green's function method to thermal transport problems where phonon-phonon scattering cannot be neglected. Although classical MD method can easily add the anharmonicity to the system, they are strictly valid only in the higher temperature regimes and can't capture the quantum mechanical aspects of the phonon transport problem. Therefore, both for fundamental, as well as applied reasons, AGF along with DFT method including the anharmonicity of the system become more and more important to capture the thermal transport process. Furthermore, including the anharmonicity in the AGF could provide a powerful tool to study the phonon transport process at the interfaces with defects. The validation of AGF simulation results against the experimental measurements is important to better understand the temperature limitation of

using harmonic assumption and the importance of including the anharmonicity for different types of interfaces. To perform such comparison, the sample with a clean interface is necessary to be prepared. Residue, for example, contaminants from tape/polymer during transfer of 2D materials or surface oxidation due to exposure to moisture in air can have significant impact on the measurements of interfacial thermal conductance and such effects need to be reduced. The lattice stacking configurations also have significant influence on the thermal measurement results, influence of which need to be considered and characterized by techniques such as STM or STEM.

9.2.2 Machine Learning Method for Predicting Thermal Properties

According to our presented work, the second and third IFCs from first-principles DFT calculation are the musts for estimating thermal conductivity and simulating the resistive thermal transport process. The calculation process obtaining the second and third IFCs based on the perturbation theory require repeatedly calculating the energy of a crystal or nanostructures with more atoms displaced from their equilibrium position. As a result, the computational cost is very high for large systems. Sometimes, it's impossible to calculate the huge system with low concentration of defects and low symmetry, which may require evaluating tons of atomic displacements.

Recently, machine learning techniques applied to *ab initio* calculations have been proposed as an efficient approach for describing the energies of crystals and molecules in their given ground-state structure.[236, 237] Gaussian process regression (GPR), Bayesian linear regression (BLR), and support vector machine (SVM) regression models are evaluated on their prediction accuracy and convergence rate with respect to training set

size. In addition, the machine learning techniques can also predict the thermal properties directly without performing exhaustive DFT calculations. [238-240]

Therefore, applying the machine learning techniques to the field of thermal transport is of significant importance for solving the complicated structures, such as defective interfaces, noncrystalline or molecular compounds with defects.

9.2.3 Electron Contribution to Thermal Transport

The phonon contribution to the thermal conductivity of the semiconducting materials has a complex dependence on temperature, lattice anharmonicity, and the strength of electron-phonon coupling [1–3]. The scattering of phonons by electrons is typically less important. The high-temperature lattice thermal conductivities with relatively weak electron-phonon coupling are typically in good agreement with the assumption of lattice thermal conductivity limited by anharmonicity [3]. However, for the materials with low anharmonic phonon scattering rates and strong electron-phonon coupling strength, electron contribution plays a significant role to the thermal transport process, such as at metal electrode interfaces and in metallic transition-metal (TM) nitrides and carbides.[241-244] In addition, the electron-phonon coupling becomes very important considering the thermal transport in transistors with a high electrical field. The validation of the electron contributions to interfacial thermal transport predicted by the simulations against the experimental measurements is also necessary to understand the importance of the electron contribution especially for the materials with strong electron-phonon coupling strength, such as graphene, metallic materials, superconductors, magnetic materials. Therefore, performing the study of the electron contribution to thermal transport by considering

electron transport and electron-phonon coupling will extend our current model applications to the nano-electronic devices for high-field high-power applications.

REFERENCES

1. Enoki, T., M. Suzuki, and M. Endo, *Graphite intercalation compounds and applications*. 2003: Oxford University Press.
2. Delhaes, P., *Graphite and precursors*. 2014: CRC Press.
3. Bourzac, K., *ELECTRONICS Back to analogue.* Nature, 2012. **483**(7389): p. S34-S36.
4. Balandin, A.A., *Thermal properties of graphene and nanostructured carbon materials.* Nat Mater, 2011. **10**(8): p. 569-581.
5. Schwierz, F., *Graphene transistors.* Nat Nano, 2010. **5**(7): p. 487-496.
6. Gu, X. and R. Yang, *First-principles prediction of phononic thermal conductivity of silicene: A comparison with graphene.* Journal of Applied Physics, 2015. **117**(2): p. 025102.
7. Li, X.L., et al., *Chemically derived, ultrasmooth graphene nanoribbon semiconductors.* Science, 2008. **319**(5867): p. 1229-1232.
8. Wang, X., L.J. Zhi, and K. Mullen, *Transparent, conductive graphene electrodes for dye-sensitized solar cells.* Nano Letters, 2008. **8**(1): p. 323-327.
9. Bai, J.W., et al., *Graphene nanomesh.* Nature Nanotechnology, 2010. **5**(3): p. 190-194.
10. Lin, Y.M., et al., *Operation of Graphene Transistors at Gigahertz Frequencies.* Nano Letters, 2009. **9**(1): p. 422-426.
11. Kawano, Y., *Wide-band frequency-tunable terahertz and infrared detection with graphene.* Nanotechnology, 2013. **24**(21): p. 214004.
12. Thiele, S. and F. Schwierz, *Modeling of the steady state characteristics of large-area graphene field-effect transistors.* Journal of Applied Physics, 2011. **110**(3): p. 034506.
13. Wang, Y., et al., *Large area, continuous, few-layered graphene as anodes in organic photovoltaic devices.* Applied Physics Letters, 2009. **95**(6): p. 209.
14. Wang, X., L. Zhi, and K. Müllen, *Transparent, conductive graphene electrodes for dye-sensitized solar cells.* Nano letters, 2008. **8**(1): p. 323-327.
15. Mattevi, C., et al., *Solution-processable organic dielectrics for graphene electronics.* Nanotechnology, 2012. **23**(34): p. 344017.
16. Kim, K.S., et al., *Large-scale pattern growth of graphene films for stretchable transparent electrodes.* nature, 2009. **457**(7230): p. 706.
17. Edwards, R.S. and K.S. Coleman, *Graphene synthesis: relationship to applications.* Nanoscale, 2013. **5**(1): p. 38-51.
18. Brownson, D.A., D.K. Kampouris, and C.E. Banks, *An overview of graphene in energy production and storage applications.* Journal of Power Sources, 2011. **196**(11): p. 4873-4885.
19. Lee, J.K., et al., *Silicon nanoparticles–graphene paper composites for Li ion battery anodes.* Chemical Communications, 2010. **46**(12): p. 2025-2027.
20. David, L., et al., *Silicon oxycarbide glass-graphene composite paper electrode for long-cycle lithium-ion batteries.* Nature communications, 2016. **7**: p. 10998.

21. Peng, Z., et al., *Flexible boron-doped laser-induced graphene microsupercapacitors.* ACS nano, 2015. **9**(6): p. 5868-5875.
22. Yan, J., et al., *Preparation of a graphene nanosheet/polyaniline composite with high specific capacitance.* Carbon, 2010. **48**(2): p. 487-493.
23. Vivekchand, S., et al., *Graphene-based electrochemical supercapacitors.* Journal of Chemical Sciences, 2008. **120**(1): p. 9-13.
24. Pan, D., et al., *Li storage properties of disordered graphene nanosheets.* Chemistry of Materials, 2009. **21**(14): p. 3136-3142.
25. Wu, Z.-S., et al., *Doped graphene sheets as anode materials with superhigh rate and large capacity for lithium ion batteries.* ACS nano, 2011. **5**(7): p. 5463-5471.
26. Reddy, A.L.M., et al., *Synthesis of nitrogen-doped graphene films for lithium battery application.* ACS nano, 2010. **4**(11): p. 6337-6342.
27. Shao, Y., et al., *Nitrogen-doped graphene and its electrochemical applications.* Journal of Materials Chemistry, 2010. **20**(35): p. 7491-7496.
28. Tadjer, M.J., et al., *Structural, Optical, and Electrical Characterization of Monoclinic β-Ga 2 O 3 Grown by MOVPE on Sapphire Substrates.* Journal of Electronic Materials, 2016. **45**(4): p. 2031-2037.
29. Pearton, S., et al., *A review of Ga2O3 materials, processing, and devices.* Applied Physics Reviews, 2018. **5**(1): p. 011301.
30. Ueda, N., et al., *Anisotropy of electrical and optical properties in β-Ga 2 O 3 single crystals.* Applied physics letters, 1997. **71**(7): p. 933-935.
31. Schubert, M., et al., *Anisotropy, phonon modes, and free charge carrier parameters in monoclinic β-gallium oxide single crystals.* Physical Review B, 2016. **93**(12): p. 125209.
32. Slomski, M., et al., *Anisotropic thermal conductivity of β-Ga2O3 at elevated temperatures: Effect of Sn and Fe dopants.* Journal of Applied Physics, 2017. **121**(23): p. 235104.
33. Ueda, O., et al., *Structural evaluation of defects in β-Ga2O3 single crystals grown by edge-defined film-fed growth process.* Japanese Journal of Applied Physics, 2016. **55**(12): p. 1202BD.
34. Mang, A. and K. Reimann, *Band gaps, crystal-field splitting, spin-orbit coupling, and exciton binding energies in ZnO under hydrostatic pressure.* Solid state communications, 1995. **94**(4): p. 251-254.
35. Sasaki, K., et al., *Device-quality β-Ga2O3 epitaxial films fabricated by ozone molecular beam epitaxy.* Applied Physics Express, 2012. **5**(3): p. 035502.
36. Sasaki, K., et al., *MBE grown Ga2O3 and its power device applications.* Journal of Crystal Growth, 2013. **378**: p. 591-595.
37. Higashiwaki, M., et al., *Gallium oxide (Ga2O3) metal-semiconductor field-effect transistors on single-crystal β-Ga2O3 (010) substrates.* Applied Physics Letters, 2012. **100**(1): p. 013504.
38. Oh, S., et al., *Solar-Blind Metal-Semiconductor-Metal Photodetectors Based on an Exfoliated β-Ga2O3 Micro-Flake.* ECS Journal of Solid State Science and Technology, 2017. **6**(8): p. Q79-Q83.
39. Yang, J., et al., *High Breakdown Voltage (− 201) $\beta $-Ga2O3 Schottky Rectifiers.* IEEE Electron Device Letters, 2017. **38**(7): p. 906-909.

40. Nakagomi, S., T. Sai, and Y. Kokubun, *Hydrogen gas sensor with self temperature compensation based on β-Ga2O3 thin film.* Sensors and Actuators B: Chemical, 2013. **187**: p. 413-419.
41. Krishnamoorthy, S., et al., *Modulation-doped β-(Al0. 2Ga0. 8) 2O3/Ga2O3 field-effect transistor.* Applied Physics Letters, 2017. **111**(2): p. 023502.
42. Zhou, H., et al., *High-Performance Depletion/Enhancement-ode $\beta $-Ga2O3 on Insulator (GOOI) Field-Effect Transistors With Record Drain Currents of 600/450 mA/mm.* IEEE Electron Device Letters, 2017. **38**(1): p. 103-106.
43. Tadjer, M.J., et al., *Editors' Choice Communication—A (001) β-Ga2O3 MOSFET with+ 2.9 V Threshold Voltage and HfO2 Gate Dielectric.* ECS Journal of Solid State Science and Technology, 2016. **5**(9): p. P468-P470.
44. Zhou, H., et al., *High-performance depletion/enhancement-mode β-Ga2O3 on insulator (GOOI) field-effect transistors with record drain currents of 600/450 mA/mm.* IEEE Electron Device Lett, 2017. **38**(1): p. 103-106.
45. Mak, K.F., et al., *Atomically Thin ${\mathrm{MoS}}_{2}$: A New Direct-Gap Semiconductor.* Physical Review Letters, 2010. **105**(13): p. 136805.
46. Han, S.W., et al., *Band-gap transition induced by interlayer van der Waals interaction in MoS${}_{2}$.* Physical Review B, 2011. **84**(4): p. 045409.
47. Li, Y., et al., *MoS2 nanoribbons: high stability and unusual electronic and magnetic properties.* Journal of the American Chemical Society, 2008. **130**(49): p. 16739-16744.
48. Huang, Y.L., et al., *Bandgap tunability at single-layer molybdenum disulphide grain boundaries.* Nature communications, 2015. **6**.
49. Zheng, C., et al., *Profound effect of substrate hydroxylation and hydration on electronic and optical properties of monolayer MoS2.* Nano letters, 2015. **15**(5): p. 3096-3102.
50. Zeng, H., et al., *Valley polarization in MoS2 monolayers by optical pumping.* Nature nanotechnology, 2012. **7**(8): p. 490-493.
51. Mak, K.F., et al., *Control of valley polarization in monolayer MoS2 by optical helicity.* Nature nanotechnology, 2012. **7**(8): p. 494-498.
52. Splendiani, A., et al., *Emerging photoluminescence in monolayer MoS2.* Nano letters, 2010. **10**(4): p. 1271-1275.
53. Das, S., et al., *High performance multilayer MoS2 transistors with scandium contacts.* Nano letters, 2012. **13**(1): p. 100-105.
54. Qiu, H., et al., *Electrical characterization of back-gated bi-layer MoS2 field-effect transistors and the effect of ambient on their performances.* Applied Physics Letters, 2012. **100**(12): p. 123104.
55. Fortin, E. and W. Sears, *Photovoltaic effect and optical absorption in MoS2.* Journal of Physics and Chemistry of Solids, 1982. **43**(9): p. 881-884.
56. Novoselov, K., et al., *Two-dimensional atomic crystals.* Proceedings of the National Academy of Sciences of the United States of America, 2005. **102**(30): p. 10451-10453.
57. Lynch, R.W. and H.G. Drickamer, *Effect of High Pressure on the Lattice Parameters of Diamond, Graphite, and Hexagonal Boron Nitride.* The Journal of Chemical Physics, 1966. **44**(1): p. 181-184.

58. Radisavljevic, B., et al., *Single-layer MoS2 transistors.* Nature nanotechnology, 2011. **6**(3): p. 147-150.
59. Radisavljevic, B., et al., *Single-layer MoS 2 transistors.* Nature nanotechnology, 2011. **6**(3): p. 147.
60. Zhang, Y., et al., *Direct observation of the transition from indirect to direct bandgap in atomically thin epitaxial MoSe2.* Nature nanotechnology, 2014. **9**(2): p. 111-115.
61. Tongay, S., et al., *Thermally driven crossover from indirect toward direct bandgap in 2D semiconductors: MoSe2 versus MoS2.* Nano letters, 2012. **12**(11): p. 5576-5580.
62. Late, D.J., et al., *Thermal Expansion, Anharmonicity and Temperature‐Dependent Raman Spectra of Single‐and Few‐Layer MoSe2 and WSe2.* ChemPhysChem, 2014. **15**(8): p. 1592-1598.
63. Horzum, S., et al., *Phonon softening and direct to indirect band gap crossover in strained single-layer MoSe 2.* Physical Review B, 2013. **87**(12): p. 125415.
64. Onga, M., et al., *High circular polarization in electroluminescence from MoSe2.* Applied Physics Letters, 2016. **108**(7): p. 073107.
65. Chang, Y.-H., et al., *Monolayer MoSe2 grown by chemical vapor deposition for fast photodetection.* ACS nano, 2014. **8**(8): p. 8582-8590.
66. Bernardi, M., M. Palummo, and J.C. Grossman, *Extraordinary sunlight absorption and one nanometer thick photovoltaics using two-dimensional monolayer materials.* Nano letters, 2013. **13**(8): p. 3664-3670.
67. Larentis, S., B. Fallahazad, and E. Tutuc, *Field-effect transistors and intrinsic mobility in ultra-thin MoSe2 layers.* Applied Physics Letters, 2012. **101**(22): p. 223104.
68. Kumar, S. and U. Schwingenschlogl, *Thermoelectric response of bulk and monolayer MoSe2 and WSe2.* Chemistry of Materials, 2015. **27**(4): p. 1278-1284.
69. Shafique, A. and Y.-H. Shin, *Thermoelectric and phonon transport properties of two-dimensional IV–VI compounds.* Scientific Reports, 2017. **7**(1): p. 506.
70. Quereda, J., et al., *Observation of bright and dark exciton transitions in monolayer MoSe2 by photocurrent spectroscopy.* 2D Materials, 2017. **5**(1): p. 015004.
71. Ataca, C., H. Sahin, and S. Ciraci, *Stable, single-layer MX2 transition-metal oxides and dichalcogenides in a honeycomb-like structure.* The Journal of Physical Chemistry C, 2012. **116**(16): p. 8983-8999.
72. Lee, Y.-H., et al., *Synthesis and transfer of single-layer transition metal disulfides on diverse surfaces.* Nano letters, 2013. **13**(4): p. 1852-1857.
73. Tonndorf, P., et al., *Photoluminescence emission and Raman response of monolayer MoS 2, MoSe 2, and WSe 2.* Optics express, 2013. **21**(4): p. 4908-4916.
74. Chhowalla, M., et al., *The chemistry of two-dimensional layered transition metal dichalcogenide nanosheets.* Nature chemistry, 2013. **5**(4): p. 263-275.
75. Wang, Q.H., et al., *Electronics and optoelectronics of two-dimensional transition metal dichalcogenides.* Nature nanotechnology, 2012. **7**(11): p. 699-712.
76. Yan, Z., et al., *The Role of Interfacial Electronic Properties on Phonon Transport in Two-Dimensional MoS2 on Metal Substrates.* ACS applied materials & interfaces, 2016. **8**(48): p. 33299-33306.

77. Dean, C.R., et al., *Boron nitride substrates for high-quality graphene electronics.* Nat Nano, 2010. **5**(10): p. 722-726.
78. Geim, A.K. and K.S. Novoselov, *The rise of graphene.* Nat Mater, 2007. **6**(3): p. 183-191.
79. Kaloni, T.P., Y.C. Cheng, and U. Schwingenschlogl, *Electronic structure of superlattices of graphene and hexagonal boron nitride.* Journal of Materials Chemistry, 2012. **22**(3): p. 919-922.
80. Freitag, M., et al., *Energy Dissipation in Graphene Field-Effect Transistors.* Nano Letters, 2009. **9**(5): p. 1883-1888.
81. Chen, C.-C., et al., *Thermal interface conductance across a graphene/hexagonal boron nitride heterojunction.* Applied Physics Letters, 2014. **104**(8): p. -.
82. Mao, R., et al., *Phonon engineering in nanostructures: Controlling interfacial thermal resistance in multilayer-graphene/dielectric heterojunctions.* Applied Physics Letters, 2012. **101**(11): p. 113111.
83. Xue, J.M., et al., *Scanning tunnelling microscopy and spectroscopy of ultra-flat graphene on hexagonal boron nitride.* Nature Materials, 2011. **10**(4): p. 282-285.
84. Sachs, B., et al., *Adhesion and electronic structure of graphene on hexagonal boron nitride substrates.* Physical Review B, 2011. **84**(19): p. 195414.
85. Giovannetti, G., et al., *Substrate-induced band gap in graphene on hexagonal boron nitride: Ab initio density functional calculations.* Physical Review B, 2007. **76**(7).
86. Zhong, X.L., et al., *Electronic structure and quantum transport properties of trilayers formed from graphene and boron nitride.* Nanoscale, 2012. **4**(17): p. 5490-5498.
87. Slawinska, J., et al., *Reversible modifications of linear dispersion: Graphene between boron nitride monolayers.* Physical Review B, 2010. **82**(8).
88. Li, Y.J., et al., *Hexagonal boron nitride intercalated multi-layer graphene: a possible ultimate solution to ultra-scaled interconnect technology.* Aip Advances, 2012. **2**(1).
89. Quhe, R., et al., *Tunable and sizable band gap of single-layer graphene sandwiched between hexagonal boron nitride (vol 4, pg e6, 2012).* Npg Asia Materials, 2012. **4**.
90. Pashangpour, M., Z. Bagheri, and V. Ghaffari, *A comparison of electronic transport properties of graphene with hexagonal boron nitride substrate and graphane, a first principle study.* European Physical Journal B, 2013. **86**(6).
91. Slotman, G.J., et al., *Phonons and electron-phonon coupling in graphene-h-BN heterostructures.* Annalen Der Physik, 2014. **526**(9-10): p. 381-386.
92. Mao, R., B.D. Kong, and K.W. Kim, *Thermal transport properties of metal/MoS2 interfaces from first principles.* Journal of Applied Physics, 2014. **116**(3): p. 034302.
93. Popov, I., G. Seifert, and D. Tománek, *Designing electrical contacts to MoS 2 monolayers: a computational study.* Physical review letters, 2012. **108**(15): p. 156802.
94. Chen, W., et al., *Tuning the electronic and chemical properties of monolayer MoS2 adsorbed on transition metal substrates.* Nano letters, 2013. **13**(2): p. 509-514.

95. Chakraborty, B., et al., *Symmetry-dependent phonon renormalization in monolayer MoS 2 transistor.* Physical Review B, 2012. **85**(16): p. 161403.
96. Koh, Y.K., et al., *Heat conduction across monolayer and few-layer graphenes.* Nano Letters, 2010. **10**(11): p. 4363-4368.
97. Chiloyan, V., et al., *Transition from near-field thermal radiation to phonon heat conduction at sub-nanometre gaps.* Nat Commun, 2015. **6**.
98. Yan, Z., et al., *Phonon Transport at the Interfaces of Vertically Stacked Graphene and Hexagonal Boron Nitride Heterostructures.* Nanoscale, 2016.
99. Tsao, J., et al., *Ultrawide‐Bandgap Semiconductors: Research Opportunities and Challenges.* Advanced Electronic Materials, 2018. **4**(1): p. 1600501.
100. Wu, X., et al., *Thermal conductivity of wurtzite zinc-oxide from first-principles lattice dynamics–a comparative study with gallium nitride.* Scientific reports, 2016. **6**: p. 22504.
101. Lindsay, L., D. Broido, and T. Reinecke, *Thermal conductivity and large isotope effect in GaN from first principles.* Physical review letters, 2012. **109**(9): p. 095901.
102. Mastro, M.A., et al., *Perspective—opportunities and future directions for Ga2O3.* ECS Journal of Solid State Science and Technology, 2017. **6**(5): p. P356-P359.
103. Bayraktaroglu, B., *Assessment of gallium oxide technology*. 2017, Air Force Research Laboratory, Sensors Directorate WPAFB United States.
104. Tadjer, M.J., et al., *Reduced self-heating in AlGaN/GaN HEMTs using nanocrystalline diamond heat-spreading films.* IEEE Electron Device Letters, 2012. **33**(1): p. 23-25.
105. Chao, P.-C., et al., *Low-temperature bonded GaN-on-diamond HEMTs with 11 W/mm output power at 10 GHz.* IEEE Transactions on Electron Devices, 2015. **62**(11): p. 3658-3664.
106. Santia, M.D., N. Tandon, and J. Albrecht, *Lattice thermal conductivity in β-Ga 2 O 3 from first principles.* Applied Physics Letters, 2015. **107**(4): p. 041907.
107. Guo, Z., et al., *Anisotropic thermal conductivity in single crystal β-gallium oxide.* Applied Physics Letters, 2015. **106**(11): p. 111909.
108. Handwerg, M., et al., *Temperature-dependent thermal conductivity in Mg-doped and undoped β-Ga2O3 bulk-crystals.* Semiconductor Science and Technology, 2015. **30**(2): p. 024006.
109. Galazka, Z., et al., *On the bulk β-Ga2O3 single crystals grown by the Czochralski method.* Journal of Crystal Growth, 2014. **404**: p. 184-191.
110. Kananen, B., et al., *Gallium vacancies in β-Ga2O3 crystals.* Applied Physics Letters, 2017. **110**(20): p. 202104.
111. Varley, J., et al., *Oxygen vacancies and donor impurities in β-Ga 2 O 3.* Applied Physics Letters, 2010. **97**(14): p. 142106.
112. Kananen, B., et al., *Electron paramagnetic resonance study of neutral Mg acceptors in β-Ga2O3 crystals.* Applied Physics Letters, 2017. **111**(7): p. 072102.
113. Dong, L., et al., *Effects of oxygen vacancies on the structural and optical properties of β-Ga 2 O 3.* Scientific reports, 2017. **7**: p. 40160.
114. Dong, L., et al., *Ab initio study of N-doped β-Ga2O3 with intrinsic defects: the structural, electronic and optical properties.* Journal of Alloys and Compounds, 2017. **712**: p. 379-385.

115. Chikoidze, E., et al., *P-type β-gallium oxide: A new perspective for power and optoelectronic devices.* Materials Today Physics, 2017. **3**: p. 118-126.
116. Ma, X., et al., *First-principles calculations of electronic and optical properties of aluminum-doped β-Ga2O3 with intrinsic defects.* Results in physics, 2017. **7**: p. 1582-1589.
117. Binet, L. and D. Gourier, *Origin of the blue luminescence of β-Ga2O3.* Journal of Physics and Chemistry of Solids, 1998. **59**(8): p. 1241-1249.
118. Chen, L., et al., *Roles of Point Defects in Thermal Transport in Perovskite Barium Stannate.* The Journal of Physical Chemistry C, 2018. **122**(21): p. 11482-11490.
119. Yan, Z., M. Yoon, and S. Kumar, *Influence of defects and doping on phonon transport properties of monolayer MoSe2.* 2D Materials, 2018. **5**(3): p. 031008.
120. Gu, X. and R. Yang, *Phonon transport in single-layer transition metal dichalcogenides: A first-principles study.* Applied Physics Letters, 2014. **105**(13): p. 131903.
121. Peng, B., et al., *Thermal conductivity of monolayer MoS 2, MoSe 2, and WS 2: interplay of mass effect, interatomic bonding and anharmonicity.* RSC Advances, 2016. **6**(7): p. 5767-5773.
122. Li, W., J. Carrete, and N. Mingo, *Thermal conductivity and phonon linewidths of monolayer MoS2 from first principles.* Applied Physics Letters, 2013. **103**(25): p. 253103.
123. Slack, G.A., *Nonmetallic crystals with high thermal conductivity.* Journal of Physics and Chemistry of Solids, 1973. **34**(2): p. 321-335.
124. Morelli, D. and J. Heremans, *Thermal conductivity of germanium, silicon, and carbon nitrides.* Applied physics letters, 2002. **81**(27): p. 5126-5128.
125. Lin, J., S.T. Pantelides, and W. Zhou, *Vacancy-induced formation and growth of inversion domains in transition-metal dichalcogenide monolayer.* ACS nano, 2015. **9**(5): p. 5189-5197.
126. Zhang, K., et al., *Manganese doping of monolayer MoS2: the substrate is critical.* Nano Lett, 2015. **15**(10): p. 6586-6591.
127. Li, X., et al., *Suppression of defects and deep levels using isoelectronic tungsten substitution in monolayer MoSe2.* Advanced Functional Materials, 2017. **27**(19).
128. Mahjouri-Samani, M., et al., *Tailoring Vacancies Far Beyond Intrinsic Levels Changes the Carrier Type and Optical Response in Monolayer MoSe2− x Crystals.* Nano letters, 2016. **16**(8): p. 5213-5220.
129. Gong, Y., et al., *Band gap engineering and layer-by-layer mapping of selenium-doped molybdenum disulfide.* Nano letters, 2013. **14**(2): p. 442-449.
130. Azizi, A., et al., *Dislocation motion and grain boundary migration in two-dimensional tungsten disulphide.* Nature communications, 2014. **5**: p. 4867.
131. Peng, B., et al., *Beyond Perturbation: Role of Vacancy-Induced Localized Phonon States in Thermal Transport of Monolayer MoS2.* The Journal of Physical Chemistry C, 2016. **120**(51): p. 29324-29331.
132. Ding, Z., et al., *Manipulating the thermal conductivity of monolayer MoS2 via lattice defect and strain engineering.* The Journal of Physical Chemistry C, 2015. **119**(28): p. 16358-16365.

133. Han, H.-V., et al., *Photoluminescence enhancement and structure repairing of monolayer MoSe2 by hydrohalic acid treatment.* ACS nano, 2016. **10**(1): p. 1454-1461.
134. Lin, Z., et al., *Defect engineering of two-dimensional transition metal dichalcogenides.* 2D Materials, 2016. **3**(2): p. 022002.
135. Lin, Z., et al., *2D materials advances: from large scale synthesis and controlled heterostructures to improved characterization techniques, defects and applications.* 2D Materials, 2016. **3**(4): p. 042001.
136. Azizi, A., et al., *Defect Coupling and Sub-Angstrom Structural Distortions in W1–x Mo x S2 Monolayers.* Nano letters, 2017. **17**(5): p. 2802-2808.
137. Li, X., et al., *Persistent photoconductivity in two-dimensional Mo 1− x W x Se 2–MoSe 2 van der Waals heterojunctions.* Journal of Materials Research, 2016. **31**(7): p. 923-930.
138. Mayorov, A.S., et al., *Micrometer-scale ballistic transport in encapsulated graphene at room temperature.* Nano letters, 2011. **11**(6): p. 2396-2399.
139. Lee, K.H., et al., *Large-scale synthesis of high-quality hexagonal boron nitride nanosheets for large-area graphene electronics.* Nano letters, 2012. **12**(2): p. 714-718.
140. Britnell, L., et al., *Field-effect tunneling transistor based on vertical graphene heterostructures.* Science, 2012. **335**(6071): p. 947-950.
141. D'Souza, R. and S. Mukherjee, *Thermoelectric transport in graphene/h-BN/graphene heterostructures: A computational study.* Physica E: Low-dimensional Systems and Nanostructures, 2016. **81**: p. 96-101.
142. Chen, C.-C., et al., *Thermoelectric transport across graphene/hexagonal boron nitride/graphene heterostructures.* Nano Research, 2015. **8**(2): p. 666-672.
143. Zhang, C., et al., *Direct growth of large-area graphene and boron nitride heterostructures by a co-segregation method.* Nature communications, 2015. **6**: p. 6519.
144. Liu, Y., et al., *Thermal conductance of the 2D MoS 2/h-BN and graphene/h-BN interfaces.* Scientific Reports, 2017. **7**: p. 43886.
145. Kim, D., et al., *Energy dissipation mechanism revealed by spatially resolved Raman thermometry of graphene/hexagonal boron nitride heterostructure devices.* 2D Materials, 2018. **5**(2): p. 025009.
146. Cahill, D.G., *Analysis of heat flow in layered structures for time-domain thermoreflectance.* Review of scientific instruments, 2004. **75**(12): p. 5119-5122.
147. Norris, P.M., et al., *Prediction and Measurement of Thermal Transport Across Interfaces Between Isotropic Solids and Graphitic Materials.* Journal of Heat Transfer, 2011. **134**(2): p. 020910-020910.
148. Gengler, J.J., et al., *Limited thermal conductance of metal-carbon interfaces.* Journal of Applied Physics, 2012. **112**(9): p. 094904.
149. Chen, L., Z. Huang, and S. Kumar, *Impact of bonding at multi-layer graphene/metal Interfaces on thermal boundary conductance.* RSC Advances, 2014. **4**(68): p. 35852-35861.
150. Shen, M., P.K. Schelling, and P. Keblinski, *Heat transfer mechanism across few-layer graphene by molecular dynamics.* Physical Review B, 2013. **88**(4): p. 045444.

151. Xue, J., et al., *Scanning tunnelling microscopy and spectroscopy of ultra-flat graphene on hexagonal boron nitride.* Nature materials, 2011. **10**(4): p. 282.
152. Zhang, J., Y. Hong, and Y. Yue, *Thermal transport across graphene and single layer hexagonal boron nitride.* Journal of Applied Physics, 2015. **117**(13): p. 134307.
153. Wang, Q.H., et al., *Electronics and optoelectronics of two-dimensional transition metal dichalcogenides.* Nature nanotechnology, 2012. **7**(11): p. 699.
154. Chhowalla, M., et al., *The chemistry of two-dimensional layered transition metal dichalcogenide nanosheets.* Nature chemistry, 2013. **5**(4): p. 263.
155. Fang, H., et al., *High-performance single layered WSe2 p-FETs with chemically doped contacts.* Nano letters, 2012. **12**(7): p. 3788-3792.
156. Liu, W., et al., *Role of metal contacts in designing high-performance monolayer n-type WSe2 field effect transistors.* Nano letters, 2013. **13**(5): p. 1983-1990.
157. Kappera, R., et al., *Phase-engineered low-resistance contacts for ultrathin MoS 2 transistors.* Nature materials, 2014. **13**(12): p. 1128.
158. Sahoo, S., et al., *Temperature-dependent Raman studies and thermal conductivity of few-layer MoS2.* The Journal of Physical Chemistry C, 2013. **117**(17): p. 9042-9047.
159. Yan, R., et al., *Thermal conductivity of monolayer molybdenum disulfide obtained from temperature-dependent Raman spectroscopy.* ACS nano, 2014. **8**(1): p. 986-993.
160. Zhang, X., et al., *Measurement of lateral and interfacial thermal conductivity of Single-and Bilayer MoS2 and MoSe2 using refined optothermal Raman technique.* ACS applied materials & interfaces, 2015. **7**(46): p. 25923-25929.
161. Taube, A., et al., *Temperature-dependent thermal properties of supported MoS2 monolayers.* ACS applied materials & interfaces, 2015. **7**(9): p. 5061-5065.
162. Hong, Y., J. Zhang, and X.C. Zeng, *Thermal conductivity of monolayer mose2 and mos2.* The Journal of Physical Chemistry C, 2016. **120**(45): p. 26067-26075.
163. Han, H.-V., et al., *Photoluminescence enhancement and structure repairing of monolayer MoSe2 by hydrohalic acid treatment.* 2016.
164. Yarali, M., et al., *Effect of Metal Doping and Vacancies on the Thermal Conductivity of Monolayer Molybdenum Diselenide.* ACS applied materials & interfaces, 2018. **10**(5): p. 4921-4928.
165. Engel, E. and R.M. Dreizler, *Density Functional Theory: An Advanced Course*. 2011: Springer Berlin Heidelberg.
166. Hohenberg, P. and W. Kohn, *Inhomogeneous Electron Gas.* Physical Review B, 1964. **136**(3B): p. B864-&.
167. Sholl, D. and J.A. Steckel, *Density functional theory: a practical introduction*. 2011: John Wiley & Sons.
168. Wirtz, L. and A. Rubio, *The phonon dispersion of graphite revisited.* Solid State Communications, 2004. **131**(3-4): p. 141-152.
169. Alfe, D., *PHON: A program to calculate phonons using the small displacement method.* Computer Physics Communications, 2009. **180**(12): p. 2622-2633.
170. Togo, A., F. Oba, and I. Tanaka, *First-principles calculations of the ferroelastic transition between rutile-type and CaCl(2)-type SiO(2) at high pressures.* Physical Review B, 2008. **78**(13).

171. M, A.J.H. and M. Kaviany, *Phonon Transport in Molecular Dynamics Simulations: Formulation and Thermal Conductivity Prediction*, in *Advances in Heat Transfer*, J.P.H.A.B.-C. George A. Greene and I.C. Young, Editors. 2006, Elsevier. p. 169-255.
172. Bayin, S.S.u., *Mathematical methods in science and engineering*. 2006, Hoboken, N.J.: Wiley-Interscience. xxvii, 679 p.
173. Huang, Z., T.S. Fisher, and J.Y. Murthy, *Simulation of phonon transmission through graphene and graphene nanoribbons with a Green's function method.* Journal of Applied Physics, 2010. **108**(9): p. 094319.
174. Zhang, W., T.S. Fisher, and N. Mingo, *Simulation of interfacial phonon transport in Si-Ge heterostructures using an atomistic Green's function method.* Journal of Heat Transfer-Transactions of the Asme, 2007. **129**(4): p. 483-491.
175. Sadasivam, S., et al., *The Atomistic Green's function method for interfacial phonon transport.* Ann. Rev. Heat Transfer, 2014. **17**: p. 89-145.
176. Dhar, A. and D. Roy, *Heat Transport in Harmonic Lattices.* Journal of Statistical Physics, 2006. **125**(4): p. 801-820.
177. Zhang, W., T.S. Fisher, and N. Mingo, *The atomistic Green's function method: An efficient simulation approach for nanoscale phonon transport.* Numerical Heat Transfer Part B-Fundamentals, 2007. **51**(4): p. 333-349.
178. Monkhorst, H.J. and J.D. Pack, *Special points for Brillouin-zone integrations.* Physical Review B, 1976. **13**(12): p. 5188-5192.
179. Loy, J.M., D. Singh, and J.Y. Murthy, *Non-Gray Phonon Transport Using a Hybrid Bte-Fourier Solver.* Ht2009: Proceedings of the Asme Summer Heat Transfer Conference 2009, Vol 2, 2009: p. 601-610.
180. Vallabhaneni, A.K., et al. *A Study of Spatially-Resolved Non-Equilibrium in Laser-Irradiated Graphene Using Boltzmann Transport Equation*. in *ASME 2013 International Mechanical Engineering Congress and Exposition*. 2013. San Diego, California, USA: ASME.
181. Li, W., et al., *ShengBTE: A solver of the Boltzmann transport equation for phonons.* Computer Physics Communications, 2014. **185**(6): p. 1747-1758.
182. Omini, M. and A. Sparavigna, *An iterative approach to the phonon Boltzmann equation in the theory of thermal conductivity.* Physica B: Condensed Matter, 1995. **212**(2): p. 101-112.
183. Maradudin, A. and A. Fein, *Scattering of neutrons by an anharmonic crystal.* Physical Review, 1962. **128**(6): p. 2589.
184. Wu, X., et al., *Thermal conductivity of wurtzite zinc-oxide from first-principles lattice dynamics–a comparative study with gallium nitride.* Scientific reports, 2016. **6**.
185. Broido, D., et al., *Intrinsic lattice thermal conductivity of semiconductors from first principles.* Applied Physics Letters, 2007. **91**(23): p. 231922.
186. Zhong, X., et al., *First-principles study of strain-induced modulation of energy gaps of graphene/BN and BN bilayers.* Physical Review B, 2011. **83**(19): p. 193403.
187. Kresse, G. and J. Furthmuller, *Efficiency of ab-initio total energy calculations for metals and semiconductors using a plane-wave basis set.* Computational Materials Science, 1996. **6**(1): p. 15-50.

188. Kresse, G. and D. Joubert, *From ultrasoft pseudopotentials to the projector augmented-wave method.* Physical Review B, 1999. **59**(3): p. 1758-1775.
189. Perdew, J.P., *Density-functional approximation for the correlation energy of the inhomogeneous electron gas.* Physical Review B, 1986. **33**(12): p. 8822-8824.
190. Marini, A., P. García-González, and A. Rubio, *First-Principles Description of Correlation Effects in Layered Materials.* Physical Review Letters, 2006. **96**(13): p. 136404.
191. Charlier, J.-C., X. Gonze, and J.-P. Michenaud, *Graphite interplanar bonding: electronic delocalization and van der Waals interaction.* EPL (Europhysics Letters), 1994. **28**(6): p. 403.
192. Yu, W.J., et al., *\textit{Ab initio} study of phase transformations in boron nitride.* Physical Review B, 2003. **67**(1): p. 014108.
193. Rydberg, H., et al., *Van der Waals Density Functional for Layered Structures.* Physical Review Letters, 2003. **91**(12): p. 126402.
194. Chen, L., Z. Huang, and S. Kumar, *Phonon transmission and thermal conductance across graphene/Cu interface.* Applied Physics Letters, 2013. **103**(12): p. 123110.
195. Mingo, N., et al., *Phonon transmission through defects in carbon nanotubes from first principles.* 2008.
196. Ooi, N., et al., *Structural properties of hexagonal boron nitride.* Modelling and Simulation in Materials Science and Engineering, 2006. **14**(3): p. 515.
197. Oshima, C. and A. Nagashima, *Ultra-thin epitaxial films of graphite and hexagonal boron nitride on solid surfaces.* Journal of Physics: Condensed Matter, 1997. **9**(1): p. 1.
198. Shikin, A.M., V.K. Adamchuk, and K.H. Rieder, *Formation of quasi-free graphene on the Ni(111) surface with intercalated Cu, Ag, and Au layers.* Physics of the Solid State, 2009. **51**(11): p. 2390-2400.
199. Shikin, A.M., et al., *Surface intercalation of gold underneath a graphite monolayer on Ni(111) studied by angle-resolved photoemission and high-resolution electron-energy-loss spectroscopy.* Physical Review B, 2000. **62**(19): p. 13202-13208.
200. Allard, A. and L. Wirtz, *Graphene on metallic substrates: suppression of the Kohn anomalies in the phonon dispersion.* Nano letters, 2010. **10**(11): p. 4335-4340.
201. Ramasubramaniam, A., D. Naveh, and E. Towe, *Tunable Band Gaps in Bilayer Graphene−BN Heterostructures.* Nano Letters, 2011. **11**(3): p. 1070-1075.
202. Khomyakov, P., et al., *First-principles study of the interaction and charge transfer between graphene and metals.* Physical Review B, 2009. **79**(19): p. 195425.
203. Xiong, S., et al., *Classical to Quantum Transition of Heat Transfer between Two Silica Clusters.* Physical Review Letters, 2014. **112**(11): p. 114301.
204. Beechem, T., L. Yates, and S. Graham, *Invited Review Article: Error and uncertainty in Raman thermal conductivity measurements.* Review of Scientific Instruments, 2015. **86**(4): p. 041101.
205. Li, X. and R. Yang, *Effect of lattice mismatch on phonon transmission and interface thermal conductance across dissimilar material interfaces.* Physical Review B, 2012. **86**(5): p. 054305.
206. Klimeš, J., D.R. Bowler, and A. Michaelides, *Van der Waals density functionals applied to solids.* Physical Review B, 2011. **83**(19): p. 195131.

207. Dion, M., et al., *Van der Waals density functional for general geometries.* Physical review letters, 2004. **92**(24): p. 246401.
208. Gong, C., et al., *The unusual mechanism of partial Fermi level pinning at metal–MoS2 interfaces.* Nano letters, 2014. **14**(4): p. 1714-1720.
209. Cao, T., et al., *Valley-selective circular dichroism of monolayer molybdenum disulphide.* Nature communications, 2012. **3**: p. 887.
210. Scalise, E., et al., *Strain-induced semiconductor to metal transition in the two-dimensional honeycomb structure of MoS2.* Nano Research, 2012. **5**(1): p. 43-48.
211. Stewart, D.A., I. Savic, and N. Mingo, *First-principles calculation of the isotope effect on boron nitride nanotube thermal conductivity.* Nano letters, 2008. **9**(1): p. 81-84.
212. Tian, Z., K. Esfarjani, and G. Chen, *Enhancing phonon transmission across a Si/Ge interface by atomic roughness: First-principles study with the Green's function method.* Physical Review B, 2012. **86**(23): p. 235304.
213. Kang, J., et al., *Band offsets and heterostructures of two-dimensional semiconductors.* Applied Physics Letters, 2013. **102**(1): p. 012111.
214. Savin, A., et al., *ELF: The electron localization function.* Angewandte Chemie International Edition in English, 1997. **36**(17): p. 1808-1832.
215. Silvi, B. and A. Savin, *Classification of chemical bonds based on topological analysis of electron localization functions.* Nature, 1994. **371**(6499): p. 683-686.
216. Li, Y., et al., *Single-layer MoS 2 as an efficient photocatalyst.* Catalysis Science & Technology, 2013. **3**(9): p. 2214-2220.
217. Li, J., T.C.A. Yeung, and C.H. Kam, *Phonon transport in nanowire with contacts: Size and doping.* Journal of Applied Physics, 2012. **111**(9).
218. Peelaers, H. and C.G. Van de Walle, *Brillouin zone and band structure of β-Ga2O3.* physica status solidi (b), 2015. **252**(4): p. 828-832.
219. Kresse, G. and J. Furthmüller, *Efficient iterative schemes for ab initio total-energy calculations using a plane-wave basis set.* Physical review B, 1996. **54**(16): p. 11169.
220. Kresse, G. and D. Joubert, *From ultrasoft pseudopotentials to the projector augmented-wave method.* Physical Review B, 1999. **59**(3): p. 1758.
221. Perdew, J.P., K. Burke, and M. Ernzerhof, *Generalized gradient approximation made simple.* Physical review letters, 1996. **77**(18): p. 3865.
222. Åhman, J., *J. Åhman, G. Svensson, and J. Albertsson, Acta Crystallogr. Sect. C 52, 1336 (1996).* Acta Crystallogr. Sect. C, 1996. **52**: p. 1336.
223. Ratsifaritana, C. and P. Klemens, *Scattering of phonons by vacancies.* International journal of thermophysics, 1987. **8**(6): p. 737-750.
224. Klemens, P. and D. Pedraza, *Thermal conductivity of graphite in the basal plane.* Carbon, 1994. **32**(4): p. 735-741.
225. Klemens, P., *The scattering of low-frequency lattice waves by static imperfections.* Proceedings of the Physical Society. Section A, 1955. **68**(12): p. 1113.
226. Xie, G., et al., *A bond-order theory on the phonon scattering by vacancies in two-dimensional materials.* Scientific reports, 2014. **4**.
227. Yan, Z., et al., *Phonon transport at the interfaces of vertically stacked graphene and hexagonal boron nitride heterostructures.* Nanoscale, 2016. **8**(7): p. 4037-4046.

228. Li, X., et al., *Isoelectronic tungsten doping in monolayer MoSe2 for carrier type modulation.* Advanced Materials, 2016. **28**(37): p. 8240-8247.
229. Böker, T., et al., *Band structure of MoS 2, MoSe 2, and α− MoTe 2: Angle-resolved photoelectron spectroscopy and ab initio calculations.* Physical Review B, 2001. **64**(23): p. 235305.
230. Matthiessen, A. and C. Vogt, *On the influence of temperature on the electric conducting-power of alloys.* Philosophical Transactions of the Royal Society of London, 1864. **154**: p. 167-200.
231. Li, W., et al., *Thermal conductivity of bulk and nanowire Mg 2 Si x Sn 1− x alloys from first principles.* Physical Review B, 2012. **86**(17): p. 174307.
232. Nika, D., et al., *Phonon thermal conduction in graphene: Role of Umklapp and edge roughness scattering.* Physical Review B, 2009. **79**(15): p. 155413.
233. Lindsay, L., D. Broido, and T. Reinecke, *First-principles determination of ultrahigh thermal conductivity of boron arsenide: A competitor for diamond?* Physical review letters, 2013. **111**(2): p. 025901.
234. Lindsay, L. and D. Broido, *Three-phonon phase space and lattice thermal conductivity in semiconductors.* Journal of Physics: Condensed Matter, 2008. **20**(16): p. 165209.
235. Mingo, N., *Anharmonic phonon flow through molecular-sized junctions.* Physical Review B, 2006. **74**(12): p. 125402.
236. Rupp, M., et al., *Fast and accurate modeling of molecular atomization energies with machine learning.* Physical review letters, 2012. **108**(5): p. 058301.
237. Hansen, K., et al., *Assessment and validation of machine learning methods for predicting molecular atomization energies.* Journal of Chemical Theory and Computation, 2013. **9**(8): p. 3404-3419.
238. Rupp, M., R. Ramakrishnan, and O.A. von Lilienfeld, *Machine learning for quantum mechanical properties of atoms in molecules.* The Journal of Physical Chemistry Letters, 2015. **6**(16): p. 3309-3313.
239. Gaultois, M.W., et al., *Perspective: Web-based machine learning models for real-time screening of thermoelectric materials properties.* APL Materials, 2016. **4**(5): p. 053213.
240. Seko, A., et al., *Representation of compounds for machine-learning prediction of physical properties.* Physical Review B, 2017. **95**(14): p. 144110.
241. Bae, M.H., et al., *Infrared Microscopy of Joule Heating in Graphene Field Effect Transistors.* 2009 9th Ieee Conference on Nanotechnology (Ieee-Nano), 2009: p. 818-821.
242. Bae, M.H., et al., *Infrared Imaging of Heat Dissipation in Graphene Transistors.* Graphene, Ge/Iii-V, and Emerging Materials for Post-Cmos Applications 2, 2010. **28**(5): p. 51-62.
243. Bae, M.H., et al., *Imaging, Simulation, and Electrostatic Control of Power Dissipation in Graphene Devices.* Nano Letters, 2010. **10**(12): p. 4787-4793.
244. Pop, E., *Energy Dissipation and Transport in Nanoscale Devices.* Nano Research, 2010. **3**(3): p. 147-169.